

Remote Powering and Communication of Implantable Biosensors Through Inductive Link

THÈSE N° 5936 (2013)

PRÉSENTÉE LE 13 NOVEMBRE 2013

À LA FACULTÉ INFORMATIQUE ET COMMUNICATIONS
LABORATOIRE DES SYSTÈMES INTÉGRÉS (IC/STI)
PROGRAMME DOCTORAL EN GÉNIE ÉLECTRIQUE

ÉCOLE POLYTECHNIQUE FÉDÉRALE DE LAUSANNE

POUR L'OBTENTION DU GRADE DE DOCTEUR ÈS SCIENCES

PAR

Jacopo OLIVO

acceptée sur proposition du jury:

Prof. M. Paolone, président du jury
Prof. G. De Micheli, Dr S. Carrara, directeurs de thèse
Dr T. Constandinou, rapporteur
Dr C. Dehollain, rapporteur
Prof. G. Gielen, rapporteur



ÉCOLE POLYTECHNIQUE
FÉDÉRALE DE LAUSANNE

Suisse
2013

Remote Powering and Communication of Implantable Biosensors Through Inductive Link

THÈSE N° 5936 (2013)

PRÉSENTÉE LE 13 NOVEMBRE 2013

À LA FACULTÉ INFORMATIQUE ET COMMUNICATIONS
LABORATOIRE DES SYSTÈMES INTÉGRÉS (IC/STI)
PROGRAMME DOCTORAL EN GÉNIE ÉLECTRIQUE

ÉCOLE POLYTECHNIQUE FÉDÉRALE DE LAUSANNE

POUR L'OBTENTION DU GRADE DE DOCTEUR ÈS SCIENCES

PAR

Jacopo OLIVO

acceptée sur proposition du jury:

Prof. M. Paolone, président du jury
Prof. G. De Micheli, Dr S. Carrara, directeurs de thèse
Dr T. Constandinou, rapporteur
Dr C. Dehollain, rapporteur
Prof. G. Gielen, rapporteur



ÉCOLE POLYTECHNIQUE
FÉDÉRALE DE LAUSANNE

Suisse
2013

Acknowledgements

My first acknowledgement goes to my thesis directors, Prof. Giovanni De Micheli and Dr. Sandro Carrara, for the opportunity they gave me to pursue my research in their group. They trusted me and gave me ample freedom to explore different ideas and develop my own research path. Furthermore, they have always been ready to advise me and contribute to my work with precious suggestions, useful remarks and interesting discussions. I have really enjoyed the friendly and collaborative atmosphere they were able to create in the laboratory and I cannot imagine a more friendly work environment. I would like to thank also the members of the jury who have evaluated this thesis and provided useful feedbacks: Prof. Mario Paolone, Dr. Catherine Dehollain, Prof. Georges Gielen, and Prof. Timothy Constandinou.

A successful doctorate requires a constant interaction with colleagues and collaborators. The most interesting ideas I have had have been the result of discussions and brainstorming. Thus, I would like to thank all the persons who contributed to the results reported in this thesis. Sara and Antonio, for the development of two generations of ICs; Gözen, that allowed me to “steal” some of her knowledge on analog IC design and some of her circuits as well; Francesco Merli, for the useful discussions on multi-layer inductors; the CMi staff and more in particular Laszlo Pethö, Joffrey Pernollet and Anthony Guillet for the precious suggestions while dealing with microfabrication; Prof. Jérôme Waser who allowed me to use cyanide in his laboratory and Maria Victoria Vita for the assistance; Jens Andersen and Alexander Perez for the useful discussions on microwave networks and scattering parameters; Dr. Catherine Dehollain and Enver Kiliç for the useful suggestions and the access to part of their work; the Atelier ACI for the realization of prototypes and test boards; Joseph Guzzardi and André Badertscher for their help while dealing with practical and technical problems.

The doctorate is somehow like a travel, where the travel-mates are as important as the destination. For this reason, a special thanks goes to all those friends that have been with me during this experience. The “Italian group”: Matteo, Anna, Ludovica, Jaume (almost Italian!), Cristina, Ivan, Camilla, Andrea, Michele, Federico, Massimo, Michela, and Francesca. With them I have shared wonderful moments, travel experiences (Matteo and Anna are “Gold Members” of my travels to Bologna), mountain experiences (Michele was my partner while building a snow cave in the Alps during the coldest winter in the last 20 years), home sharing (Ivan, of course!), culinary experiences (Camilla and Andrea: usually at their place, usually offered by them; Ludovica and Jaume: usually at their place, usually offered by them), stimulating and never-ending discussions (Michele and Massimo), and sailing (Matteo, Michele, and

Acknowledgements

Massimo are honorary guests of the Cachalo). A special thanks to Cristina: she put up with me for almost 5 years (in her own way though!) and she keeps doing it. My friends in Bologna: Simone, Michele, Paolo, Filippo, Matteo, and Riccardo. They welcome me every time I go back home and I really feel like I have never left Bologna while I am with them. A thanks also to Marcello and Lorenzo: the time we spend together is not a lot, but is very precious.

My colleagues, past and present, at the LSI. The master students who collaborated with me: Matteo, Lorenzo, Maria Antonietta, and Eric; all the other friends of LSI: Irene, Julien, Pierre-Emmanuel, Somayyeh, Hassan, Alena, Wenqi, Hu, Haykel, Abhishek, Joan, Srini, and Ciprian. A special thanks goes to Vasilis who proof-read most of my articles and works. I would like to thank also Christina, the tireless secretary of the laboratory, for the help while interacting with the administration and the nice chats; Rodolphe who patiently submitted all my orders to the suppliers; Anil, for the assistance with scientific contents and event organization.

My flatmates, Ivan and Shashi. We have shared the house for 4 years and we have had a lot of fun. We became a sort of a family and I cannot think to Chemin des Côtes without you. A special thanks to the “fourth flatmate” Vincenzo, who introduced jokes and rituals that went along with us during these years. Another thanks to Ruben and Alessandro, who often shared their evenings with us and with our randomness.

To conclude, a great thanks to my family. With their unconditioned love, they have supported me during the doctorate as well as during the other 18 years of school and university. They shared my successes and helped me during the times of discouragement. They helped me to distinguish the details from the important things. Their aid has been fundamental and I would not have reached this achievement without them. It is nice to know that I can always count on you.

Abstract

Nowadays there is an increasing interest in the field of implantable biosensors. The possibility of real-time monitoring of the human body from inside paves the way to a large number of applications and offers wide opportunities for the future. Within this scenario, the i-IronIC project aims to develop an implantable, low cost, health-care device for real-time monitoring of human metabolites. The contribution of this research work to the i-IronIC project consists of the design and realization of a complete platform to provide power, data communication and remote control to the implantable biosensor. High wearability of the transmitting unit, low invasivity of the implanted electronics, integration of the power management module within the sensor, and a reliable communication protocol with portable devices are the key points of this platform.

The power is transmitted to the implanted sensor by exploiting an inductive link. Simulations have been performed to check the effects of several variables on the link performance. These simulations have finally confirmed the possibility to operate in the low megahertz range, where tissue absorption is minimum, even if a miniaturized receiving inductor is used.

A wearable patch has been designed to transmit power through the body tissues by driving an external inductor. The same inductive link is used to achieve bidirectional data communication with the implanted device. The patch, named IronIC, is powered by lithium-ion polymer batteries and can be remotely controlled by means of a dedicated Android application running on smartphones and tablets. Long-range communication between the patch and portable devices is performed by means of Bluetooth protocol.

Different typologies of receiving inductors have been designed to minimize the size of the implantable device and reduce the discomfort of the patient. Multi-layer, printed spiral inductors and microfabricated spiral inductors have been designed, fabricated and tested. Both the approaches involve a sensibly smaller size, as compared to classic “pancake” inductors used for remote powering. Furthermore, the second solution enables the realization of the receiving inductor directly on the silicon substrate hosting the sensor, thus involving a further miniaturization of the implanted device.

An integrated power module has been designed and fabricated in 0.18 μm CMOS technology to perform power management and data communication with the external patch. The circuit, to be merged with the sensor readout circuit, consists of a half-wave voltage rectifier, a low-dropout regulator, an amplitude demodulator and a load modulator. The module receives

Abstract

the power from the implanted inductor and provides a stable voltage to the sensor readout circuit. Finally, the amplitude demodulator and the load modulator enable short-range communication with the patch.

Keywords: Inductive link, remote powering, implantable biosensors, multi-layer inductors, microfabricated inductors.

Résumé

Les dernières années ont vu un intérêt croissant envers le domaine des capteurs implantables. La possibilité de contrôler en temps réel le corps humain ouvre la voie vers de nombreuses applications et offre des opportunités intéressantes pour le futur. Dans ce contexte, le projet i-IronIC a pour but de développer un capteur implantable à bas prix pour le contrôle en temps réel de plusieurs métabolites dans le corps humain.

La contribution de ce travail de recherche au projet i-IronIC consiste en la réalisation d'une plateforme complète capable de transférer l'alimentation et de communiquer avec le capteur implanté. Invasivité et dimensions réduites, intégration du module de gestion de puissance et protocole de communication fiable font parti des points clés de cette plateforme.

L'alimentation est transmise au capteur implantable par lien inductif. Plusieurs simulations ont été effectuées afin d'étudier l'effet de variables externes sur les performances du lien. Ces simulations ont confirmé la possibilité de travailler dans le domaine du mégahertz, où l'absorption par les tissus est minime, même lorsque des inducteurs miniaturisés sont utilisés.

Un patch électronique a été conçu afin de transmettre l'alimentation à travers la peau grâce à un inducteur externe. En outre, ce même lien est exploité pour communiquer de manière bidirectionnelle avec le dispositif implanté. Le patch, appelé IronIC, est alimenté par batteries aux polymères de lithium et peut être contrôlé à distance au moyen d'une application Android pour smartphone et tablet. La communication à longue portée entre le patch et d'autres dispositifs portables est basée sur le protocole Bluetooth.

Différents types d'inducteurs de réception ont été étudiés pour minimiser les dimensions finales du dispositif et réduire l'inconfort du patient. Ainsi, des inducteurs multicouches et des inducteurs micro-fabriqués ont été conçus, réalisés et testés. Les deux approches impliquent une diminution substantielle de la taille par rapport aux inducteurs "pancake", habituellement utilisés pour la transmission de puissance sans fils. En outre, la deuxième solution présente l'avantage de pouvoir être réalisée directement sur le substrat de silicium qui accueille le capteur, permettant de réduire encore la taille de l'implant.

Un module intégré pour la gestion de la puissance a été conçu et réalisé en technologie CMOS 0.18 μm . Le module est responsable de la gestion de la puissance reçue et de la communication avec le patch. Le circuit, qui doit être intégré avec le capteur, comprend un redresseur à demi-onde, un régulateur à faible chute de tension, un démodulateur d'amplitude et un modulateur

Résumé

de charge. Le module reçoit l'alimentation par l'inducteur et fournit une tension stable au capteur. Le démodulateur d'amplitude et le modulateur de charge, quant à eux, permettent la communication à courte portée avec le patch.

Mots clés : Lien inductif, transmission de puissance sans fils, biocapteurs implantables, inducteurs multicouches, inducteurs micro-fabriqués.

Sommario

Negli ultimi anni si è potuto assistere ad un crescente interesse nei confronti dei biosensori impiantabili. La possibilità di monitorare in tempo reale il corpo umano dall'interno apre la strada ad un elevato numero di applicazioni ed offre interessanti prospettive per il futuro. In questo contesto, il progetto i-IronIC si propone di sviluppare un sensore impiantabile a basso costo per il monitoraggio in tempo reale di diversi metaboliti presenti nel corpo umano. Il contributo di questo lavoro di ricerca al progetto i-IronIC consiste nel progetto e nella realizzazione di una piattaforma completa in grado di trasmettere potenza e comunicare con il sensore impiantato. Elevata vestibilità, dimensioni contenute, integrazione del modulo di gestione della potenza ed un protocollo di comunicazione affidabile sono punti chiave di questa piattaforma.

La potenza è trasmessa al sensore impiantabile mediante accoppiamento induttivo. Diverse simulazioni sono state effettuate per studiare l'effetto di variabili esterne sulle prestazioni dell'accoppiamento. Tali simulazioni hanno confermato la possibilità di lavorare nel campo dei megahertz, dove l'assorbimento da parte dei tessuti è minimo, anche quando sono utilizzate delle induttanze riceventi miniaturizzate.

Un cerotto elettronico è stato progettato per trasmettere potenza attraverso la pelle utilizzando un accoppiamento induttivo. Inoltre, lo stesso accoppiamento induttivo usato per la trasmissione di potenza è utilizzato per comunicare bidirezionalmente con il dispositivo impiantato. Il cerotto, chiamato IronIC, è alimentato da batterie agli ioni di litio e può essere controllato a distanza tramite un'applicazione Android dedicata per smartphone e tablet. La comunicazione a lungo raggio fra il cerotto ed eventuali dispositivi portatili è effettuata tramite Bluetooth.

Diverse tipologie di induttori riceventi sono state studiate per minimizzare le dimensioni finali del dispositivo e diminuire il disagio del paziente. Induttori multi-strato ed induttori microfabbricati sono stati progettati, realizzati e testati. Entrambi gli approcci comportano una notevole diminuzione delle dimensioni se comparati ai classici induttori "pancake" solitamente utilizzati per la trasmissione di potenza senza fili. Inoltre, la seconda soluzione presenta il vantaggio di poter essere implementata direttamente sul substrato di silicio che ospita il sensore, riducendo ulteriormente le dimensioni dell'impianto.

Un modulo integrato per la gestione della potenza è stato progettato e realizzato in tecnologia CMOS 0.18 μ m. Il modulo si occupa della gestione della potenza ricevuta e della comuni-

Sommario

cazione con il cerotto. Il circuito, da integrare con il sensore, include un raddrizzatore a semionda, un regolatore, un demodulatore di ampiezza ed un modulatore di carico. Il modulo riceve potenza dall'induttore impiantato e fornisce una tensione stabile al sensore. Infine, il demodulatore di ampiezza ed il modulatore di carico consentono la comunicazione a corto raggio con il cerotto.

Parole chiave: Accoppiamento induttivo, trasmissione di potenza senza fili, biosensori impiantabili, induttori multi-strato, induttori microfabbricati.

Contents

Acknowledgements	iii
Abstract	v
Contents	xiii
List of figures	xvii
List of tables	xix
1 Introduction	1
1.1 i-IronIC Project	2
1.1.1 Description	2
1.1.2 Requirements	3
1.1.3 Remote Powering and Data Communication	5
1.2 Research Contribution	6
1.3 Organization of the Thesis	7
2 Energy Harvesting and Remote Powering for Implantable Biosensors	9
2.1 Kinetic	9
2.2 Thermoelectric Effect	10
2.3 Fuel Cells	15
2.4 Infrared Radiation	17
2.5 Low Frequency Magnetic Fields	18
2.6 Emerging Techniques	18
2.7 Inductive Link	19
2.7.1 Inductive Link Description	19
2.7.2 Inductive Link in the Literature	23
2.7.3 Health Implication - Specific Absorption Rate	25
2.8 Chapter Contribution and Summary	28
3 Inductive Link for mm-sized Implants: Frequency and Geometry Optimization	29
3.1 Inductive Link Analysis	30
3.2 Inductor Modeling	34
3.3 Chapter Contribution and Summary	41

4	Design and Fabrication of Miniaturized Receiving Inductors	43
4.1	Multi-layer Spiral Inductors	43
4.1.1	Standard Design Techniques for Inductive Links	44
4.1.2	Design and Test of Multi-layer Spiral Inductors	46
4.1.3	Performance Evaluation	50
4.2	Microfabricated Spiral Inductors	53
4.2.1	Inductor Design	54
4.2.2	Fabrication Process Flow	57
4.2.3	Performance Evaluation	58
4.3	Chapter Contribution and Summary	60
5	IronIC Patch	61
5.1	Patch Design	61
5.1.1	Substrate Description	62
5.1.2	Class-E Power Amplifier	63
5.1.3	Downlink Modulator	65
5.1.4	Uplink Demodulator	65
5.1.5	Power Supply	66
5.1.6	External Inductor	66
5.2	Experimental Results	66
5.2.1	Performance Evaluation	66
5.2.2	Battery Consumption	67
5.2.3	Comparison with the Literature	68
5.3	Chapter Contribution and Summary	70
6	Android Interface	71
6.1	Application Description	71
6.1.1	Communication Protocol	73
6.1.2	8b/10b Encoding	75
6.2	Experimental Results	78
6.3	Chapter Contribution and Summary	79
7	Integrated Power Module	81
7.1	Design	81
7.1.1	Voltage Rectifier and Load Modulator	82
7.1.2	Amplitude Demodulator	84
7.2	Simulations	85
7.3	Measurements	89
7.3.1	Rectifier and Load Modulator	90
7.3.2	Amplitude Demodulator	93
7.4	Chapter Contribution and Summary	93

8	Conclusions and Future Work	95
8.1	Thesis Summary and Contributions	96
8.2	Future Work	97
A	Appendix	99
	Bibliography	112
	Curriculum Vitae	113

List of Figures

1.1	Schematic description of the i-IronIC implantable biosensor.	2
1.2	Example of voltammogram obtained with cyclic voltammetry.	3
1.3	Schematic representation of an inductive link performing remote powering and bidirectional data communication.	4
1.4	A platform has been conceived to provide remote powering and data communication to the implantable system.	5
2.1	Schematic representation of a thermocouple.	11
2.2	The connection of many thermocouples electrically in series and thermally in parallel forms a thermopile.	11
2.3	Schematic example of a thermal circuit.	12
2.4	Schematic description of a PEM fuel cell.	16
2.5	Schematic description of a membrane-less fuel cell.	16
2.6	Example of an IR harvester.	17
2.7	Low frequency magnetic fields are used to move an implanted rotor to generate power.	18
2.8	An inductive link is obtained with a primary coil connected to a power source and magnetically coupled to a secondary coil.	20
2.9	Power gain obtained by [98] using an inductive link composed of two 4 mm ² coils. 24	
3.1	Slice of human abdomen obtained with the Visible Human Server [106].	30
3.2	The smaller size of the coils involves a higher optimal frequency, along with a lower link efficiency.	32
3.3	Different implantation sites do not affect the optimum frequency.	33
3.4	Lateral misalignments between the coils have been simulated for a given geometry. 33	
3.5	Maximum link efficiency obtained with multiple-turn external coils.	34
3.6	Lumped RLC model of a printed spiral inductor.	35
3.7	Geometrical and physical parameters of a printed inductor and the surrounding substrates.	35
3.8	Impedance of the inductors described in Table 3.2.	40
4.1	Link efficiency and voltage gain decrease when smaller receiving inductors are used.	47

List of Figures

4.2	By reducing the number of turns of the external inductor and increasing their width, the link efficiency slightly decreases while the voltage gain noticeably increases.	48
4.3	Layout of a multi-layer spiral inductor on PCB.	49
4.4	Multi-layer spiral inductors are obtained by stacking and connecting single-layer inductors realized on a flexible substrate.	50
4.5	Multi-layer spiral inductors enable a higher link efficiency and voltage gain if compared with single-layer inductors having the same area.	51
4.6	Both the model and the measurements confirm a strong dependence of the transferred power on distance.	52
4.7	Measurements are performed using beef sirloin between the inductors.	52
4.8	Microfabricated spiral inductors during the fabrication process.	53
4.9	The inductors are simulated onto a substrate of silicon + silicon dioxide.	54
4.10	A higher trace thickness decreases the inductor resistance, thus increasing the quality factor.	55
4.11	The quality factor, for a given shape and size of the spiral inductor, is weakly dependent on the number of turns.	56
4.12	Fabrication process flow.	56
4.13	SEM pictures of the microfabricated inductors.	58
4.14	Electrical characteristic of the microfabricated inductors.	59
4.15	Power received by the microfabricated inductor against the distance between transmitting and receiving inductors.	60
5.1	Functionalities of the IronIC patch.	62
5.2	The patch is realized on a flexible FR4 substrate.	62
5.3	The patch can be placed over the implantation zones, in concave or convex parts of the body, to power the implanted sensor and communicate with it.	63
5.4	Schematic of the IronIC patch at component-level.	64
5.5	Behavior of voltage and current across the switch of a well-tuned class-E amplifier.	65
6.1	Activities of BlueCells application.	74
6.2	Biosensor instruction set.	75
6.3	Communication protocol for a cyclic voltammetry.	76
6.4	Description of the 8b/10b encoding.	77
6.5	Running disparity state diagram.	78
6.6	Calibration lines of lactate and glucose, obtained by means of the Android application and an external sensor.	79
7.1	The implanted sensor receives power and data from the IronIC patch. The transmitter performs long-range communication with remote devices by means of Bluetooth.	82
7.2	Schematic of the voltage rectifier and the load modulation unit.	83

7.3 In order to have NMOS transistors with bulk potential different from the substrate potential, a triple well has been used.	83
7.4 Schematic of the amplitude demodulator.	84
7.5 Equivalent circuit of the demodulator.	85
7.6 Pseudo-logic is used to achieve threshold voltages sensibly higher or lower than those obtained with standard CMOS inverters.	86
7.7 Characteristic of inverter I_3	86
7.8 The power module is simulated to check its performance.	88
7.9 Layout of the power module fabricated in 0.18 μm CMOS technology.	89
7.10 The measurement setup used to test the performance of the power module. . .	90
7.11 Output voltage and output current of the rectifier against the output load for several distances between the inductors.	91
7.12 Input and output voltages of the rectifier during the functioning.	92
7.13 Test of the uplink communication through load modulation.	92
7.14 Test of downlink communication through ASK modulation.	93
A.1 Schematic description of a two-port network by means of the scattering parameters.	100
A.2 Signal flow chart of a two-port network.	102

List of Tables

2.1	Human temperature gradients at room temperature.	14
2.2	Implantable devices exploiting inductive links for wireless power transmission.	26
2.3	Comparison between different harvesting techniques.	27
3.1	Implantation sites.	31
3.2	Geometrical parameters of the test inductors.	39
3.3	Electrical parameters of the test inductors.	39
5.1	Physical properties of the FR4 patch substrate.	63
5.2	Power consumption of the patch in different operating modes.	67
5.3	Comparison among inductive powering systems for implantable devices.	69

1 Introduction

Nowadays there is an increasing interest in the field of implantable biosensors. The possibility of real-time monitoring of the human body from inside paves the way to a large number of applications and offers wide scenarios for the future. As an example, a promising application is the use of implanted electrode arrays to monitor local neural circuits and the related spiking activity [1–4]. The study of brain neural activity is a great help in the treatment of disorders such as blindness, deafness, epilepsy, Parkinson's disease and paralysis. For instance, in the last mentioned disorder, by observing the emission rate of electrical impulses occurring when particular movements are performed, it is possible to transform these signals into commands for neuroprosthetic devices. These devices, controlled directly through the nerve signals [5], are thus able to partially render the mobility to people with motion disabilities.

The brain is not the only application area for implantable biosensors. Significant effort is dedicated to the design and development of implantable chemical sensors, capable of detecting the concentration of clinically relevant species [6]. The real-time, continuous monitoring of several metabolites in the human body enables personalized medicine and point-of-care therapies, tuned on the response of the patient. As example, the constant monitoring of the glucose level in the subcutaneous interstitial fluids is an important aid to those patients who suffer from diabetes. By means of implantable sensors, located in the subcutaneous zones, the percentage of glucose into the blood (*glycemia*) can be recorded and transmitted to a remote device, such as a smartphone, to be analyzed. Thus, periodic and disturbing blood drawing can be avoided.

Another metabolite that can be monitored by means of subcutaneous sensors is the lactate, a product of the anaerobic muscle activity [7]. The lactate concentration into the blood (*lactatemia*) or into interstitial tissues in muscles can be recorded to monitor the muscular effort in sportsmen or people under rehabilitation. Different solutions have been proposed in the literature to design and optimize amperometric biosensors dedicated to lactate detection [8, 9]. The use of carbon nanotubes has been proposed to enhance the sensitivity of these devices [10, 11]. The presence of nanostructured electrodes slightly complicates the design of the sensor. Due to the toxicity of nanotubes [12, 13], selective membranes must be used to

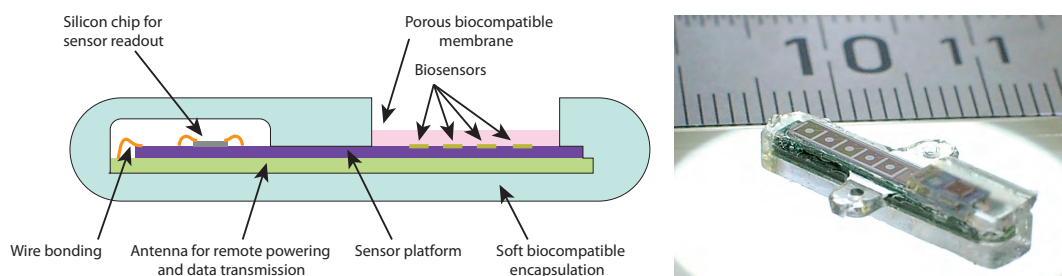


Figure 1.1: Schematic description of the i-IronIC implantable biosensor. Elaborated from [20].

avoid dispersion into the body. However, the enhanced sensitivity enables the detection of small concentrations of the metabolite, typical of the body range.

1.1 i-IronIC Project

1.1.1 Description

The design and development of implantable sensors for the detection and measurement of clinically relevant species is a multi-disciplinary field that is attracting the attention of academia and industry since the last two decades. The cost for health-care services and the population aging in developed countries increase the importance of these devices to prevent chronic diseases and support the rehabilitation. Within this scenario, the i-IronIC project aims to develop a low cost, health-care platform for real-time monitoring of human metabolites such as lactate, cholesterol, and ATP. The continuous monitoring of these compounds enables point-of-care treatments, tuned on the response of the patient, and offers an accurate “telemetry” of the physical condition. Point-of-care therapies can be used to provide assistance to elderly or disabled people, while “body-telemetry” can be useful for professional and recreational sportsmen training.

Devices dedicated to the continuous monitoring of human metabolites, such as glucose [14] and lactate [7], are already present on the market. Furthermore, experimental prototypes have been reported in the literature for the detection of glutamate [15], ATP [16], and exogenous metabolites such as cyclophosphamide and naproxen [17]. The aim of the i-IronIC project is to hierarchically integrate these metabolite sensors into an unobtrusive biosensor to enable minimally invasive, low cost human telemetry (Fig. 1.1). This device can perform electrochemical measurements by means of microfabricated electrodes [18]. Thus, real-time monitoring of the patients can be performed without invasive methods of analysis. An integrated logic unit is designed in 0.18 μm CMOS technology to drive these electrodes, each of which is dedicated to the detection of a specific compound, and to perform several types of measurements, such as cyclic voltammetry, chronoamperometry, temperature and pH detection [19].

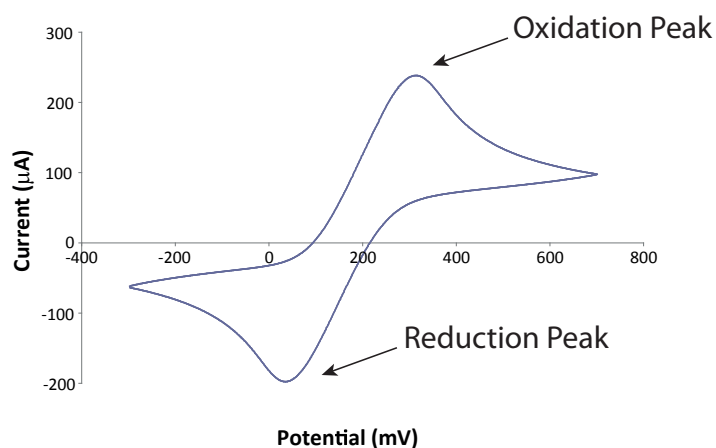


Figure 1.2: Example of voltammogram obtained with cyclic voltammetry. Elaborated from [22].

In a cyclic voltammetry measurement, a linearly varying potential is applied between the electrodes. By changing the potential, a point is reached in which oxidation (loss of electrons by the compound) takes place. The compound oxidation generates a current that is continuously monitored. The graphic of the current against the potential (named voltammogram) shows a positive peak while the oxidation potential is reached. In case of reversible reactions, as the potential sweeps back towards the reduction potential, the oxidized species will start to be reduced. The current reported in the voltammogram will now increase in the negative direction until a reduction peak is reached. An example of voltammogram is reported in Fig. 1.2. The peaks of current have almost the same height. The areas underneath the peaks return the compound concentration, whereas the peak position and their distance are related to the species involved in the reaction. If the reverse peak has a different or distorted shape, or is not present at all, the reaction is not completely reversible or is not reversible at all.

In a chronoamperometry measurement, the potential applied between the cell electrodes is stepped to the oxidation (or reduction) potential. The current through the cell shows a peak while the potential is stepped and then decreases exponentially. The asymptotic value of the current, when a steady-state is reached, is directly related to the compound concentration. Temperature and pH sensibly affect the results obtained with these measurements [21]. Thus, temperature and pH sensors have been included to calibrate the results obtained.

1.1.2 Requirements

Besides the sensing aspects, related to the electrochemistry domain, the implantable device previously introduced must respect several constraints. It must be minimally invasive, completely biocompatible, with low thermal dissipation, and large power autonomy. This last requirement should be carefully considered, since battery size and battery lifetime strongly affect the performance and the invasivity of an implantable sensor. Modern batteries have increased capabilities with respect to those available in the past: for example, lithium-ion

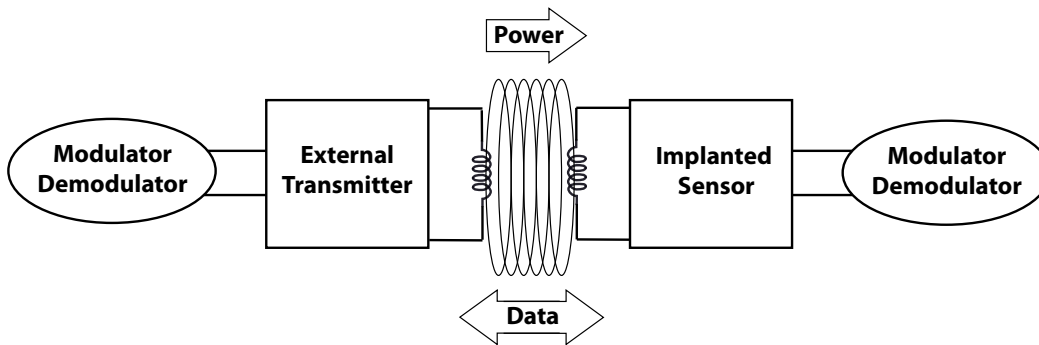


Figure 1.3: Schematic representation of an inductive link performing remote powering and bidirectional data communication.

batteries have reached a high level of energy density (up to 0.2 Wh/g) and are able to maintain an almost constant voltage until they are discharged to 75%-80% [23]. Unfortunately, size constraints of implantable batteries limit their efficiency and their repeated use implies their substitution after a while.

Power constraints can be relaxed by energy harvesters, also named energy scavengers. These devices exploit natural or artificial power sources surrounding the person to assist the implanted batteries, to recharge them and in certain cases even to replace them. Energy harvesters for implantable biosensors have been exhaustively studied and a large number of solutions for different cases can be found in the literature. Most of the physical phenomena have been studied to obtain harvesters suitable for in-body applications, having minimum invasivity and high efficiency. Previously developed harvesting techniques for implantable biosensors, surveyed in [24], are reported in Chapter 2.

Among these approaches, the remote powering through inductive link is one of the most promising. In such a technique, near-field magnetic induction is used to transfer power wirelessly through the body tissues. An alternate current is forced into an external inductor; the variable magnetic field generated induces an alternate current into one or more receiving inductors (Fig. 1.3). Moreover, inductive links enable bidirectional data communication with the implanted sensor without using an implanted RF transmitter. Downlink communication (from the external system to the implanted sensor) can be achieved by modulating the power carrier; uplink communication (from the implanted sensor to the external system) can be obtained by modulating the load of the receiving coil (*Load Shift Keying* - LSK).

This harvesting technique has been studied since several decades. Several solutions have been proposed in the literature [25–34] and it has already reached the market with commercial products [35]. Nevertheless, the miniaturization process of the receiving inductor, the wearability of the transmitting unit and its remote control by means of portable devices are still open research topics.

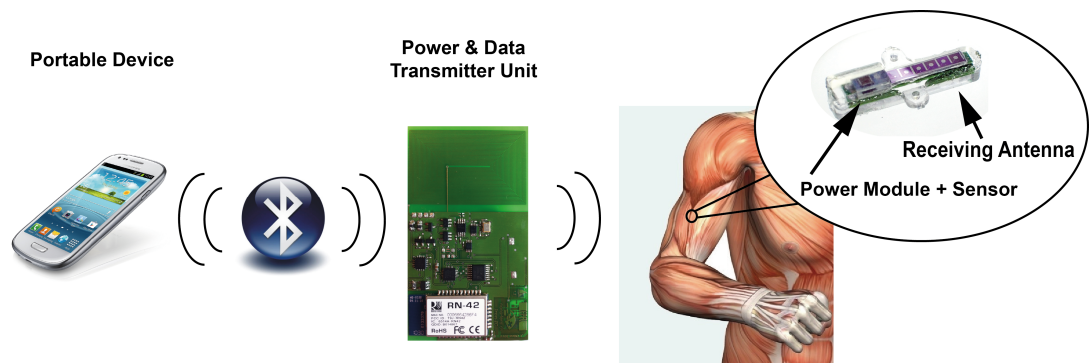


Figure 1.4: A platform has been conceived to provide remote powering and data communication to the implantable system.

1.1.3 Remote Powering and Data Communication

The contribution of this research work to the i-IronIC project consists of the design and realization of a complete platform to provide power, data communication and remote control to the implantable biosensor shown in Fig. 1.1. High wearability of the transmitting unit, low invasivity of the receiving inductor, integration of the power management module within the sensor, and a reliable communication protocol with portable devices are the key points of this platform. The schematic view of the different blocks composing the platform is reported in Fig. 1.4.

The design of the receiving inductor is a critical step of the platform design. The miniaturization of this element reduces the discomfort of the patient and eases the implantation process. However, smaller receiving inductors generally involve lower link efficiency. Starting from the literature, different approaches have been tested to realize the receiving inductor. Multi-layer spiral inductors on printed circuit boards and microfabricated inductors have been studied, fabricated and tested to check their performance within a real setup [36]. The simulations are reported in Chapter 3 together with the frequency and geometry optimization. The fabrication and the measurement of these inductors are described in Chapter 4.

A wearable, flexible transmitting unit, named IronIC patch, is designed to be placed directly over the implantation area and provide power transmission and bidirectional data communication with the implanted device through inductive link [36]. A careful study has been done to select the geometry of the external transmitting inductor [37, 38], in order to reduce the tissue absorption and maximize the link efficiency. Powered by lithium-ion polymer batteries, the patch can be placed in concave or convex parts of the body, thus reducing misalignments with the implanted receiving inductor. Finally, connectivity with portable devices has been enabled by using Bluetooth protocol. The design and realization of this device are deeply described in Chapter 5. The Bluetooth protocol and the user interface are reported in Chapter 6.

Once delivered to the sensor, power needs to be properly stored and managed. Moreover, a communication unit is needed to enable bidirectional data communication with the external

transmitter unit. These functionalities (power management, power storage, and data communication) have been implemented in a $0.18\ \mu\text{m}$ CMOS circuit to be integrated within the sensor. Voltage rectifier, low-dropout regulator (designed by [39]), amplitude demodulator and load modulator are included in that circuit. Simulations and measurements within a real setup are described in Chapter 7.

1.2 Research Contribution

This thesis is both a research and an implementation work. On the research side, every block of the i-IronIC chain of Fig. 1.4 has been designed starting from the state of the art presented in the literature, with the aim to offer a novel and original contribution. On the implementation side, this work provides practical solutions to design, develop and manufacture four out of five blocks of the i-IronIC platform: long-range communication with remote devices, power and data transmitter unit, receiving antenna, and integrated power management module.

Wearable sensor-based systems for medical aims have been already presented in the literature [40]. Flexible systems to be worn around the wrist for the monitoring and the evaluation of vital signs have been reported by [41] and [42]. Wearable devices for the pulse oximetry have been presented by [43] and [44]. A flexible and stretchable ECG patch to monitor the heart activity has been proposed by [45], while a system based on a textile wearable interface to simultaneously acquire different biomedical signals is presented by [46]. Different from these approaches, the power and data transmitting unit presented in this thesis is not directly involved in the sensing process, but offers a novel approach to transmit power and data through the body tissues by means of a wearable device.

The multi-layer approach proposed for the receiving antenna has been conceived to reduce the size of classic “pancake” inductors or single-layer inductors used for wireless power transfer [25–27,31–33]. Multi-layer approaches have already been presented in the literature [47–49]. The design of multi-layer inductors reported in this thesis starts off from those works to further investigate the effects of the spiral geometries on the link efficiency while multi-layer structures are used. The fabrication and measurement of multi-layer inductors and the effects of their geometry on the link efficiency and voltage gain are a novel contribution to the literature. Furthermore, a novel asymmetrical shape of the inductor is investigated to ease the implantation process.

The microfabrication of the receiving antenna directly on the silicon substrate hosting the sensor is presented as an alternative to the multi-layer approach. Several solutions have been proposed in the literature for the microfabrication of spiral inductors on flexible substrate [50] or silicon [51–53]. Starting off from these works, a microfabrication process has been proposed to design high-thickness spiral inductors on several substrates, such as silicon and pyrex. The realization of high-thickness structures with a single photoresist deposition is a practical contribution to the existing literature.

1.3 Organization of the Thesis

Following the Introduction, the remainder of the thesis is organized as follows:

Chapter 2 introduces the most popular techniques for energy harvesting and power transfer dedicated to implantable biosensors. For each technique, the advantages and the drawbacks are discussed. Emphasis is placed on the inductive links, able to deliver power wirelessly through the biological tissues and to enable bidirectional data communication with the implanted sensor.

Chapter 3 describes the design of the inductive link. The modeling of the transmitting and receiving inductors is reported here. Simulations are performed to achieve frequency and geometry optimization. The possibility to work in the low megahertz range, where tissue absorption is minimum, while dealing with small receiving antennas is also discussed. Finally, a model is presented to calculate the electrical parameters of the receiving inductor starting from its geometry.

Chapter 4 describes and motivates the design and fabrication of multi-layer inductors and microfabricated spiral inductors. Both the approaches have been proposed to minimize the size of the implant, while preserving the link efficiency. Simulations and measurements are presented to support these two approaches and to enable a comparison with the state of the art.

Chapter 5 reports the design and development of the power and data transmitter unit. The IronIC patch, designed to be placed directly over the implantation zone to remotely power the implantable system, is described here. The patch is battery powered and is capable to provide power to the implanted system by means of an inductive link. Furthermore, it enables bidirectional short-range communication with the implanted sensor and long-range communication with portable devices, such as smartphones and tablets.

Chapter 6 describes the Android application designed to communicate with the IronIC patch. The application, based on Bluetooth protocol, is described in detail and tested with a custom hardware for glucose and lactate detection in cell cultures. The user interface, running on portable devices, such as smartphones and tablets, enables real-time and continuous monitoring of the patient.

Chapter 7 describes the integrated power module, reporting the simulations and the measurements performed to test and validate the circuit. The integrated circuit reported here includes a voltage rectifier, a low-dropout regulator (designed by [39]), an ASK demodulator for downlink communication and an LSK modulator for uplink communication.

Chapter 8 concludes the thesis with an indication of future developments and possible research directions.

2 Energy Harvesting and Remote Powering for Implantable Biosensors

The most popular harvesting techniques for implantable biosensors are introduced in this chapter, discussing for each technique the state of the art, the advantages, and the disadvantages. An outlook of some new emerging techniques, inspired by biological mechanisms, is also proposed. Finally, a special focus is dedicated to the remote powering and data communication through inductive link. This technique has finally been chosen to provide power and data communication to the implantable sensor.

2.1 Kinetic

Kinetic harvesters aim to collect the energy related to human motions and convert it into electrical energy [54]. These kinds of harvesters can be classified into three categories, depending on the employed transduction method: electromagnetic, electrostatic, and piezoelectric.

Kinetic harvesters using electromagnetic transducers are able to generate an electromotive force due to the change of an external magnetic flux through a closed circuit. The change of flux can be induced, for instance, by rotating the circuit along an axis, thereby changing the surface associated with the magnetic flux. This method has been used by Seiko to power the quartz wristwatch “Seiko Kinetic” [55]. This watch is able to self-charge by the means of wrist motion, transmitted by an oscillating weight to a magnetic rotor linked to a coil [56]. The motion of the rotor induces an electromotive force through a coil and the generated charge is stored in a standard battery. Moreover, this harvester is equipped with a charge pump circuit with different multiplicative factors to quickly increase the voltage of the battery, in order to reduce the start-up time of the watch as much as possible. The approach of Seiko has been successfully tested in the biomedical field, being able to exploit the heart beats to charge a pacemaker battery [57]. Implanted on a dog, this energy harvester has collected 80 mJ after 30 min with a cardiac frequency of about 200 beats/min: around 13 μJ per beat with a returned power of about 44 μW . A possible drawback of this technique is the necessity to periodically lubricate the moving parts which, in the end, need to be replaced when worn out. Moreover, the oscillating weight makes this solution not suitable for implantable biosensors.

Kinetic harvesters based on electrostatic transducers utilize variable capacitors having the position of the plates changed by an external force. They can work with fixed charge or fixed voltage. Working with fixed charge, the external force changes the voltage across the capacitor, while working with fixed potential the motion of the plates generates current through the capacitor. Independent of the operation mode, in most cases they need to be precharged to operate. This technique has low efficiency when high power is required, but works quite well with devices having low power requirements, such as the implantable biosensors. Furthermore, it is appropriate for MEMS realization. The literature offers kinetic harvesters with electrostatic transducers that can render up to 58 μW when set in motion by a force emulating the cardiac signal, exploiting a capacitor with a capacitance variable between 32 nF and 110 nF [58]. A MEMS electrostatic harvester rendering 80 μW when excited with an acceleration of 10 m/s^2 has been proposed [59]. This harvester is dedicated to biomedical applications and operates with constant charge; moreover it is non-resonant, thus it can operate over a wide range of oscillation frequencies.

Finally, the kinetic harvesters based on piezoelectric transducers use the capability of the piezoelectric materials to generate an electric field when subjected to mechanical deformation. Different from the electrostatic transducers, no precharging is required. Piezoelectric harvesters based on *Aluminum Nitride* (AlN) have returned up to 60 μW , with a footprint smaller than 1 cm^2 [60]; this power, however, is obtained with unpackaged devices and could significantly decrease once the harvesters are packaged; Piezoelectric harvesters based on *Lead Zirconate Titanate* (PZT) have obtained up to 40 μW [61].

Kinetic harvesters are widely used in commercial sensors available in the market. Perpetuum [62] and EnOcean [63] provide a large spectrum of solutions for different application fields, including wireless sensor nodes. None of these commercial solutions is however dedicated to implantable biosensors.

2.2 Thermoelectric Effect

Scavengers exploiting thermal gradients to generate energy are based on the Seebeck effect. Due to a temperature difference between two different metals or semiconductors, a voltage drop is created across them.

The core element of this kind of scavengers is the thermocouple (Fig. 2.1). Two materials are linked together, maintaining their junctions at different temperatures. The voltage generated across a thermocouple due to a temperature difference ($T_1 - T_2$) can be expressed as

$$V = \int_{T_1}^{T_2} [S_B(T) - S_A(T)] dT , \quad (2.1)$$

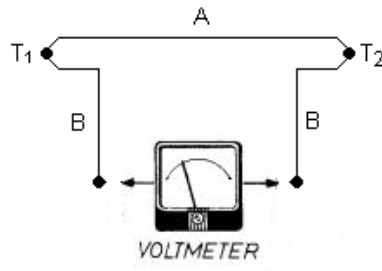


Figure 2.1: Schematic representation of a thermocouple: two materials are linked together keeping their junctions at different temperatures. A voltage drop is thus created across them because of the Seebeck effect. Reprinted from [24].

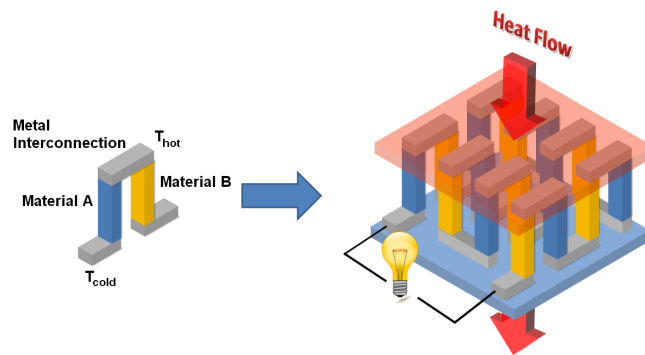


Figure 2.2: The connection of many thermocouples (left) electrically in series and thermally in parallel forms a thermopile (right). Reprinted from [24].

where S_A and S_B are the thermoelectric powers (or Seebeck coefficients) of the two materials A and B. Semiconductors typically have a high Seebeck coefficient and that is why these materials are commonly used for thermocouples. Moreover, n-type and p-type semiconductors have Seebeck coefficients with different signs; thus, if the two semiconductors composing a thermocouple have opposite doping, the contributions to the voltage reported in (2.1) are summed.

Energy scavengers exploiting the thermoelectrical effect consist of many thermocouples connected electrically in series and thermally in parallel to create a thermopile (Fig. 2.2). Additional elements, such as radiators and structures to convey the heat into the thermopile legs are normally used to increase the efficiency of these devices.

Thermopiles are usually inserted in a thermal circuit as depicted in Fig. 2.3. If we assume that the thermopile is placed between the human body (source) and the external ambient (sink), R_{sr} represents the thermal resistance during a heat exchange between the hot plate of the thermopile and the body, while R_{sk} represents the thermal resistance during a heat exchange between the cold plate of the thermopile and the ambient. The temperature difference

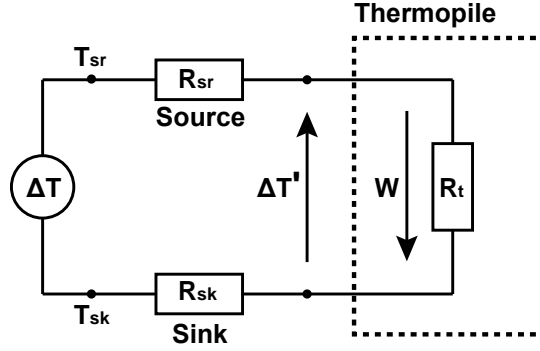


Figure 2.3: Schematic example of a thermal circuit. Reprinted from [24].

between the body and the ambient is denoted as ΔT , while $\Delta T'$ is the temperature difference that is effectively present across the thermopile plates. The thermopile has a thermal resistance between the plates equal to R_t and a heat flux W flows across it. In this description, the heat flux is considered constant. This assumption remains valid only for high values of the thermal resistances R_{sr} and R_{sk} .

The thermal resistance R_t of the thermopile is the parallel combination of the thermal resistance R_p of the thermopile legs, also called pillars, and the thermal resistance R_a of the air in between the legs

$$\begin{cases} R_p = \frac{h}{2na^2}r_p, \\ R_a = \frac{h}{A-2na^2}r_a, \end{cases} \quad (2.2)$$

where A is the area of the thermopile plates, h is the height of the pillars, equal to the distance between the plates, and a is the lateral dimension of the pillars, assumed with square base. The parameter n represents the number of thermocouples (each one having two pillars) while r_a and r_p are the thermal resistivity of the air and of the pillars, respectively.

It is possible to demonstrate that R_p and R_a should be equal to maximize the generated power [64]. Thus, by equalizing the two previous expressions, the optimum number of thermocouples to be used in a thermopile is obtained

$$n = \frac{r_p}{r_p + r_a} \cdot \frac{A}{2a^2} = \frac{r_p}{R_a} \cdot \frac{h}{2a^2}. \quad (2.3)$$

The thermal gradient $\Delta T'$ across the thermopile can be written as

$$\Delta T' = WR_t = W \frac{R_p}{2}, \quad (2.4)$$

where the thermal resistance of the thermocouple R_t is the parallel of R_p and R_a . The thermal resistance R_p has been fixed equal to R_a to maximize the generated power.

The electrical parameters of the thermopile can be determined as

$$\begin{cases} \Delta V = nS_p \Delta T' = r_p \frac{S_p W}{4} \cdot \frac{h}{a^2}, \\ R = 2n\rho \frac{h}{a^2} = \frac{r_p}{r_p + r_a} \cdot \frac{\rho A}{h} \cdot \left(\frac{h}{a^2}\right)^2. \end{cases} \quad (2.5)$$

The first equation of (2.5) returns the voltage drop across the entire thermopile and is obtained from (2.1) by considering S_p as the sum of the Seebeck coefficients of the two pillars of every thermocouple. The second equation of (2.5) describes the electrical resistance R of the thermopile, where ρ is the electrical resistivity of the pillars.

Finally, the power delivered by the thermopile to a matched load is equal to

$$P = \frac{\Delta V^2}{4R} = \frac{1}{64} \frac{S_p^2 W_u^2 A h}{\rho} (r_p + r_a) r_p, \quad (2.6)$$

where $W_u = W/A$ is the heat flux per unit area. A common figure of merit for the thermopiles is the following

$$ZT = \frac{S_p^2 r_p}{\rho} \Delta T', \quad (2.7)$$

where ZT is a dimensionless factor describing the performance of a thermocouple.

With the formulas just introduced, the voltage V is shown to be proportional to h/a^2 , while the power P is proportional to h . The aspect h/a between the height of the pillars and the lateral dimension is limited by technology aspects [65]. Thus, by increasing h to obtain higher power, h/a^2 is decreased and, hence, the voltage. For this reason, there is no space for simultaneously optimizing of power and voltage.

Table 2.1: Human temperature gradients at room temperature. Table from [66].

Site	Muscle Thickness (mm)	Fat Thickness (mm)	Rested (v=0.2 m/s) $\Delta T(K)$	Walking (v=1.56 m/s) $\Delta T(K)$	Running (v=4.25 m/s) $\Delta T(K)$
Abdomen	16.34	14.8	1.73	3.8	4.75
Biceps	34.6	3.33	0.45	1.22	1.7
Calf-posterior	65.36	4.93	0.65	1.74	2.4
Chest	33.45	7.26	0.94	2.37	3.18
Forearm	26.04	3.24	0.44	1.16	1.63
Hamstring	69.29	6.97	0.91	2.32	3.14
Lumbar	37	6.54	0.85	2.18	2.96
Quadriceps	54.54	6.42	0.82	2.12	2.89
Subscapular	23.74	8.4	1.06	2.6	3.44
Suprapatellar	29.42	6.23	0.81	2.08	2.81
Triceps	41.84	5.92	0.78	2.02	2.75

When low thermal gradients are applied, as in the case of human body applications, it is not straightforward to obtain voltage levels sufficient to power integrated circuits. Commercial thermopiles commonly use bismuth telluride (Bi_2Te_3), having a Seebeck coefficient $S = \pm 0.2 \text{ mV}/^\circ\text{C}$, due to the high ZT factor. By using that material for the thermocouple pillars, with a temperature difference $\Delta T' = 1^\circ\text{C}$, 5000 thermocouples having a total area of about 25 cm^2 are required to produce a voltage drop $\Delta V = 1 \text{ V}$ [64].

Moreover, a value of $\Delta T' = 1^\circ\text{C}$ between the thermopile plates is not easily achieved. Based on results from [64], placing a commercial thermopile exploiting bismuth telluride on a human forearm and considering an area $A = 1 \text{ cm}^2$, we can assume as reasonable the following values: $R_{sr} = 500 \text{ K/W}$, $R_{sk} = 1030 \text{ K/W}$, $R_t = 50 \text{ K/W}$, $T_{sr} = 37.5^\circ\text{C}$, $T_{sk} = 28^\circ\text{C}$. If the heat flux W passing through the thermopile is

$$W = \frac{\Delta T}{(R_{sr} + R_{sk} + R_t)}, \quad (2.8)$$

a heat flux of about $W = 6 \text{ mW}$ flows through the area A . The product of the heat flux by the thermal resistance of the thermopile results in temperature gradient $\Delta T' = 0.3^\circ\text{C}$, instead of 1°C previously assumed. With this value of $\Delta T'$, the thermopile area must be increased up to 83 cm^2 to obtain a voltage drop of $\Delta V = 1 \text{ V}$, making impractical any kind of implant application. In order to compare the different implantation areas, Table 2.1 shows calculated temperature gradients in different parts of the human body, with an ambient temperature of 25°C .

Charge pumps are commonly used to increase the voltage drops generated by the thermocouples, thus overcoming the problems related to the low voltages generated by the thermal scavengers [67–70]. Seiko proposed a thermoelectric wristwatch where a voltage of about 300 mV is boosted until 1.5 V, a useful level to power the 1 μ W quartz circuit [71]. The whole scavenger can provide a total power of 22.5 μ W.

The literature offers some examples of thermopiles exploiting the human warmth and considerable effort has been invested to improve the performance of these systems. However, the power range of thermoelectric harvesters when exploiting the human warmth is still quite low and generally does not exceed the few hundreds of microwatts when thermal differences below 5 K are applied. In [72], 1.5 μ W with a 0.19 cm³ device exploiting a thermal gradient of 5 K is obtained. Similar results have been obtained by [73] with a device that is able to deliver 1 μ W with an area of 1 cm² and a thermal gradient of 5 K. ThermoLife [74] proposes a commercially available solution that is able to produce up to 30 μ W (10 μ A with a voltage drop of 3 V) when a temperature difference of 5 K is applied. This device has a volume of 95 mm³ and a weight of 0.23 g.

2.3 Fuel Cells

A fuel cell is an electrochemical device that generates current through the reaction of two chemical species flowing into it, the fuel on the anode site and the oxidant on the cathode site. The main difference between a fuel cell and a traditional battery is that the former can produce energy virtually without stopping, as long as the reactants continue to be present.

Fuel cells exist in many different kinds. The most common is the *Proton Exchange Membrane* (PEM) fuel cell (Fig. 2.4). The fuel and the oxidant streams are separated by a membrane that allows only protons produced on the anode site to cross it and to reduce the oxidant on the cathode site. The electrons generated on the anode cannot pass directly through the membrane to reach the cathode; consequently, they have to follow a different external path, generating current.

Recently, a new kind of membrane-less fuel cells has been introduced [75, 76]. They exploit the laminar characteristics of micro-channel flows to keep the two reactants separated, thus avoiding the use of a membrane. Indeed, the PEM membrane needs constant humidification and it is subject to degradation and fuel crossover. In addition, the cost is usually quite high. Membrane-less fuel cells, instead, are more compact and enable significant miniaturization. Also, they do not require water management or cooling system. A schematic example of a membrane-less fuel cell is reported in Fig. 2.5.

The use of fuel cells exploiting species present into the human body to harvest energy for implantable biosensors offers considerable advantages. The constant presence and availability of the reactants directly into the body makes unnecessary external recharging mechanisms or replacement. Implantable fuel cells that use glucose as reactant are probably the most

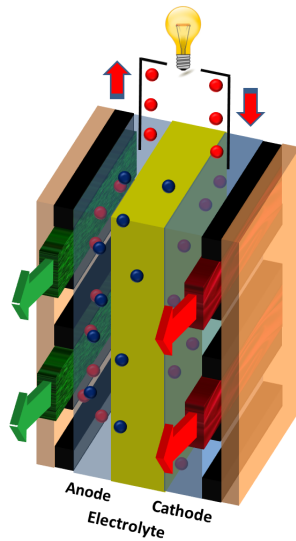


Figure 2.4: Schematic description of a PEM fuel cell. Electrons cannot cross the membrane. They have to follow a different path, thus generating current. Reprinted from [24].

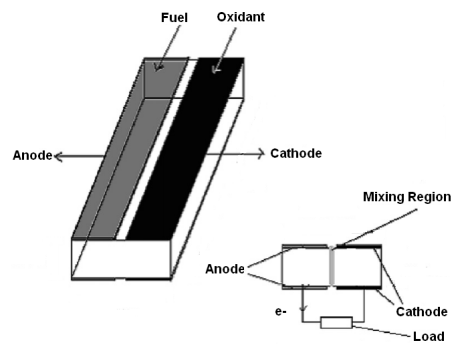


Figure 2.5: Schematic description of a membrane-less fuel cell. The laminar characteristics of micro-channel flows are used to keep reactants separated. Elaborated from [83].

studied biofuel cells, due to the high availability of glucose in body fluids. The investigation and development of these cells began in the 1960s [77].

Glucose fuel cells can be divided into two groups: *abiotically catalyzed* and *enzymatically catalyzed*. The former group utilizes non-biological catalysts, such as noble metals or activated carbon. The latter group, instead, uses enzymes, such as glucose oxidase or laccase, as catalysts to enable the electrode reactions. In [78], the state of the art of these devices is reported. During *in vitro* experiments, glucose fuel cells abiotically catalyzed can generate up to $50 \mu\text{W}/\text{cm}^2$ [79]. Experiments *in vivo* performed on a dog have generated $2.2 \mu\text{W}/\text{cm}^2$ over a period of 30 days [80]. Enzymatically catalyzed cells can provide a higher power density, up to $430 \mu\text{W}/\text{cm}^2$ [81]. Unfortunately, the lifetime of their enzymatic catalyst has not been proved beyond a period of one month [82].

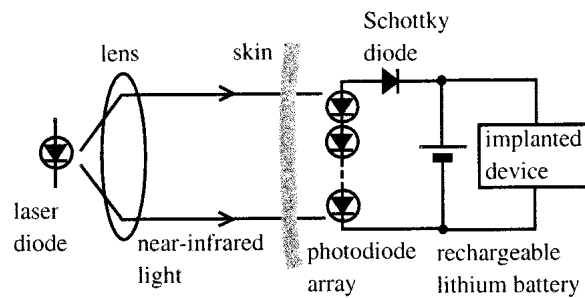


Figure 2.6: Example of an IR harvester. The IR light emitted by an external source is caught by an implanted photodiode array. Reprinted from [85].

2.4 Infrared Radiation

These kinds of harvesters exploit an external *infrared* (IR) source to transmit power to an implanted photodiode array. This array converts the received radiation into a current to properly charge the sensor battery (Fig. 2.6).

Some examples of this typology of scavengers are discussed in [84, 85]. The device presented in [85] can supply power in the order of hundreds microwatts up to few milliwatts when illuminated by a power density of some milliwatts per square centimeter. The power returned by that photodiode array when enlighten by a power density of 22 mW/cm^2 for 17 min is sufficient to enable a $20 \mu\text{A}$ cardiac pacemaker to operate for 24 h. In terms of power, it means about 4 mW of transmitted power if the voltage of the pacemaker battery is considered equal to 2.4 V. This result has been obtained with a skin temperature rise of 1.4°C , a safe value for this kind of tissue [86].

This performance has been achieved by means of a large photodiode array, having an area of 2.1 cm^2 and placed in a subcutaneous zone extremely close to the IR emitter (0.8 mm). To obtain the same performance without further temperature increase when a thicker tissue is used, the array size can be enlarged. In [85], the same results are demonstrated where a 2 mm human skin is used as barrier with a 10 cm^2 photodiode array. Finally, increasing the emitter power densities to reduce the photodiode area is not recommended. Most of the heat generated by these scavengers is due to the array heating and a smaller array receiving a greater power density would involve a considerable temperature rise in the implantation zone.

Due to the area constrains and the difficulties of operating with tissues having high thickness, these kinds of harvesters are suitable for large devices not deeply implanted (i.e., cardiac pacemakers) but are practically ineffective with less invasive, deeply implanted devices.

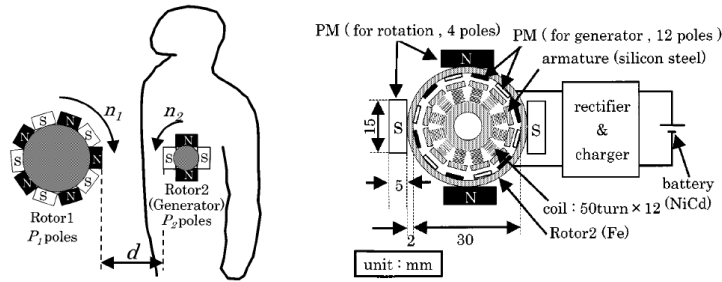


Figure 2.7: Low frequency magnetic fields are used to move an implanted rotor to generate power. Elaborated from [88].

2.5 Low Frequency Magnetic Fields

These kinds of harvesters use low frequency magnetic fields generated outside the body to move an implanted magnetic rotor and to harvest power exploiting its mechanical rotation (Fig. 2.7). Some solutions using this technique have been reported in literature [87, 88].

One of the advantages in employing these kinds of scavengers is the high quantity of power that they can deliver over a relatively long distance and even to deeply implanted biosensors. A maximum power of 3.1 W over a distance of 1.5 cm has been reported in [88], with an attractive force between the external and the internal rotors of 1.6 N. This value has been obtained with a speed of the internal rotor of about 547 rad/s. At a lower speed, up to 0.2 W can be delivered over a distance of 2 cm when the implanted rotor rotates at 273 rad/s and the resistance of the load is 200 Ω .

The major drawback of this technique is the large size of the implanted rotor, about 10 cm³. This volume hinders the implantation process. Moreover, moving components need to be periodically lubricated and substituted when worn out.

2.6 Emerging Techniques

The biological processes in animals and plants to collect, store and reuse energy can inspire novel harvesting techniques. Some works have presented strong analogies between complex electronic systems and biological energy management [89].

For example, natural photosynthesis permits plants to collect energy by exploiting the solar light as source and CO₂ and water as reactants. Several efforts have been invested to artificially reproduce the key steps of the photosynthesis, in order to generate electrical power and energy fuels [90, 91]. Ref. [92] has proposed a photosynthetic light conversion unit that mimics the light-harvesting structure of phototrophic bacteria. An array of self-assembled bacteriochlorophyll aggregates captures and conveys the solar energy to an embedded “reaction center”. This element has the role of energy acceptor and contributes to the charge transfer.

Another kind of scavenger inspired by the natural photosynthesis is the Grätzel's cell or *Dye-Sensitized Solar Cell* (DSSC) [93]. This device has two electrodes, one of which is transparent to the solar light. In between the two electrodes, a molecular dye converts the solar light in electrons that reach the anode electrode by means of a stratum of titanium dioxide (TiO₂). The electron holes generated into the dye reach the cathode electrode through a liquid electrolyte. The whole mechanism is similar to the natural photosynthesis. Indeed, in this approach the dye has the same role of the chlorophyll (conversion of light in electrons), the electrolyte has the same role of the water (replacement of the generated electrons), and the TiO₂ has the same role of the CO₂ (electrons acceptor).

This harvesting technique, although at the moment is not directly applicable to the field of implantable biosensors, could be used in the near future to power devices not deeply implanted. A possible target, for example, could be subcutaneous biosensors due to their proximity to the skin and to the solar light.

2.7 Inductive Link

2.7.1 Inductive Link Description

The use of inductive links to power implanted sensors has been deeply investigated in the last decade. An inductive link usually consists of two coils. The primary coil is placed outside the body, generating a variable magnetic field by means of an alternate current flowing in it. The change of the magnetic flux through the secondary coil generates an electromotive force across it, according to the Faraday-Neumann-Lenz law

$$\varepsilon = -\frac{d\phi_B}{dt}, \quad (2.9)$$

where ε is the electromotive force generated by the change of the magnetic flux ϕ_B through the secondary coil. The minus sign in the right side of the equation indicates that the generated electromotive force opposes the flux change. Using this method, power is transferred wirelessly through the body tissues, inducing an electromotive force in the implanted coil by means of an alternate current flowing on the external coil.

An example of inductive link is reported in Fig. 2.8. The behavior of that circuit is described, according to (2.9), by the following formulas

$$\begin{cases} V_1 = +R_1 I_1 + \frac{d\phi_1}{dt}, \\ V_2 = -R_2 I_2 - \frac{d\phi_2}{dt}, \end{cases} \quad (2.10)$$

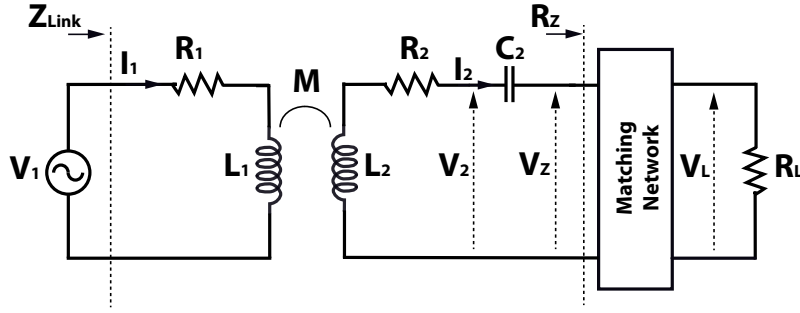


Figure 2.8: An inductive link is obtained with a primary coil L_1 connected to a power source and magnetically coupled to a secondary coil L_2 . Reprinted from [24].

where R_1 and R_2 represent the parasitic resistances of the two coils, ϕ_1 is the total magnetic flux through the primary coil, and ϕ_2 is the total magnetic flux through the secondary coil. The voltages and the currents reported in (2.10) are functions of time.

Defining the self-inductances L_1 and L_2 of the two coils and their mutual inductance M as

$$\begin{cases} L_1 = \frac{\partial \phi_1}{\partial I_1}, \\ L_2 = \frac{\partial \phi_2}{\partial I_2}, \\ M = \frac{\partial \phi_1}{\partial I_2} = \frac{\partial \phi_2}{\partial I_1}, \end{cases} \quad (2.11)$$

the expressions in (2.10) can be rewritten as

$$\begin{cases} V_1 = +R_1 I_1 + L_1 \frac{dI_1}{dt} - M \frac{dI_2}{dt}, \\ V_2 = -R_2 I_2 - L_2 \frac{dI_2}{dt} + M \frac{dI_1}{dt}. \end{cases} \quad (2.12)$$

The system can be finally described in the frequency domain by

$$\begin{cases} V_1 = +R_1 I_1 + j\omega L_1 I_1 - j\omega M I_2, \\ V_2 = -R_2 I_2 - j\omega L_2 I_2 + j\omega M I_1, \end{cases} \quad (2.13)$$

where V and I represent now complex phasors.

Link Efficiency

The efficiency η of an inductive link is defined as the ratio between the power dissipated on the load and the total dissipated power. We report here the analytical formulas presented in [94] to describe the link efficiency η as a function of the electrical parameters of the link. By defining η_1 as the power dissipated on the secondary circuit over the totally dissipated power

$$\eta_1 = \frac{\omega^2 M^2}{\omega^2 M^2 + R_1(R_2 + R_Z)} , \quad (2.14)$$

and η_2 as the power dissipated on the load over the power dissipated on the secondary circuit

$$\eta_2 = \frac{R_Z}{R_Z + R_2} , \quad (2.15)$$

the link efficiency η can be written as

$$\eta = \eta_1 \eta_2 = \frac{\omega^2 M^2 R_Z}{\omega^2 M^2 (R_2 + R_Z) + R_1 (R_2 + R_Z)^2} . \quad (2.16)$$

By defining the coupling coefficient k as

$$k = \frac{M}{\sqrt{L_1 L_2}} , \quad (2.17)$$

and the quality factor Q as

$$Q = \frac{\omega L}{R} , \quad (2.18)$$

the efficiency reported in (2.16) can be rewritten as

$$\eta = \frac{k^2 Q_1 Q_2 \frac{R_2}{R_Z}}{\left(1 + \frac{R_2}{R_Z} + k^2 Q_1 Q_2 \frac{R_2}{R_Z}\right) \left(1 + \frac{R_2}{R_Z}\right)} . \quad (2.19)$$

Chapter 2. Energy Harvesting and Remote Powering for Implantable Biosensors

The ratio between the intrinsic resistance R_2 of the internal inductor and the load R_Z that maximizes the link efficiency is obtained

$$\frac{\partial \eta}{\partial R_Z} = 0 \implies R_Z = R_2 \sqrt{1 + k^2 Q_1 Q_2}. \quad (2.20)$$

Since

$$\left. \frac{\partial^2 \eta}{\partial R_Z^2} \right|_{R_Z = R_2 \sqrt{1 + k^2 Q_1 Q_2}} < 0, \quad (2.21)$$

the stationary point found in (2.20) is a maximum. The desired R_Z is obtained by properly tuning the matching network in Fig. 2.8.

Finally, by combining (2.16) and (2.20), the maximum link efficiency is described by

$$\eta_{max} = \frac{k^2 Q_1 Q_2}{\left(1 + \sqrt{1 + k^2 Q_1 Q_2}\right)^2}. \quad (2.22)$$

Voltage Gain

The transferred power, although important, is not the only figure of merit of an inductive link. In order to power a load, the supplied voltage must be sufficiently high, according to the load specification. Thus, it is useful to define the voltage gain A as the ratio between the voltage V_Z and the source voltage V_1 . According to [94], the voltage gain A can be written as

$$A = \frac{|V_Z|}{|V_1|} = \frac{\omega M R_Z}{\sqrt{[R_1(R_2 + R_Z) + \omega^2 M^2]^2 + \omega^2 L_1^2 (R_2 + R_Z)^2}}. \quad (2.23)$$

By studying the voltage gain A as a function of the load R_Z , no maximum is found for finite values of R_Z . The voltage gain asymptotically tends to a maximum as R_Z tends to infinity (open circuit).

Data Transmission

In most of the cases, the power signal driving the primary circuit is generated by a class-E amplifier, due to the higher efficiency of this circuit as compared to conventional class-B or class-C amplifiers [95]. Downlink transmission can be achieved by modulating the power signal generated by the class-E amplifier. *Amplitude Shift Keying* (ASK) is one of the most preferred modulation techniques, due to the simplicity of the demodulator that permits to reduce the area and the power consumption of the implanted chip. In addition, this kind of modulation enables a simple synchronization between transmitter and receiver. On the other hand, by modifying the amplitude of the power signal, the transmission efficiency becomes sub-optimal. Furthermore, the data-rate is lower when compared with other kinds of downlink modulations. Another solution for downlink communication is the *Frequency Shift Keying* (FSK). It enables to reach higher data-rate when compared to the ASK, but this result is achieved by means of a more complex demodulator and by increasing the difficulty of synchronization between transmitter and receiver [96].

Uplink transmission is commonly achieved by means of the *Load Shift Keying* (LSK). By modifying the impedance of the secondary circuit, the load Z_{link} seen by the primary circuit consequently varies, causing the current flowing on the primary coil to change. This change can be detected by an external demodulator, enabling uplink transmission without any internal RF transmitter.

2.7.2 Inductive Link in the Literature

Inductive links present considerable advantages when compared with other kinds of power transmission previously discussed. Exploiting this technique, data can be transmitted from outside to inside the body (*downlink*) and vice versa (*uplink*) without using an RF transmitter or receiver. This can be feasible by modulating the load of the secondary coil, varying in this way the total load seen by the primary coil. This technique of data transmission, often called *backscattering*, enables saving a large amount of energy by avoiding the use of implanted RF transmitters. Indeed, RF transmitters usually have the highest power consumption among the components of an implantable biosensor. The possibility to avoid implanted RF transmitters, together with a delivered power up to few milliwatts, make this technique particularly suitable for low-invasive, implantable biosensors. Commercial products exploiting inductive links to power implanted biosensors are currently available on the market. One of these products is the neurostimulator “RestoreUltra”, produced by Medtronic [35]. It is a stimulator of the spinal cord and is equipped with a battery that can be recharged from outside avoiding invasive surgeries.

This technique presents strong analogies with the use of RFID passive tags [97]. An RFID passive tag consists of an integrated circuit with memory that is powered by the incidental field generated by a reader. Once powered, the chip generally transmits its identification tag to the reader by means of an RF transmitter or by exploiting the backscattering technique.

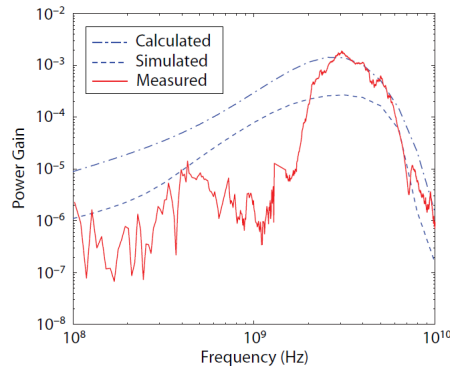


Figure 2.9: Power gain obtained by [98] using an inductive link composed of two 4 mm² coils. Simulations and measurements return an optimal transmission frequency around 2.5 GHz. Reprinted from [98].

Thus, an RFID passive tag needs energy only when the tag is required by the reader and it is not equipped with a battery. Implantable biosensors, instead, could need to be powered even when no reading occurs. Thus, in most cases the biosensors must be equipped with an implanted battery.

Almost all the works reported in the literature utilize frequencies in the order of few megahertz or lower [25–33]. The reason behind this choice is that this range of frequencies minimizes the power absorbed by the tissues, yielding a higher transmission efficiency. At these frequencies, an inductive link can be analyzed by means of the Kirchhoff's laws using lumped parameters [94]. This method of analysis has been introduced in the previous section.

A recent work has explored the possibility to use extremely small inductors [98]. These geometries involve an optimal frequency in the gigahertz range. In that range of frequencies, to characterize a network in terms of lumped elements, as we have done in the previous section, is difficult and in certain cases intractable. Indeed, in the microwave range it is not always possible to define voltages and currents in a univocal manner. Moreover, the measurement of impedances and admittances, when possible, requires the use of short-circuits or open-circuits, not always easily realizable at high frequency. For these reasons, in the microwave and optical range a description of the networks in terms of scattering parameters is usually preferred [99]. A brief introduction of the scattering parameter theory is given in the Appendix.

Ref. [98] has simulated the performance of an inductive link consisting of two square coils with an area of 4 mm². These coils are separated by a substrate of 1.5 cm (composed of air, 2 mm of skin, 1 mm of fat, 4 mm of muscle, 8 mm of skull and brain). The result obtained is reported in Fig. 2.9. The optimum frequency is located around 2.5 GHz, at least two orders of magnitude higher than the frequencies commonly used for wireless power transmission. Moreover, this result has been validated by measurements using beef sirloin as substrate. However, the value of power gain reported is sensibly lower than those presented by the works previously cited, operating in the low megahertz range.

Other works [100] have shown an increase of the power gain, together with a shift of the optimal frequency in the sub-gigahertz range, where the area of the external coil is increased up to 4 cm². The optimum frequency is still two orders of magnitude higher than the frequencies commonly used. An implantable chip exploiting high frequency power transmission has been presented by [34]. The working frequency is 915 MHz and it can deliver a maximum power of 140 μW at 1.2 V, sending 0.25 W through 15 mm of tissue. The implanted coil has an area of 4 mm², while the transmitting coil has an area of 4 cm².

To recap, a summary of some works that exploit inductive links to power implantable devices is reported in Table 2.2. For each of these, some of the key parameters have been extracted and reported in the table to enable a fast comparison. Missing data in Table 2.2 have not been declared in the literature. In contrast to other harvesting techniques presented before, inductive links are able to deliver a noticeable amount of power (order of milliwatts) while requiring a relatively small area. Furthermore, power can be transferred wirelessly through the body tissues without any physical link that could cause infections or discomfort. In Table 2.3, inductive links are compared with other harvesting techniques previously introduced.

Most of the works presented in Table 2.2 perform data communication between the external devices and the implanted sensors, with data-rates up to few hundreds kilobits per second. Finally, all the works reported in Table 2.2 use frequencies in the order of few megahertz with the exception of the last one, where a frequency in the gigahertz range is used. The amount of power delivered by this last solution and its efficiency are noticeably smaller than the others, but they have been obtained using the smallest implanted coil among those reported in the table.

2.7.3 Health Implication - Specific Absorption Rate

An important parameter to be considered, when the power source is close to the body, is the *Specific Absorption Rate* (SAR) of the tissues

$$\text{SAR} = \frac{\sigma |\mathbf{E}|^2}{\rho} , \quad (2.24)$$

where σ and ρ are the conductivity and the density of the involved tissues, respectively, and $|\mathbf{E}|^2$ is the norm of the incident electric field. The SAR, measured in watts per kilogram, determines the quantity of power absorbed by the tissues and is strictly related to their temperature increase. The SAR is usually calculated as an average over a region of 1 g or 10 g of tissue, depending on the national laws. In the IEEE guideline [101], the SAR limits for a general public exposure are 4 W/kg for any 10 g of tissue of hands, wrists, feet, and ankles; 1.6 W/kg for any 1 g of any other tissue. In the ICNIRP guideline [102], the SAR limits for a general public exposure are 2 W/kg for any 10 g of head and trunk and 4 W/kg for any 10 g of the limbs.

Table 2.2: Implantable devices exploiting inductive links for wireless power transmission. Table from [24].

Ref.	Coil Area ($\lambda = 10 \text{ mm}^2$)	Coil Thickness ($\sigma = 1 \text{ mm}$)	Carrier Frequency	Data Transmission	Bit-Rate	Power Consumption	Efficiency	Distance	Measurement Site	Target Site
[25]	Tx: 7.8 λ Rx: 1.7 λ	Tx: 2 σ Rx: 2.5 σ	4 MHz	Downlink: PWM-ASK Uplink: LSK	Uplink: 125 kbps	90 mW		5 mm	Air	Neural Recording System
[26]	Tx: 196 λ Rx: 31.4 λ	Tx: 9.5 σ Rx: 5 σ	4 MHz	Uplink: LSK	Uplink: 5 ÷ 10 kbps	11 mW		28 mm	Water Bearing Colloids	
[27]	Tx: 13200 λ Rx: 7.9 λ	Tx: 300 σ Rx: 13 σ	1 MHz			150 mW	1% (min.)	205 mm	PVC Barrel	Stomach
[28]	Rx: 10 λ	Rx: 0.035 σ	1 MHz			10 mW	18.9% (max.)	5 mm	Air	Cerebral Cortex
[29]	Tx: 283 λ Rx: 31.4 λ		0.7 MHz	Downlink: ASK Uplink: LSK	Downlink: 60 kbps Uplink: 60 kbps	50 mW	36% (max.)	30 mm		
[30]	Tx: 31.4 λ Rx: 7.9 λ		10 MHz	Downlink: ASK Uplink: BPSK	Downlink: 120 kbps Uplink: 234 kbps	$\approx 22.5 \text{ mW}$ in vitro $\approx 19 \text{ mW}$ in vivo		15 mm	Rabbit	Muscle
[31]	Tx: 196.3 λ Rx: 3.5 λ	Tx: 5 σ Rx: 1.9 σ	5 MHz	Downlink: OOK	Downlink: 100 kbps	$\approx 5 \div 10 \text{ mW}$		40 mm		Neural Stimulator
[32]	Rx: 112.5 λ	Rx: 10 σ	6.78 MHz	Downlink: OOK Uplink: LSK	Uplink: 200 kbps	120 mW	20% (min)	25 mm	Dog Shoulder	Muscular Stimulator
[33]	Tx: 152 λ Rx: 3.2 λ	Rx: 1 σ	13.56 MHz	Uplink: LSK		0.198 mW		40 mm		Subcutaneous Tissue
[34]	Tx: 40 λ Rx: 0.4 λ	Tx: 0.038 σ Rx: 0.038 σ	915 MHz			0.14 mW	0.06% (max)	15 mm	Bovine Muscle	

Table 2.3: Comparison between different harvesting techniques. Table from [24].

Technique	Ref.	Returned Power	Advantages	Drawbacks
Kinetic	[57]	$\approx 44 \mu\text{W}$		Large size ($\approx 7 \text{ cm}^2$).
	[58]	$58 \mu\text{W}$		
	[59]	$80 \mu\text{W}$	Non resonant.	
	[60]	$60 \mu\text{W}$	Size ($\leq 1 \text{ cm}^2$).	
	[61]	$40 \mu\text{W}$	Performance can decrease when packaged.	
Thermoelectric	[71]	$22.5 \mu\text{W}$		Low voltage drop.
	[72]	$1.5 \mu\text{W}$		
	[73]	$1 \mu\text{W}$		
	[74]	$30 \mu\text{W}$		
Fuel Cells	[79]	$50 \mu\text{W}/\text{cm}^2$		<i>In vitro</i> .
	[80]	$2.2 \mu\text{W}/\text{cm}^2$	<i>In vivo</i> .	
	[81]	$430 \mu\text{W}/\text{cm}^2$	High power density.	
Infrared Radiation	[85]	$\approx 4 \text{ mW}$	High power.	Size increases when thick tissues are used (10 cm^2 for 2 mm of human skin).
Low Frequency Magnetic Field	[88]	up to 3.1 W	Extremely high power over a big distance (up to 2 cm).	Extremely large size (10 cm^3). Moving parts need to be lubricated and substituted when worn out.
	Inductive Links	[26]	11 mW	High quantity of power. Data transmission (except [27, 28]).
[27]		150 mW		
[28]		10 mW		
[29]		50 mW		
[30]		up to 22.5 mW		
[34]	0.14 mW	Extremely small size. Possibility of high data-rate.	Extremely low efficiency. High transmitted power (0.25 W).	

In [103] a large number of cases where people were daily subjected to microwave fields with densities in the order of few milliwatts per square centimeter have been analyzed, without finding any significant health implication. In addition, it reports the trend of SAR on humans with respect to the frequency, when an incident field of 1 mW/cm^2 is applied. The maximum absorption is around 70 MHz, where SAR is equal to 0.225 W/kg . At higher frequencies, around 2.45 GHz, SAR is one order of magnitude smaller, being equal to 0.028 W/kg . This value is comparable with that obtained around 20 MHz, where SAR is equal to 0.015 W/kg .

Recent studies have focused on the neurological effects of microwaves. The head has become the primary focus due to the wide use of electronic devices for mobile communication. With certain kinds of mobile phones, a maximum SAR of 3.72 W/kg , averaged over 1 g of tissues of the head, can be reached at 900 MHz while the mobile phone is transmitting 600 mW [104]. If averaged over 10 g of tissues, the SAR can be 1.99 W/kg . The increase of temperature of the head tissues is included in the range between $0.22 \text{ }^\circ\text{C}$ and $0.43 \text{ }^\circ\text{C}$. These measurements have been performed with a radiated power of 600 mW. Ref. [105] found no positive evidence of risk to the health or the brain related to pulsed or continuous exposure to microwave having power levels typical of GSM communication, such as the ones previously reported.

2.8 Chapter Contribution and Summary

In this chapter we have presented the most common techniques for powering implantable sensors. Kinetic, thermoelectric, fuel-cell based, infrared, and low frequency magnetic harvesters have been studied. For each technique the main key points and drawbacks have been reported together with a description of the state of the art.

Finally, special attention has been dedicated to the remote powering through inductive link. This technique enables wireless power transfer and bidirectional data communication by using the magnetic coupling between an external and an implanted coil. The amount of delivered power, together with the possibility to communicate with the sensor without implanted RF transmitters, make this solution particularly suitable for the i-IronIC platform.

3 Inductive Link for mm-sized Implants: Frequency and Geometry Optimization

Inductive links are widely used for remote powering of implantable biosensors [25–33]. As reported in the previous chapter, in most cases they operate at frequencies below 10 MHz. This upper limit is often proposed to minimize the quantity of power absorbed by the tissues and to increase the link efficiency. Standards related to SAR have been defined by IEEE [101] and ICNIRP [102]. Recent works, based on full-wave analysis [98, 100], have questioned this assumption. Ref. [34] has shown a 4 mm inductor working at 915 MHz, in the microwave range (see Table 2.2). However, the link efficiency is drastically reduced as compared to inductive links operating in the low megahertz range.

In this chapter we study the possibility to operate in the low megahertz range, where tissue absorption is minimum, while assuring a mm-sized receiving inductor compatible with the requirement of the i-IronIC implantable sensor. This is one of the most important contributions of this chapter. Indeed, the possibility to work in a frequency range where tissue absorption is minimum while using a miniaturized receiving inductor paves the way to efficient and unobtrusive implantable devices. The *Industrial, Scientific, and Medical* (ISM) radio band provides standard frequencies for this type of applications. The most commonly used are 6.78 MHz and 13.56 MHz. In this work we did not limit our investigation to these two frequencies and we did not pose constraints on the working frequency of the inductive link.

In the remainder of the chapter, the design of an inductive link is studied starting from the electrical properties of the body tissues. The impact on the link efficiency of several factors (such as coil geometry, implantation depth, and misalignments) is simulated. Finally, the design of both the transmitting and the receiving inductors is described. A mathematical model to calculate the electrical parameters of a spiral inductor starting from its geometry is presented. This model can help the designer to optimize the link efficiency. The results obtained in this chapter have been used to design and fabricate the miniaturized receiving inductors presented in the next chapter.

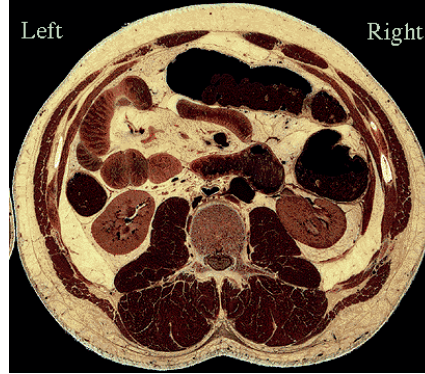


Figure 3.1: Slice of human abdomen obtained with the Visible Human Server [106]. In the slice are visible: spinal cord, kidneys, colon, and small intestine. Reprinted from [37].

3.1 Inductive Link Analysis

Electrical Properties of the Body Tissues

In order to investigate the behavior of an inductive link that remotely powers an implantable device, it is necessary to model the electrical properties of the appropriate human tissues. A large number of tissues have been investigated with the Cole-Cole dispersion model [107]. This model describes the complex permittivity $\hat{\epsilon}$ of a tissue as a function of the angular frequency ω of the incident electromagnetic field

$$\hat{\epsilon} = \epsilon_{\infty} + \sum_n \frac{\Delta\epsilon_n}{1 + (j\omega\tau_n)^{(1-\alpha_n)}} + \frac{\sigma_i}{j\omega\epsilon_0}, \quad (3.1)$$

where τ is a time constant characterizing the polarization mechanism, α is a measure of the broadening of the dispersion, ϵ_0 is the permittivity of the vacuum and σ_i is the static ionic conductivity of the tissue. The term ϵ_{∞} is the permittivity of the tissue at field frequencies where $\omega\tau \gg 1$. Finally, $\Delta\epsilon_n = \epsilon_s - \epsilon_{\infty}$, where ϵ_s is the permittivity of the tissue at field frequencies where $\omega\tau \ll 1$. These parameters are reported in [107] for a large variety of body tissues.

We have investigated different implantation zones by using the Visible Human Server [106], that enables 3D real-time navigation into the human body (Fig. 3.1). Four different locations, such as arm, forearm, abdomen, and leg have been explored with the Visible Human Server and modeled using the Cole-Cole dispersion model [37]. The description of the tissues within these implantation zones is reported in Table 3.1, together with the location of the coils. Then, we have imported the different tissues in the simulation tool Agilent Momentum to perform full-wave analyses in different parts of the human body. The inductive links have

Table 3.1: Implantation sites. Table from [37].

Arm	Forearm	Abdomen	Leg
	<i>External coil</i>		
	<i>Air - 1 mm</i>	<i>External coil</i>	
	<i>Skin - 2 mm</i>	<i>Air - 1 mm</i>	
<i>External coil</i>	<i>Fat - 1.5 mm</i>	<i>Skin - 2 mm</i>	<i>External coil</i>
<i>Air - 1 mm</i>	<i>Air - 1 mm</i>	<i>Fat - 2 mm</i>	<i>Air - 1 mm</i>
<i>Skin - 1.5 mm</i>	<i>Receiving coil</i>	<i>Air - 1 mm</i>	<i>Skin - 2 mm</i>
<i>Fat - 4.5 mm</i>	<i>Air - 1 mm</i>	<i>Receiving coil</i>	<i>Fat - 3 mm</i>
<i>Air - 1 mm</i>	<i>Fat - 1.5 mm</i>	<i>Air - 1 mm</i>	<i>Air - 1 mm</i>
<i>Receiving coil</i>	<i>Muscle - 12 mm</i>	<i>Fat - 2 mm</i>	<i>Receiving coil</i>
<i>Air - 1 mm</i>	<i>Ulna - 5 mm</i>	<i>Muscle - 17 mm</i>	<i>Air - 1 mm</i>
<i>Fat - 4.5 mm</i>	<i>Muscle - 2 mm</i>	<i>Colon - 40 mm</i>	<i>Fat - 3 mm</i>
<i>Muscle - 36 mm</i>	<i>Radius - 3 mm</i>	<i>Fat - 40 mm</i>	<i>Muscle - 45 mm</i>
<i>Humerus - 18 mm</i>	<i>Muscle - 12 mm</i>	<i>Intestine - 33 mm</i>	<i>Femur - 14 mm</i>
<i>Muscle - 48 mm</i>	<i>Blood - 5 mm</i>	<i>Blood - 17 mm</i>	<i>Muscle - 45 mm</i>
<i>Fat - 9 mm</i>	<i>Muscle - 4 mm</i>	<i>Spine - 56 mm</i>	<i>Fat - 6 mm</i>
<i>Skin - 1.5 mm</i>	<i>Blood - 4 mm</i>	<i>Muscle - 83 mm</i>	<i>Skin - 2 mm</i>
	<i>Muscle - 8 mm</i>	<i>Fat - 10 mm</i>	
	<i>Fat - 3 mm</i>	<i>Skin - 2 mm</i>	
	<i>Skin - 2 mm</i>		

been considered as 2-port networks and the S-parameters obtained with the simulation tool have been used to calculate the link efficiency as described in the Appendix.

Effects of the Coil Geometry on the Link Efficiency

The size of the inductors greatly affects the link efficiency. Smaller inductors involve higher working frequency but lower link efficiency. The effects of the coil geometry on the link efficiency and the working frequency are reported here for receiving inductors compatible with the size of the i-IronIC sensor.

We have performed a set of simulations with the receiving coil implanted in the arm (Table 3.1). The results are shown in Fig. 3.2. As expected, a reduced size of the coils involves a higher optimal frequency, together with a lower link efficiency. For the tested geometries, the optimal frequency is always located over 100 MHz, at least one order of magnitude higher than the frequencies commonly used. With the largest geometry the link efficiency is about 30%.

Implantation Sites

The implantation sites depend on several factors, such as the substances to detect or the tissues to check. For instance, the monitoring of glucose in elderly patients or diabetics can be performed in the interstitial regions of the abdomen, while the monitoring of lactate in

Chapter 3. Inductive Link for mm-sized Implants: Frequency and Geometry Optimization

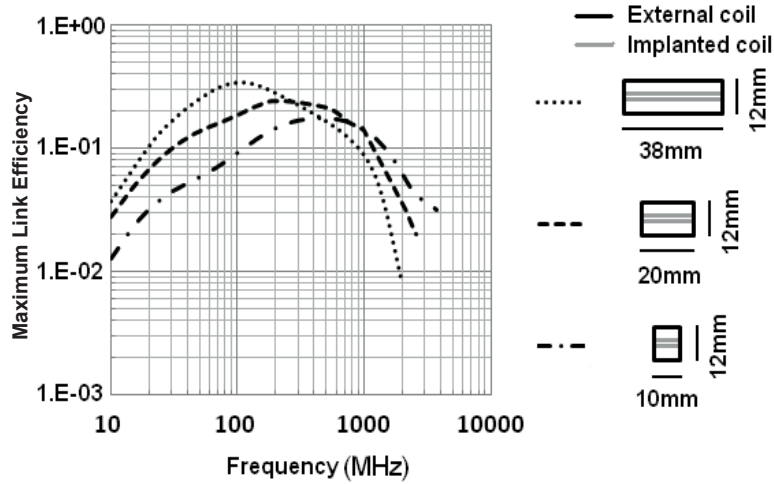


Figure 3.2: The smaller size of the coils involves a higher optimal frequency, along with a lower link efficiency. Simulations are performed in the arm. Reprinted from [37].

sportsmen must be performed in the interstitial regions of the limbs under stress. Thus, we have tested different implantation zones, reported in Table 3.1, keeping unchanged the geometries of the coils. The results are shown in Fig. 3.3. The optimal frequency does not change by implanting the receiving coil in different zones. Moreover, the link efficiency depends on the implantation depth and decreases with deeper implanted coils. The differences of tissues in the implantation zones do not affect the link efficiency.

Lateral Misalignment

Misalignments between the transmitting and the receiving coil can occur due to erroneous placement of the external inductor or difficulties in locating the exact implantation zone. Thus, we have simulated lateral misalignments between the coils for a given geometry (Fig. 3.4). The simulations are performed with the receiving coil implanted in the arm. Lateral misalignments strongly affect the link efficiency, while they do not shift the optimal frequency. Furthermore, lateral misalignments over 20 mm seriously compromise the efficiency of the inductive link.

Multiple-turn External Coils and Frequency Shift

Finally, we have performed a set of simulations using external coils with multiple turns. The results are shown in Fig. 3.5. In two simulations (14 turns and 29 turns), the trace width of the external coil is 0.2 mm, while the trace spacing is 0.2 mm. In the third simulation (30 turns) the trace width is 0.254 mm, while the trace spacing is 0.14 mm. The optimal frequency is always lower than in the case where a single-turn external coil is used. In the case of a 30-turn external coil the optimal frequency is about 10 MHz, at least one order of magnitude lower than the optimal frequencies obtained in the previous simulations. These results show the

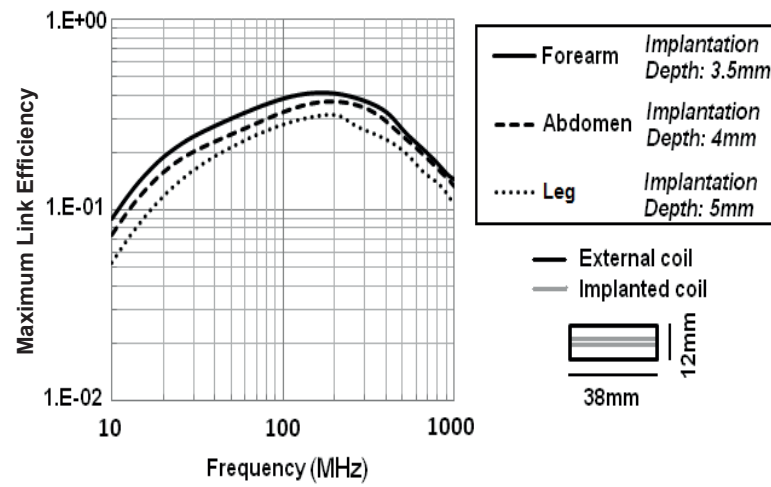


Figure 3.3: Different implantation sites do not affect the optimum frequency. The differences among the three curves are mostly due to the different implantation depths. Reprinted from [37].

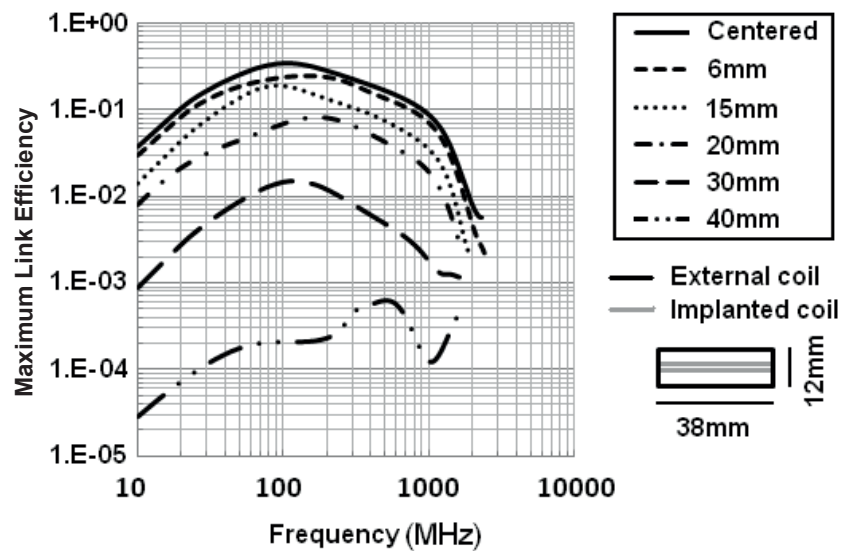


Figure 3.4: Lateral misalignments between the coils have been simulated for a given geometry. The misalignments do not affect the optimal frequency. Reprinted from [37].

Chapter 3. Inductive Link for mm-sized Implants: Frequency and Geometry Optimization

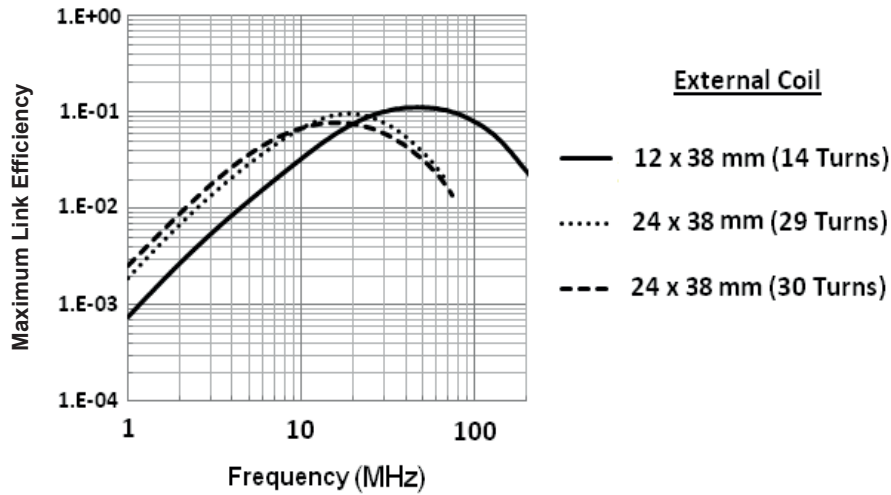


Figure 3.5: Maximum link efficiency obtained with multiple-turn external coils. The number of turns and the geometry of the external coils affect the optimal frequency. Reprinted from [37].

possibility to operate in the low megahertz range, where tissue absorption is minimum, while dealing with mm-sized receiving inductors and multi-turn, cm-sized transmitting inductors. This achievement has been obtained by increasing the size and the number of turns of the external inductor, as compared to the previous simulations.

This last set of simulations suggests the use of a multiple-turn external inductor, in order to work in the low megahertz range where tissue absorption is minimum. In the next section, a mathematical model is proposed to obtain the electrical parameters of multi-turn spiral inductors starting from their geometry. Several multi-turn external inductors are modeled using that method.

3.2 Inductor Modeling

The capability to model multi-turn spiral inductors in terms of lumped elements, starting from their geometry, is extremely important while designing inductive links. Instead of running long *Finite Element Method* (FEM) simulations for a large number of geometries, a mathematical model can be used to define a subset of possible geometries to be subsequently tested with more powerful analysis tools. In this section we propose a lumped RLC description of printed spiral inductors (Fig. 3.6). Several models have been presented in the literature to define the value of these elements [108–112]. However, most of these models describe inductors integrated on silicon, thus limiting their applicability to printed inductors. In this section, we present a model dedicated to printed spiral inductors, obtained from different analyses reported in the literature, most of which have been recently reviewed in [113]. The model has been implemented in Matlab and the results of the simulations have been compared with the impedance measurements.

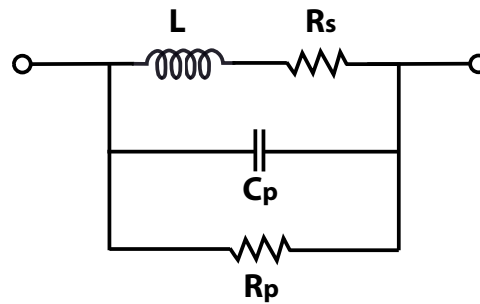


Figure 3.6: Lumped RLC model of a printed spiral inductor. Second order effects are not considered. Reprinted from [38].

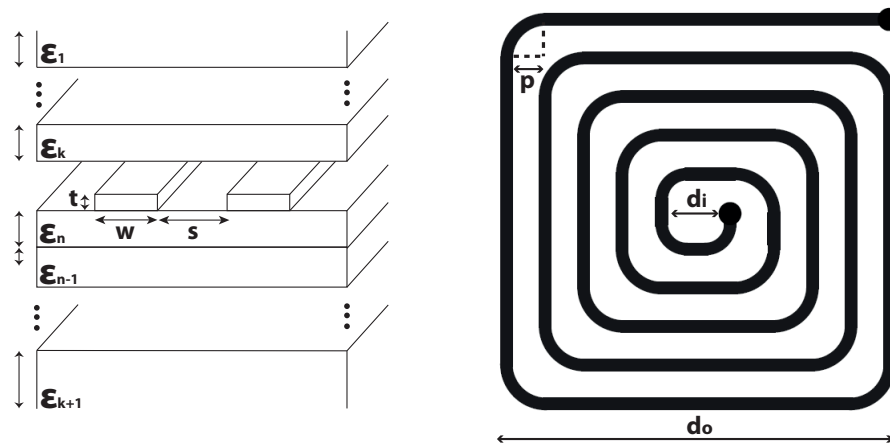


Figure 3.7: Geometrical and physical parameters of a printed inductor and the surrounding substrates. Reprinted from [38].

The model aims to determine the values of the RLC lumped elements reported in Fig. 3.6, describing the behavior of a printed inductor. The model receives as input the geometrical and physical parameters of the inductors and the surrounding substrates (Fig. 3.7). In this analysis we have considered only square-shaped inductors.

Inductance L

Different equations have been proposed in the literature to approximate the value of the inductance L . We have used the expression proposed by [114] for square-shaped coil:

$$L = \frac{1.27 \cdot \mu n^2 d_{avg}}{2} \left[\ln \left(\frac{2.07}{\varphi} \right) + 0.18\varphi + 0.13\varphi^2 \right], \quad (3.2)$$

Chapter 3. Inductive Link for mm-sized Implants: Frequency and Geometry Optimization

where μ is the magnetic permeability of the metal traces, n is the number of turns, $d_{avg} = (d_o + d_i)/2$, and $\varphi = (d_o - d_i)/(d_o + d_i)$. The parameter φ , called *fill factor*, tends to zero if the turns are concentrated close to the external perimeter, while it tends to one if the turns fill all the inductor area. As underlined by [113], the error in (3.2) is higher than 8% for $s/w > 3$ and the accuracy degrades with $\varphi \leq 0.1$ or $n \leq 2$.

Capacitance C_p

The parallel capacitance C_p has an important role among the different elements of the model. Indeed, this component determines the self-resonance frequency of the inductor.

To calculate the parallel capacitance C_p we first define the parallel capacitance per unit length C_a . According to the model presented by [111, 113], the value of C_a can be expressed as

$$C_a = C_0 + \sum_{i=1}^n C_{0i} = \varepsilon_{\text{eff}} C_0, \quad (3.3)$$

where C_0 is the capacitance per unit length between adjacent traces and C_{0i} is the capacitance between the traces and the i^{th} substrate.

According to [111], the value of C_0 is defined as follows:

$$\begin{cases} C_0 = \varepsilon_0 \frac{K(k'_0)}{K(k_0)}, \\ k_0 = \frac{s}{s + 2w}, \\ k'_0 = \sqrt{1 - k_0^2}, \end{cases} \quad (3.4)$$

where $K(\cdot)$ is the complete elliptic integral of the first kind and ε_0 is the electrical permittivity of the vacuum ($\varepsilon_0 \approx 8.854 \times 10^{-12}$ F/m).

The value of ε_{eff} is calculated as

$$\varepsilon_{\text{eff}} = 1 + \frac{1}{2} \sum_{i=2}^k (\varepsilon_{r_i} - \varepsilon_{r_{i-1}}) \frac{K(k_0)K(k'_i)}{K(k'_0)K(k_i)} + \frac{1}{2} \sum_{i=k+2}^n (\varepsilon_{r_i} - \varepsilon_{r_{i-1}}) \frac{K(k_0)K(k'_i)}{K(k'_0)K(k_i)}, \quad (3.5)$$

where the term ε_{r_i} is the relative permittivity of the i^{th} substrate and the terms k_i and k'_i are

defined as

$$\begin{cases} k_i = \frac{\tanh\left(\frac{\pi s}{4t_i}\right)}{\tanh\left(\frac{\pi(s+2w)}{4t_i}\right)}, \\ k'_i = \sqrt{1 - k_i^2}, \end{cases} \quad (3.6)$$

where t_i is the thickness of the i^{th} substrate.

According to [111, 113], the effect of trace thickness on the capacitances is considered by reducing the spacing s in (3.4b) and (3.6a) of a factor 2Δ , where Δ is defined as

$$\Delta = \frac{t}{2\pi\epsilon_e} \left[1 + \ln\left(\frac{8\pi w}{t}\right) \right], \quad (3.7)$$

being ϵ_e the relative permittivity of the material between the traces.

Finally, by considering the total length of the inductor as

$$l = 4nd_o - 4n^2w - (2n-1)^2s + \left[\left(\frac{\pi}{2} - 2\right)(4n-1)p\right], \quad (3.8)$$

the parallel capacitance C_p can be written as

$$C_p = \frac{C_a}{n} \cdot l. \quad (3.9)$$

Different from [113], C_a in (3.9) has been divided by a factor n to consider the voltage drop across the inductor turns. This solution has been suggested by [115].

Resistance R_s

The series resistance R_s of the model includes two elements. The first element is independent of the frequency and is described by the Ohm's law. The second element is frequency dependent and includes the skin effect.

Chapter 3. Inductive Link for mm-sized Implants: Frequency and Geometry Optimization

An estimation of the series resistance, suggested by [115], is

$$R_s = \rho l \left(\frac{1}{wt} + \frac{1}{2\delta(t+w)} \right), \quad (3.10)$$

where ρ is the resistivity of the metal traces. The term δ represents the skin depth and can be expressed as

$$\delta = \sqrt{\frac{2\rho}{\omega\mu}}, \quad (3.11)$$

where ω is the angular frequency and μ is the magnetic permeability of the metal traces.

Resistance R_p

Parallel resistance R_p is due to the finite resistance of the insulating layer where the inductor is placed. According to [115], parallel resistance has been modeled as

$$R_p = \frac{\rho_k t_k}{wl}, \quad (3.12)$$

where ρ_k and t_k are the resistivity and the thickness of the k^{th} layer where the inductor is placed.

Model Validation

The mathematical model just introduced has been implemented in Matlab and the results have been compared with the measurements. The geometrical parameters of the test inductors are listed in Table 3.2. For these geometries, the results obtained from simulations and measurements are listed in Table 3.3. The impedance of the test inductors has been measured by means of a network analyzer starting from the scattering parameters. In the simulations, the impedance Z is calculated using the lumped parameters presented in Fig. 3.6:

$$Z = \frac{R_s R_p + j\omega L R_p}{(R_s + R_p - \omega^2 L R_p C_p) + j\omega(L + R_p R_s C_p)}. \quad (3.13)$$

Table 3.2: Geometrical parameters of the test inductors. Table from [38].

Geometrical Parameters	TxA	TxB	TxC
d_o (mm)	38	37.8	24.3
d_i (mm)	5.4	7.8	1.37
s (mm)	2.5	1	0.146
w (mm)	1.2	1	0.254
p (mm)	3.8	2	0
n	5	8	29
t (μm)	35	35	35
ϵ_1 (Air)	1	1	1
t_1 (mm)	Open	Open	Open
ϵ_2 (Air)	1	1	1
t_2 (mm)	Open	Open	Open
ϵ_3 (FR4)	4.4	4.4	4.4
t_3 (mm)	1.2	1.2	0.8

Table 3.3: Electrical parameters of the test inductors. Table from [38].

Electrical Parameters	TxA		TxB		TxC	
	Measurement	Model	Measurement	Model	Measurement	Model
Self-resonance frequency (MHz)	112.2	160.5	70.4	75.9	32.6	32.5
L (μH)	0.588	0.565	1.53	1.52	9.44	9.50
C _p (pF)	3.42	1.74	3.34	2.89	2.52	2.52
$\Re\{Z\}$ @ 1 MHz (Ω)	0.28	0.22	0.56	0.45	3.61	3.68
$\Im\{Z\}$ @ 1 MHz (Ω)	3.76	3.58	9.76	9.64	60.1	60.4

Chapter 3. Inductive Link for mm-sized Implants: Frequency and Geometry Optimization

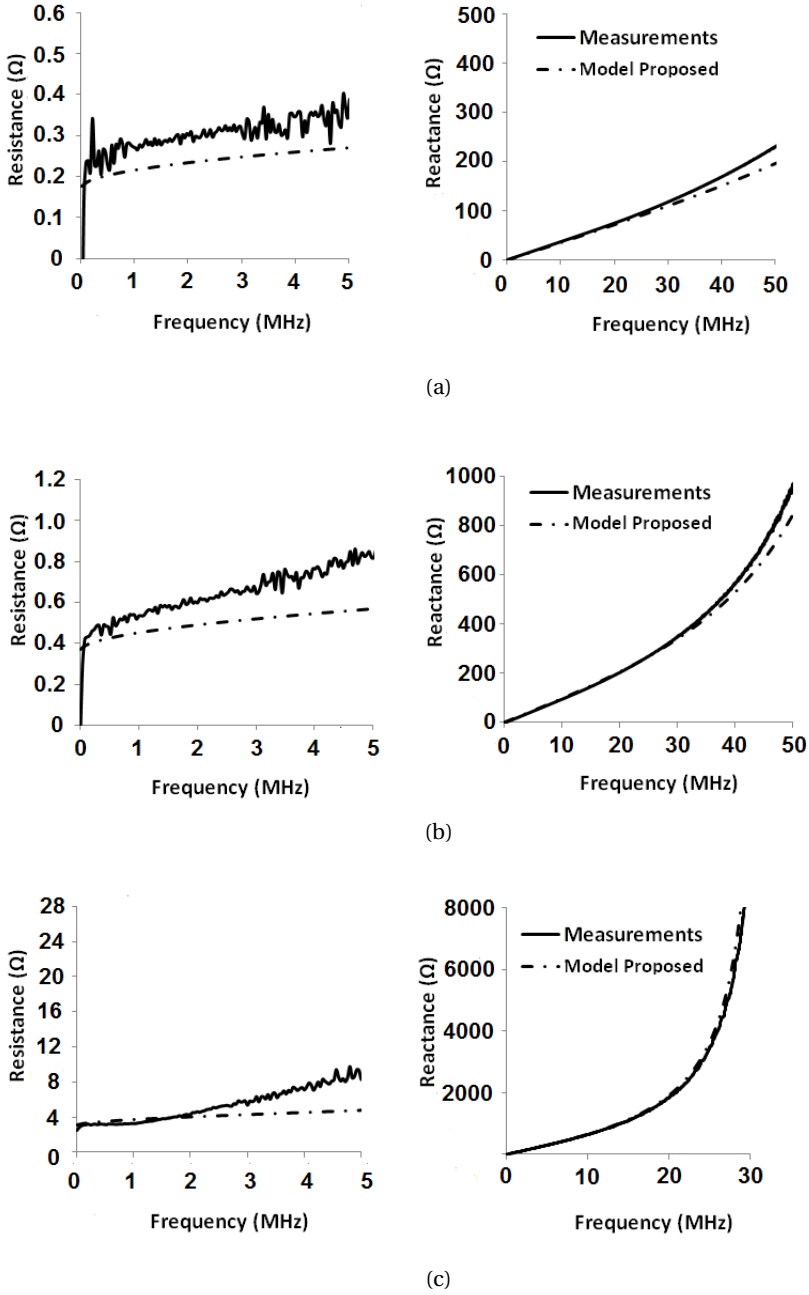


Figure 3.8: Impedance of the inductors described in Table 3.2. TxA (a), TxB (b), TxC (c). Reprinted from [38].

In Fig. 3.8 are shown the real and the imaginary part of the inductor impedance. The simulations are compared with the measurement results. The self-resonance frequencies returned by the simulations are slightly different from those obtained with the measurements. This shift is due to the inaccuracy of the model while estimating the parallel capacitance C_p . Indeed, the measured value of C_p is noticeably influenced by several factors, such as the surrounding environment and the parasitic capacitances. Thus, it is difficult to model this element with high precision.

Nevertheless, the value of C_p provided by the model is sufficient to have a rough valuation of the self-resonance frequency. Then, if we assume to work at least one order of magnitude below the self-resonance frequency, the model can be simplified by neglecting the presence of C_p . Indeed, at these low frequencies the parallel capacitance does not significantly affect the impedance Z presented in (3.13).

As shown in Table 3.3, at the operating frequency of 1 MHz the maximum error on the impedance is 21.4% on the real part and 4.8% on the imaginary part for spiral TxA. For more dense geometries, such as TxC, the error of the model at 1 MHz is reduced to 1.9% on the real part and 0.5% on the imaginary part.

3.3 Chapter Contribution and Summary

In this chapter we have presented the research work dedicated to the design and optimization of an inductive link with mm-sized receiving inductors. The effects of several factors (such as coil geometry, implantation depth, and misalignments) on the link efficiency have been analyzed by means of simulations. Smaller inductors involve higher optimal frequencies, as well as a lower efficiency. Lateral misalignments do not affect the optimal frequency but seriously compromise the link efficiency. Finally, no particular changes have been noticed while simulating different implantation zones.

Particular emphasis has been given to the possibility to operate in the low megahertz range, where tissue absorption is minimum, while using a multi-turn, cm-sized external inductor. This result has been used in the design and manufacturing of the receiving inductors presented in the next chapter.

Finally, a model has been presented to calculate the electrical proprieties of multi-turn external inductors starting from their geometry. This model has been realized to aid the designer while optimizing the link efficiency. The model is particularly suitable for dense inductors working at least one order of magnitude below the self-resonance frequency.

4 Design and Fabrication of Miniaturized Receiving Inductors

In this chapter we describe the design and realization of mm-sized receiving inductors for implantable devices. Two different approaches are considered: multi-layer printed spiral inductors and microfabricated spiral inductors.

Multi-layer printed spiral inductors consist of several printed inductors, stacked and electrically connected to obtain a multi-layer structure. This solution noticeably increases the link efficiency while compared with single-layer structures having the same area. Moreover, inductor area can be further reduced while preserving the link efficiency if the number of layers is increased.

Microfabricated spiral inductors have been explored to further reduce the size of the implantable biosensor. The main challenge of this approach is to preserve the inductor quality factor while dealing with single-layer, mm-sized structures. The fabrication process flow is described in detail in the remainder of the chapter, together with the electrical characterization of the microfabricated inductors.

4.1 Multi-layer Spiral Inductors

In this section we explore the use of multi-layer printed spiral inductors as receiving elements of an inductive link. Thanks to this approach, the size of the receiver inductors can be noticeably reduced with respect to the classical “pancake” inductors or the single-layer spiral inductors, such as those used in [25–27, 31–33]. Moreover, the decrease in size does not result in a lower efficiency of the system in terms of power transmission. Finally, the small size of multi-layer spiral inductors supports their implantation in the subcutaneous zones by means of an injection.

The proposed approach is initially compared to different solutions presented in literature, such as litz-wire coils, on-chip inductors, and MEMS inductors. Then, the advantages of multi-layer structures, in terms of link efficiency and voltage gain, are investigated and compared with a single-layer approach.

4.1.1 Standard Design Techniques for Inductive Links

The design of the inductors composing the link greatly affects both the performance of the system and the comfort of the patient. Indeed, the small size of the receiving inductor noticeably simplifies the implantation process and reduces the discomfort of the patient. Litz-wire coils, integrated CMOS inductors, MEMS inductors, and printed spiral coils are the most common solutions for the receiving inductors.

Litz wires consist of many thin strands, individually insulated and twisted or woven together, according to a predefined pattern. Then, those wires can be used to obtain the receiving coil (litz-wire coils). Litz-wire inductors have already been used for the remote powering of implantable systems [27, 116]. This approach reduces the resistive losses due to the skin and proximity effects [117]. However, the advantages of using litz wires, rather than solid wires, decrease for frequencies higher than hundreds of kilohertz. By increasing the frequency over that range, a threshold is reached where local proximity losses increase and litz wires become more lossy than solid wires. This threshold has been estimated close to 1 MHz [118]. Usually, inductive links for the remote powering of implantable devices operate in a slightly higher frequency range, between 1 MHz and 13.56 MHz, with two dedicated frequencies at 6.78 MHz and 13.56 MHz [25–28, 30–33]. Thus, frequency limitations are a drawback of using litz-wire coils for the remote powering of implantable sensors.

Frequency issues can be mitigated by increasing the number of strands, while reducing the diameter. However, physical limits exist on strand reduction. Moreover, a smaller diameter of the strands results in a decreased packing factor, defined as the ratio between the copper area and the area of the bundle [118].

Another implementation is the integration of spiral inductors on-chip with the logic circuitry to be powered by the receiver. This approach considerably reduces the area of the system. However, by using a standard CMOS fabrication process, passive inductors usually have small inductance (typically in the range of nanohenries [119]) and high resistance, leading to quality factors with maximum value at high frequency (from hundreds megahertz up to few gigahertz) and usually lower than ten [120, 121]. For these reasons, this approach is not suitable for power links operating in the low megahertz range.

These limitations can be surmounted by using different microfabrication techniques. Several solutions have been presented in literature employing MEMS inductors. By using thick-metal surface micromachining technology, ref. [51] significantly decreased the inductor resistance, as compared to standard CMOS inductors. This decrease enables higher quality factors. However, since the inductance values remain in the order of few nanohenries, those quality factors still have their maximum in the gigahertz range.

Electroplating techniques can be used to obtain microfabricated inductors with lower resistance, when compared to thin film inductors. An inlaid electroplating procedure is used in [53] to realize microcoils on silicon substrates. The fabricated inductor has an area of

$14 \times 14 \text{ mm}^2$ and a quality factor of about 34 at 4 MHz. Similar performance is obtained by using electroplated gold on an insulating substrate [122]. The fabricated inductor has an area of $15 \times 15 \text{ mm}^2$ and a quality factor of 29 at 13.56 MHz.

Finally, another option to design the receiving inductor is to use a standard *Printed Circuit Board* (PCB) process. This method enables the realization of the receiving coil on rigid or flexible substrates. Flexible substrates can considerably facilitate the implantation process. Furthermore, by using printed inductors several layers can be stacked to obtain multi-layer structures. The multi-layer approach enables area reduction, while preserving the performance of the link. Differently from what happens with microfabrication, no technological limitations exist on the number of layers that can be stacked.

The multi-layer approach has already been presented in literature [47–49]. Ref. [48] has proposed a $10 \times 10 \text{ mm}^2$, 4-layer, $2.5 \mu\text{H}$ receiving inductor having a quality factor of about 90 at 13.56 MHz. These results have been simulated. The effects on the inductance and the quality factor of different parameters (i.e., number of layers, spacing between adjacent traces, and trace width) are reported. A set of equations is proposed to calculate the electrical parameters of multi-layer structures starting from their physical characteristics [49]. A $9 \times 9 \text{ mm}^2$, 2-layer, $3.8 \mu\text{H}$ receiving inductor with a quality factor of 42 at 10 MHz has been developed by using these analytic expressions [49].

Several key points make this technique particularly suitable for the remote powering of implantable systems. The implantation process can be eased by the flexibility of the substrate and the possibility to partially reduce the inductor area, while preserving the link performance. Moreover, a relatively high quality factor can be obtained with a simple and inexpensive process.

This section contributes to the existing literature by investigating the use of multi-layer inductors for the remote powering of implantable systems. Indeed, the fabrication and measurement of multi-layer structures and the effects of their geometry on the link efficiency and voltage gain are a novel contribution to the literature. Furthermore, an asymmetrical shape of the receiving inductor is investigated. Due to a rectangular shape, having the form factor of a needle, the implantation process can be facilitated. This reduces the discomfort of the patient. Multi-layer rectangular structures are realized on a flexible substrate and measured, in order to compare their performance with the simulations reported in literature.

4.1.2 Design and Test of Multi-layer Spiral Inductors

We have designed and measured different geometries in order to determine the optimal tradeoff among the link efficiency, the voltage gain, and the size of the receiving inductors. The curves presented here are obtained by measuring the electrical parameters of the coils. By substituting these parameters in (2.22) and (2.23), the link efficiency and the voltage gain are determined. The electrical parameters of the coils are measured by means of a network analyzer (Rohde & Schwarz - ZVL).

Initially, receiving inductors with different size have been tested by using the same external inductor (Fig. 4.1). The results of these measurements show that the link efficiency does not increase over 10 MHz. This behavior is in agreement with the simulations in Fig. 3.5. Moreover, by increasing the size and the number of turns of the receiving inductor, both the link efficiency and the voltage gain increase. Indeed, a larger area and more turns for the receiving inductor lead to a higher mutual inductance M between the coils and the link efficiency (2.22) increases with M . Furthermore, if expression (2.20) is satisfied, also the voltage gain (2.23) increases with M .

Different widths of the traces have been measured for the external inductor, while maintaining the area fixed (Fig. 4.2). A lower number of turns with larger width results in a lower resistance R_1 of the external inductor and the maximum link efficiency (2.22) is a decreasing function of R_1 . However, a lower number of turns also reduces the mutual inductance M and the maximum link efficiency (2.22) is an increasing function of M . Consequently, to test which behavior is predominant between the decrease in R_1 and the decrease in M , different widths are tested for the traces of the external inductor, while keeping constant the inductor area. In the inductors with wider traces, the decrease in M outweighs the decrease in R_1 , thereby lowering the maximum link efficiency. Instead, the voltage gain strongly increases where the number of turns of the external inductor is reduced. Indeed, it can be shown that the voltage gain (2.23) is inversely proportional to the number of turns of the external coil under a constant-Q assumption [94].

This assumption considers the quality factor of a coil independent of the number of turns, for a given shape and size of the coil. This assumption can be used while optimizing the link efficiency, since the maximum link efficiency varies slowly with the quality factors of the inductors composing the link. This assumption has been used in [94, 124] to optimize the link performance.

The major constraint related to the use of subcutaneous implantable devices is the size. Indeed, to reduce the discomfort of the patient and facilitate the implantation process, implantable devices should be as small as possible. This requirement is in conflict with the results shown in Fig. 4.1. Indeed, a smaller internal coil results in a lower link efficiency and voltage gain. To mitigate this issue, a multi-layer approach is experimentally investigated. Multi-layer inductors, thanks to their small area, are particularly suitable for this type of applications.

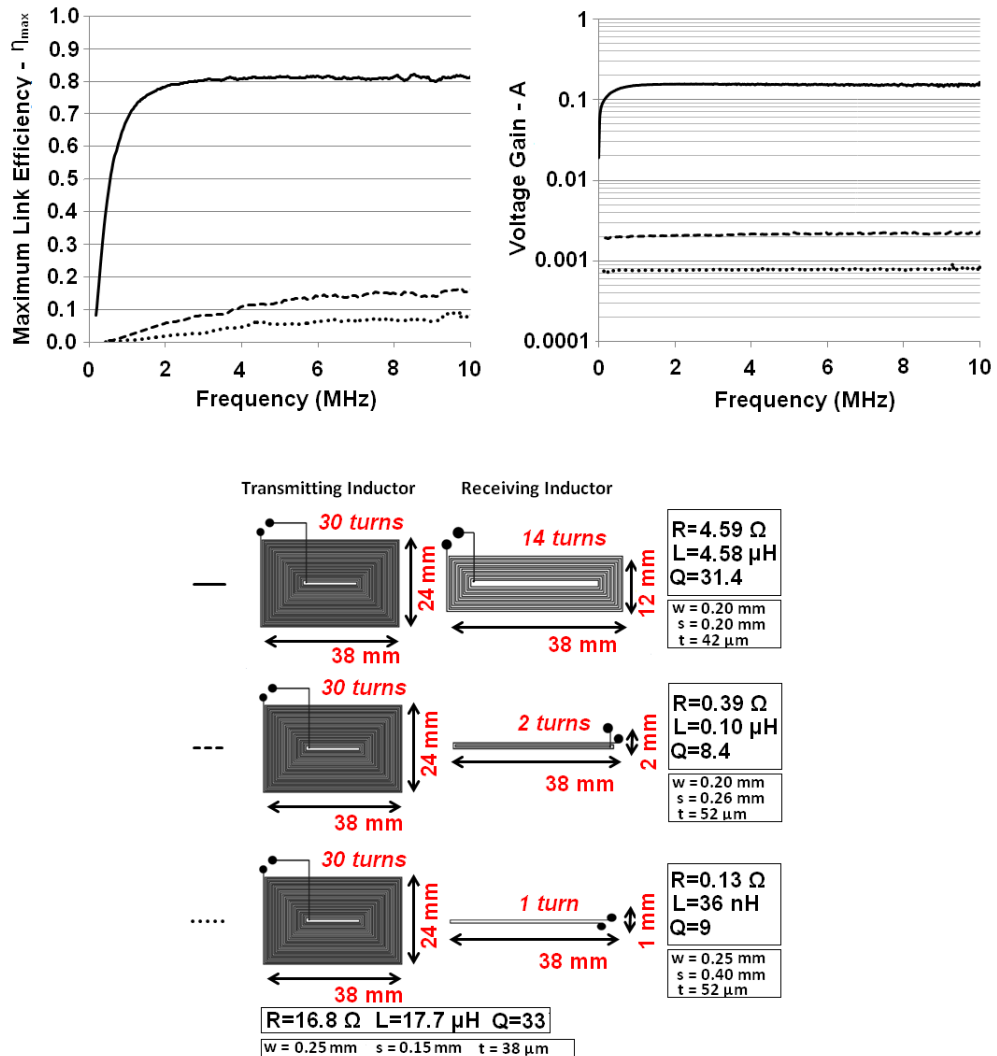


Figure 4.1: Link efficiency and voltage gain decrease when smaller receiving inductors are used. The distance between the coils is 5 mm. The inductance and resistance of each coil are measured at 5 MHz. Notations w , s , and t indicate the trace width, the spacing between adjacent turns, and the trace thickness, respectively. Reprinted from [123].

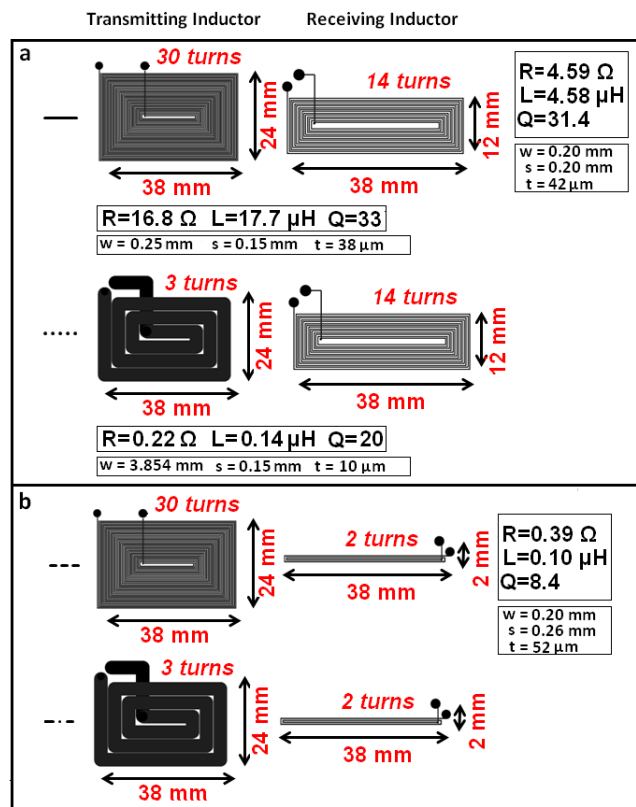
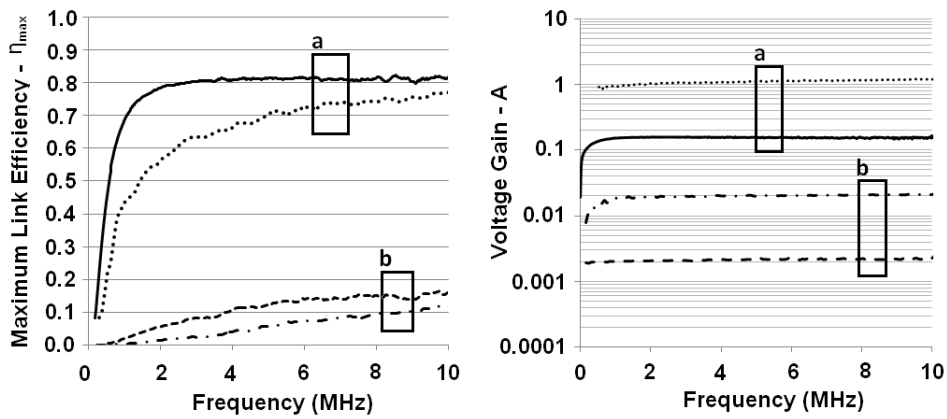


Figure 4.2: By reducing the number of turns of the external inductor and increasing their width, the link efficiency slightly decreases while the voltage gain noticeably increases. This behavior is not affected by the larger (group a) or smaller (group b) size of the internal inductor. The distance between the coils is 5 mm. The inductance and resistance of each coil are measured at 5 MHz. The notation of the parameters is the same as in Fig. 4.1. Reprinted from [123].

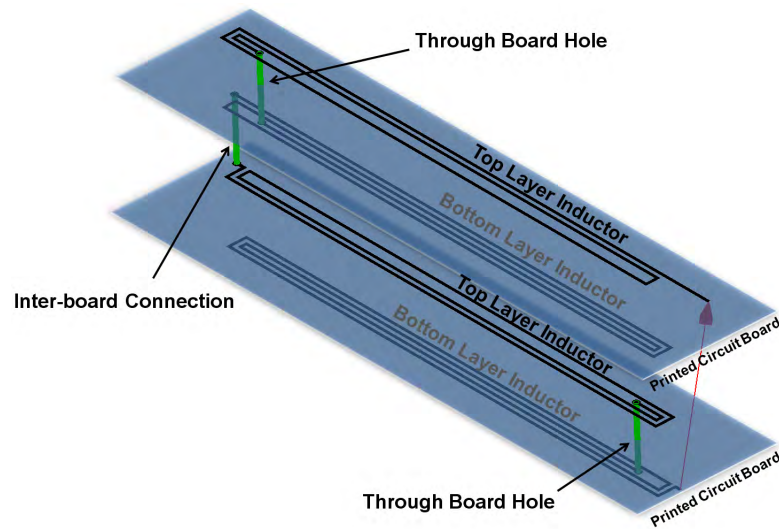


Figure 4.3: Layout of a multi-layer spiral inductor on PCB. Reprinted from [123].

The design of a multi-layer inductor is shown in Fig. 4.3. In a multi-layer coil, the same spiral inductor is replicated on the two layers of several PCB; then, the different boards are stacked and the inductors are electrically connected. Thus, a single multi-layer inductor is obtained. A multi-layer inductor has the same area as the equivalent single-layer inductor, but includes many more turns and, hence, a higher coupling with the external inductor. Attention must be paid to the direction of the current among the different layers. Indeed, the layout must be designed to have the current flowing in the same direction in all the layers. Thus, the contribution of each layer to the total magnetic field will have the same sign.

We have realized and tested several multi-layer inductors to investigate their performance and compare them with a single-layer approach (Fig. 4.4). In Fig. 4.5 the same geometries depicted in Fig. 4.1 are shown, with the addition of an 8-layer, 14-turn inductor. This multi-layer inductor has higher link efficiency and voltage gain as compared with the single-layer inductor having the same area. The link efficiency is 35% higher, shifting from 0.17 to 0.23 at 10 MHz. The voltage gain is almost one order of magnitude higher.

By using multi-layer inductors it is possible to partially compensate a reduction of area by properly increasing the number of layers. This possibility is shown in Fig. 4.5. The 12-layer, 21-turn inductor having an area of 30 mm^2 and a total thickness of $816 \text{ }\mu\text{m}$ exhibits almost the same performance of the 8-layer, 14-turn inductor, with an area of 76 mm^2 and a total thickness of $544 \text{ }\mu\text{m}$. Consequently, the same performance is obtained with an area reduction of about 60%.

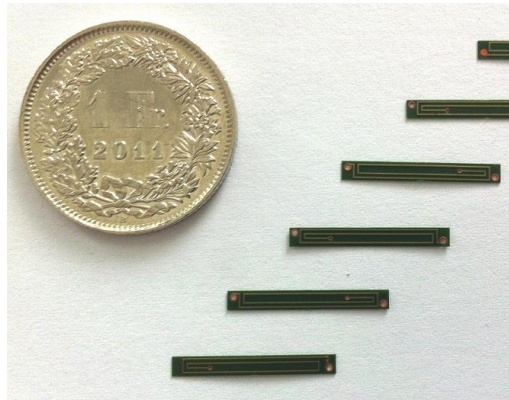


Figure 4.4: Multi-layer spiral inductors are obtained by stacking and connecting single-layer inductors realized on a flexible substrate. Reprinted from [123].

4.1.3 Performance Evaluation

In order to measure the performance of the system where multi-layer spiral inductors are used, the following setup is used. The transmitting inductor is driven by using a class-E power amplifier (described in Chapter 5). The power collected by the receiving inductor is measured by means of a spectrum analyzer (Rohde & Schwarz - ZVL). The receiving inductor is not directly connected to the spectrum analyzer. Instead, a capacitive matching network is used to match the input impedance of the instrument ($50\ \Omega$) to the impedance of the receiving inductor. A mechanical setup is used to adjust the distance between the transmitting and receiving inductors, while assuring a planar alignment. The distance between the inductors lies within the range from 6 mm to 70 mm.

To investigate the performance of the system, we have performed a first set of measurements in ambient air. The receiving inductor is the 12-layer, 21-turn, $15 \times 2\ \text{mm}^2$ coil shown in Fig. 4.5. The amplifier can transmit about 15 mW over a distance of 6 mm. The link efficiency, as calculated from (2.22) by using the measured values of the inductors, is about 13%. While transmitting 15 mW at 6 mm, the amplifier consumes about 340 mW. Thus, the overall efficiency of the system is about 4.4%. The transferred power quickly decreases when the distance between the inductors increases. In Fig. 4.6, the curve denoted as “model” is obtained by using the measured values of the inductors in (2.22); the curve named “measurement” is obtained by reporting the power effectively delivered to the load. Measurements present good agreement with eq. (2.22) reported in Chapter 2. Both the curves decrease as $1/x^{2.5}$.

Finally, a second set of measurements is performed with beef sirloin between the inductors (Fig. 4.7). The thickness of the sirloin is 17 mm. In this case, the transferred power is about 1.17 mW. This result is similar to that obtained in ambient air by using the same distance between the inductors (Fig. 4.6).

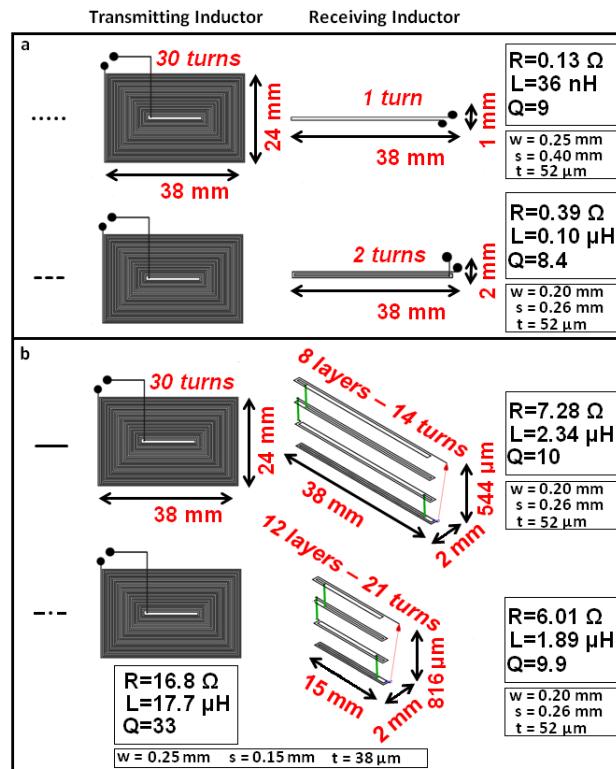
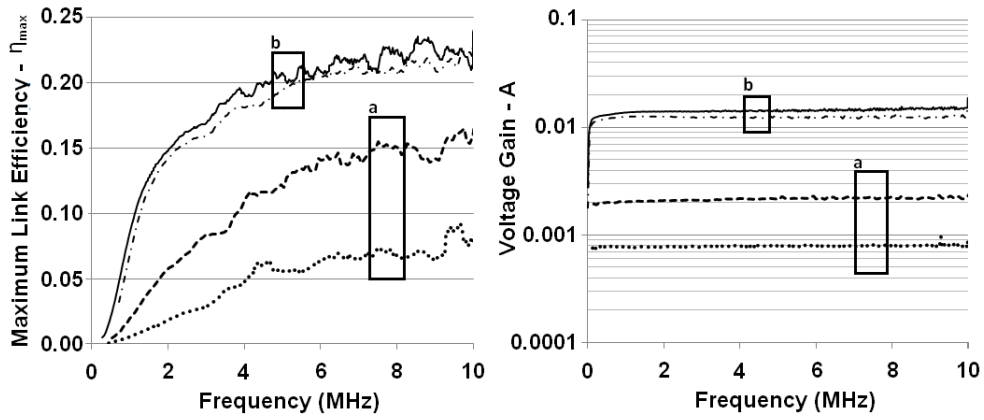


Figure 4.5: Multi-layer spiral inductors (group b) enable a higher link efficiency and voltage gain if compared with single-layer inductors having the same area (group a). Furthermore, the reduction of area in multi-layer inductors can be partially compensated by increasing the number of layers (group b). The distance between the coils is 5 mm. The inductance and resistance of each coil are measured at 5 MHz. The notation of the parameters is the same as in Fig. 4.1. Reprinted from [123].

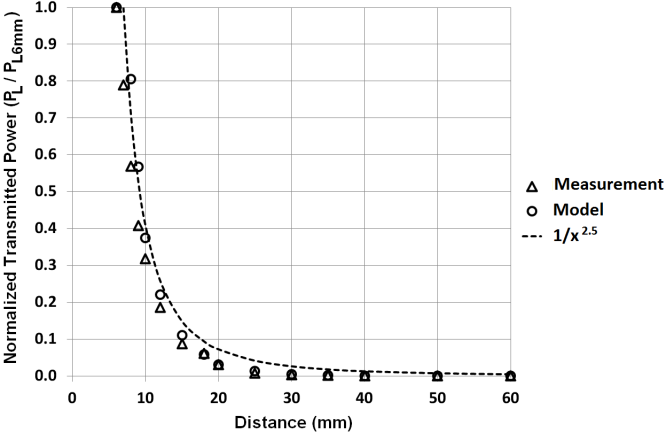


Figure 4.6: Both the model based on (2.22) and the measurements confirm a strong dependence of the transferred power on distance. Reprinted from [123].

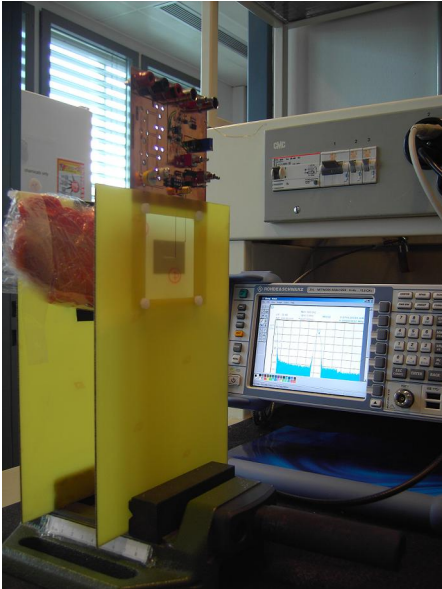


Figure 4.7: Measurements are performed using beef sirloin between the inductors. Reprinted from [123].

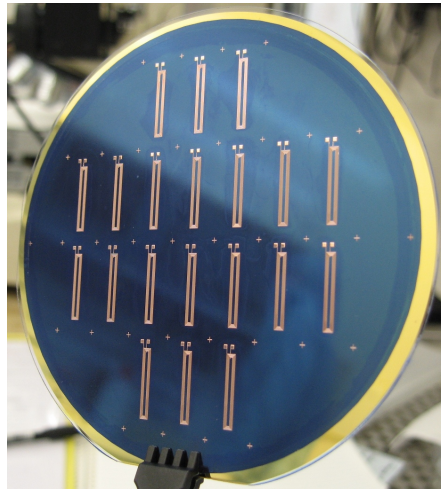


Figure 4.8: Microfabricated spiral inductors during the fabrication process (step (c) of Fig. 4.12). Reprinted from [125].

4.2 Microfabricated Spiral Inductors

Microfabrication can sensibly decrease the size of implantable coils, thus reducing the discomfort of the patient. Indeed, inductors can be fabricated directly on the substrate hosting the system to be powered (Fig. 1.1). The main challenge of this approach is to preserve the quality factor of the inductors while dealing with small structures. To that aim, trace thickness should be in the order of tenths of micrometers to reduce the resistance and increase the quality factor.

Several solutions have been proposed in the literature for the microfabrication of spiral inductors. Thick electroplated inductors on SU8 flexible substrate [50] and silicon [51, 52] have been proposed. In these works, the coil thickness does not exceed $24\ \mu\text{m}$. Ref. [53] has shown an inlaid process to fabricate electroplated inductors on a silicon substrate with a trace thickness of $60\ \mu\text{m}$. However, the proposed inlaid technique cannot be directly used on substrates other than silicon .

In this section, we propose a process to microfabricate electroplated spiral inductors with high trace thickness (starting from $60\ \mu\text{m}$) on different substrates, such as silicon or pyrex (Fig. 4.8). Microfabrication of the receiving inductor directly on the silicon substrate hosting the sensor can noticeably decrease the total volume of the system, as compared with the case where multi-layer printed inductors are used [123]. Finally, the realization of high-thickness structures with a single photoresist deposition is a practical contribution to the existing literature.

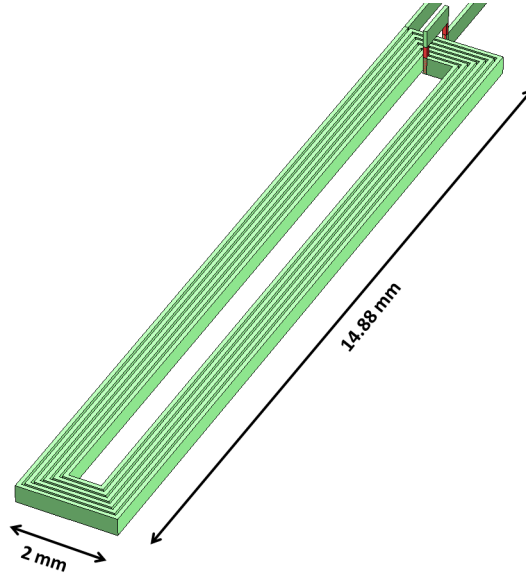


Figure 4.9: The inductors, having a size of $14.88 \times 2 \text{ mm}^2$, are simulated onto a substrate of $525 \text{ }\mu\text{m}$ silicon + $1 \text{ }\mu\text{m}$ silicon dioxide. Reprinted from [125].

4.2.1 Inductor Design

In this section, several geometries are analyzed for the receiving inductor. These geometries are then compared in terms of quality factor. The quality factor Q of a generic inductor is defined as

$$Q = \frac{\omega L}{R}, \quad (4.1)$$

where L is the inductance value, R is the resistance value, and ω is the working angular frequency. The quality factors of the transmitting and the receiving inductors directly affect the link efficiency η , reported in (2.22). That equation can be expressed as a function of the quality factors of the inductors composing the link

$$\eta = \frac{k^2 Q_1 Q_2 \frac{R_2}{R_L}}{\left(1 + \frac{R_2}{R_L} + k^2 Q_1 Q_2 \frac{R_2}{R_L}\right) \left(1 + \frac{R_2}{R_L}\right)}, \quad (4.2)$$

where Q_1 and Q_2 are the quality factors of the transmitting and the receiving inductors, respectively, k is the coupling coefficient, R_2 is the resistance of the receiving inductor, and R_L is the load resistance.

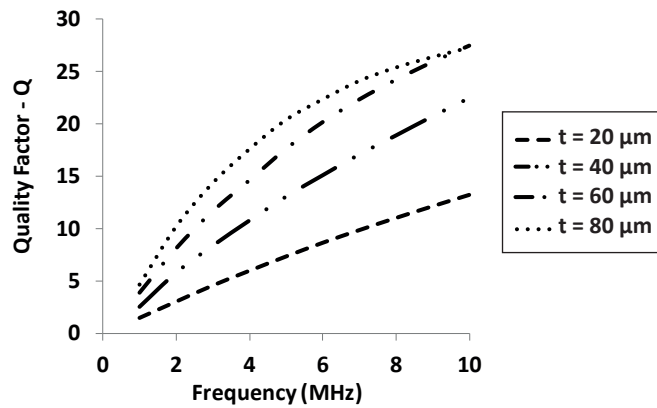


Figure 4.10: A higher trace thickness t decreases the inductor resistance, thus increasing the quality factor. Reprinted from [125].

The simulations reported here are performed with the commercial electromagnetic solver Sonnet. All the inductors are simulated as a thick layer of copper onto a substrate of $525 \mu\text{m}$ silicon + $1 \mu\text{m}$ silicon dioxide. The area of the receiving inductor is set to $14.88 \times 2 \text{ mm}^2$ (Fig. 4.9). This constraint is given by the size of the silicon substrate that will host the microfabricated inductors [20]. Since the inductive link described in [20] operates at 5 MHz, the comparison of the different geometries is performed at that frequency.

A first set of simulations is performed to check the dependence of the quality factor on the trace thickness. The results of these simulations are shown in Fig. 4.10. As previously stated, a higher trace thickness involves a lower resistance, thus increasing the quality factor. However, due to skin and proximity effects, the quality factor cannot be continuously increased by increasing the trace thickness. In this case, a thickness higher than $60 \mu\text{m}$ does not lead to significant improvements in terms of quality factor. The thickness of the microfabricated inductors is set to $60 \mu\text{m}$. This value corresponds to the maximum thickness achievable by using a single layer of photoresist in the microfabrication process. A higher trace thickness is still compatible with the fabrication process, although it requires more than one layer of photoresist.

A second set of simulations is performed to determine the number of turns of the spiral inductor. The results of these simulations are shown in Fig. 4.11. The quality factor is weakly dependent on the number of turns, for a given shape and size of the coil. This is in agreement with the constant-Q assumption [94, 124]. This assumption considers the quality factor of a coil independent of the number of turns, for a given shape and size of the coil. According to the simulation results, the number of turns is fixed equal to 6 (Fig. 4.9). The trace width is equal to $80 \mu\text{m}$ and the inter-trace width is equal to $40 \mu\text{m}$.

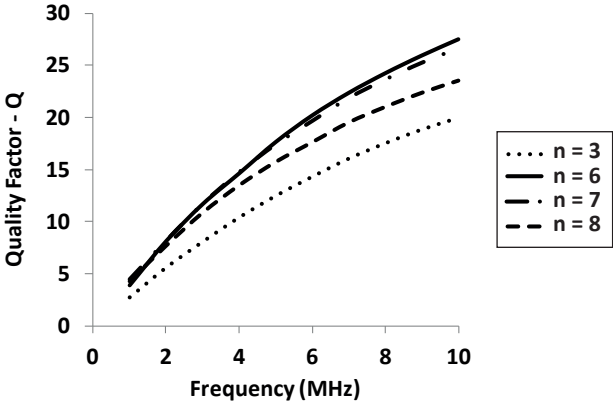


Figure 4.11: The quality factor, for a given shape and size of the spiral inductor, is weakly dependent on the number n of turns. Reprinted from [125].

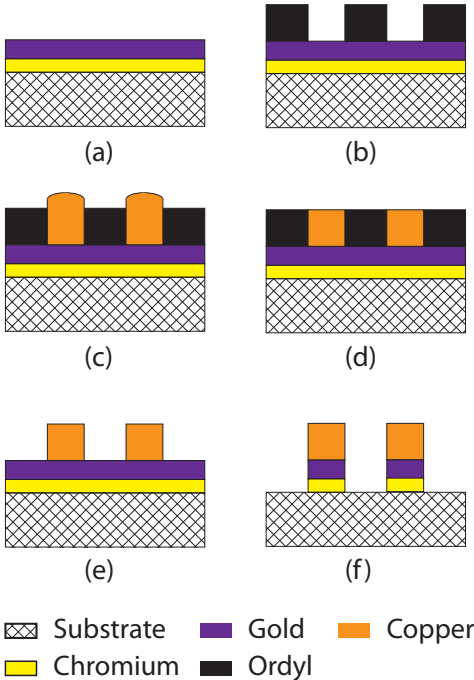


Figure 4.12: Fabrication process flow. (a) Seed layer evaporation; (b) Photolithography; (c) Electroplating; (d) Polishing; (e) Stripping; (f) Wet etching. Reprinted from [125].

4.2.2 Fabrication Process Flow

The inductors are fabricated on silicon substrate. Silicon substrate consists of 525 μm thick, 100 mm silicon $\langle 100 \rangle$ wafers. These substrates are p-type doped and exhibit a resistivity of 0.1 – 100 $\Omega\text{ cm}$. Wafers are delivered with 1 μm wet oxide on the top layer; the oxidation is used to insulate the inductors from the silicon substrate.

Two thin layers of chromium (20 nm) and gold (100 nm) are evaporated by Joule effect on the wafer top layer (Leybold - Optics LAB600H) (Fig. 4.12.a). Chromium layer is used for adhesion; gold layer is used in the next steps as a conductive seed layer for copper electroplating.

A layer of 60 μm Ordyl dry film (Alpha 960 - Elga Europe) is laminated on the wafers. Ordyl dry film is a negative photoresist designed to be developed and stripped in mildly alkaline solutions. The lamination process is performed at 110 $^{\circ}\text{C}$ (PhotoPro33 Laminator). Wafers are pre-heated prior the lamination to dehumidify.

Trenches are opened in the Ordyl film to enable copper electroplating of the inductor traces (Fig. 4.12.b). To that aim, photoresist is exposed to UV light source (Süss MicroTec - MJB4) having a power density of 15 mW/cm^2 . Exposure time is set to 6 seconds. Photoresist developing is performed at room temperature in sodium carbonate (Na_2CO_3 , 0.8%-1.2%) for a time period between 270 seconds and 330 seconds. To remove organic residuals at the bottom of the trenches, plasma cleaning is performed after developing (power: 200 W; pressure: 50 Pa; O_2 flow: 200 sccm; time: 20 s).

Copper is then electroplated inside the trenches (Fig. 4.12.c). Wafers are merged in a copper plating bath (Rohm & Haas - Copper Intervia 8510). The exposed gold layer acts as a cathode. A direct current of 130 mA is forced through it. The current density, defined as the ratio between the cathodic current and the area of the exposed gold layer, is about 40 mA/cm^2 . Electroplating is performed for 1 h and 30 min.

Electroplating is not-uniform along the wafer area. Differences in thickness of several micrometers are measured between different inductors; differences in thickness are also measured between different traces of the same inductor. To achieve a uniform thickness of 60 μm , copper traces are polished until they are planar with the film surface (Fig. 4.12.d). To that aim, chemical-mechanical polishing is performed (STEAG - Mecapol E460) (slurry: 1609BTA; head speed: 45 rpm; plate speed: 50 rpm; pressure: 34.5 kPa; time: 25 min).

Photoresist is then stripped with sodium hydroxide (NaOH , 2.5%) at room temperature (Fig. 4.12.e). The stripping solution swells the Ordyl film; as a consequence, the film is peeled off from the surface. However, stripping of Ordyl between the inductor traces is difficult, since the film tends to get stuck in the narrow inter-trace spaces when swelled. To increase the stripping temperature does not lead to noticeable improvements and can damage the copper by creating a layer of copper(II) hydroxide ($\text{Cu}(\text{OH})_2$) around the traces. To improve the process, stripping solution is stirred and a pipette is used to remove the film.

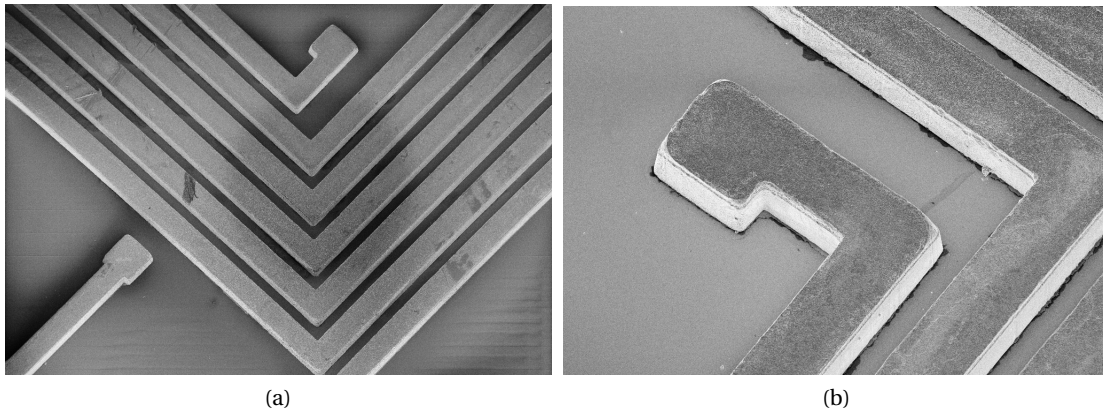


Figure 4.13: SEM pictures of the microfabricated inductors. Reprinted from [125].

Once the film removed, the inductor traces are still short-circuited due to the conductive chromium-gold seed layer (Fig. 4.12.e). To conclude the process, those two metals are removed from the inter-trace spaces by wet etching (Fig. 4.12.f).

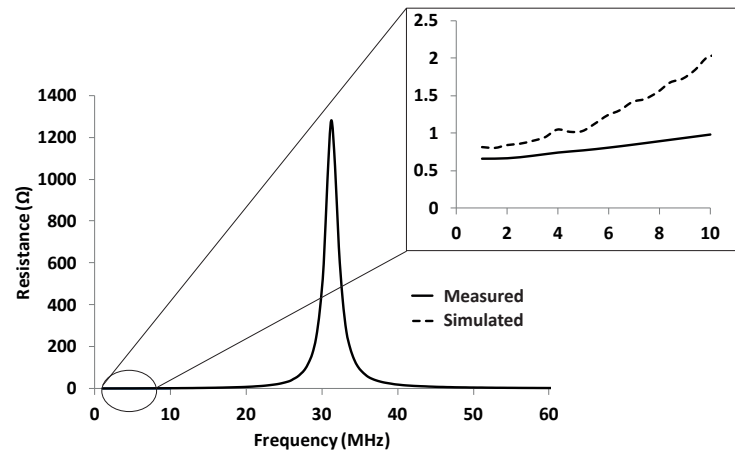
Gold is removed by using $\text{KI} + \text{I}_2$ (25 g/L and 12 g/L, respectively) at room temperature. The etch rate is between 40 and 80 nm/min; however, several minutes are needed to completely remove the gold layer between the traces. The gold etcher reacts with the copper by creating a thick layer of copper(I) iodide (CuI) around the traces; that layer can be removed by using ammonia (NH_3 , 45%), thus exposing again the copper traces.

Chromium is removed by using $\text{KMnO}_4 + \text{Na}_3\text{PO}_4$ (60 g/L and 200 g/L, respectively) at room temperature. The etch rate is about 40 nm/min but, similarly to what happens with gold, several minutes are needed to completely remove the chromium between the traces. Pictures of the inductors, captured with a *Scanning Electron Microscope* (SEM) at the end of the fabrication process, are shown in Fig. 4.13.

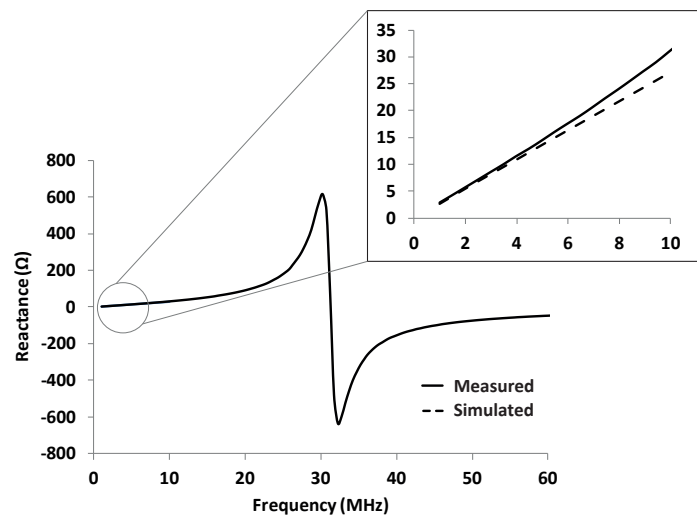
Finally, wafers are cut to separate the inductors and aluminium wire bonding is used to connect the inner edge of each inductor to the contact pad laying outside the spiral. Epoxide resin is applied over the bonding area to prevent short-circuits.

4.2.3 Performance Evaluation

Microfabricated inductors on silicon wafers are measured with a network analyzer (Rohde & Schwarz - ZVL) to check the electrical characteristic. The measured values of resistance and reactance are reported in Fig. 4.14. The comparison with the simulated values, also reported in Fig. 4.14, shows a perfect agreement between measurements and simulations. At the working frequency (5 MHz), the error on the resistance is in the order of few hundreds milliohms, while the error on the inductance is in the order of tenths of nanohenries.



(a) Resistance



(b) Reactance

Figure 4.14: Electrical characteristic of the microfabricated inductors. Measurements show a perfect agreement with the simulations. Reprinted from [125].

Microfabricated inductors are tested within a real setup, in order to measure the link efficiency. Power is sent to the receiving inductors by means of a class-E power amplifier (described in Chapter 5). The received power against the distance between transmitting and receiving inductors is reported in Fig. 4.15. The received power is measured by using a spectrum analyzer (Rohde & Schwarz - ZVL) connected to the receiving inductor. A purely capacitive matching network is used between the instrument and the receiving coil to maximize the received power.

A maximum received power of 8.7 mW is measured within a distance of 6 mm between the inductors. This performance is comparable to that previously reported, where multi-layer spiral inductors are used within the same setup.

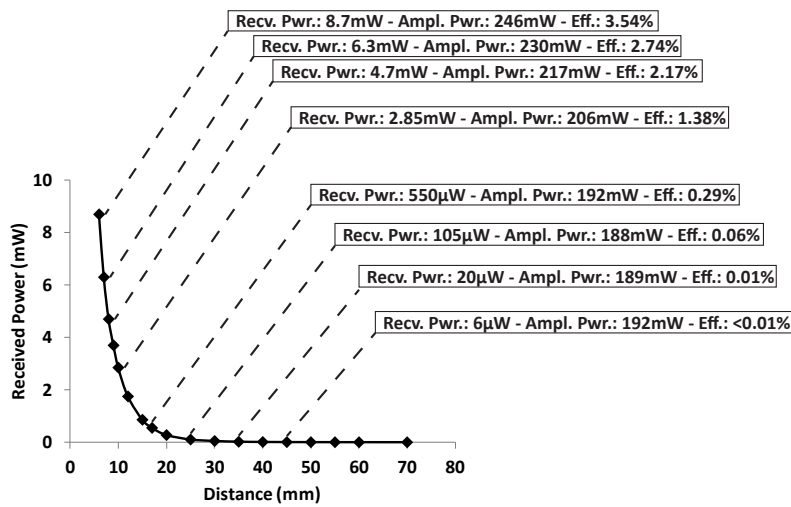


Figure 4.15: Power received by the microfabricated inductor against the distance between transmitting and receiving inductors. Overall efficiency, defined as the ratio between the received power and the power used by the amplifier, is also reported. Reprinted from [125].

4.3 Chapter Contribution and Summary

In this chapter we have described the design and fabrication of mm-sized receiving inductors compatible with the size of the implantable biosensor. Multi-layer, printed spiral inductors and microfabricated spiral inductors have been presented.

Multi-layer, printed spiral inductors with rectangular shape have been studied and measured. The rectangular shape, having the form factor of a needle, is designed to ease the implantation process and reduce the discomfort of the patient. A class-E power amplifier is used to drive those inductors. The system can transfer up to 15 mW over a distance of 6 mm in air. The maximum link efficiency measured is about 4.4%. Furthermore, the system can transfer up to 1.17 mW when a 17 mm beef sirloin is placed between the inductors. If compared with single-layer inductors having the same area, multi-layer inductors exhibit a link efficiency improvement up to 35% and a voltage gain improvement of one order of magnitude. The overhead for these improvements is an increase in thickness of few hundreds micrometers. Moreover, the same performance, in terms of link efficiency and voltage gain, is obtained with a decrease in area of 60% by simply increasing the number of layers.

A microfabrication process is also proposed to further decrease the implantation size. According to the given constraints, several geometries are simulated and compared. Finally, a 60 μ m thick, 6-turn spiral inductor is realized on silicon substrate. The microfabricated coil is measured and tested within a real setup. Powered with a class-E power amplifier, the inductor receives up to 8.7 mW within a distance of 6 mm between the transmitting and the receiving coils. At that distance, the overall efficiency of the link, defined as the ratio between the received power and the power dissipated by the transmitting source, is equal to 3.54%. This performance is comparable to that obtained when multi-layer spiral inductors were used.

5 IronIC Patch

In this chapter, the external power and data transmitter, named IronIC patch, is described at component-level. The patch is conceived to remotely power the implanted sensor through inductive link while enabling bidirectional data transmission. Due to its bendability, the patch can be placed on concave or convex parts of the body to transmit power wirelessly through the body tissues. Power is transmitted by means of an embedded class-E power amplifier driving the external inductor. Short-range, bidirectional communication with the implantable system is also enabled. Downlink communication, from the patch to the implanted sensor is achieved by means of ASK modulation. Uplink communication from the implanted sensor to the patch is achieved by using LSK modulation. Finally, long-range communication between the patch and Android portable devices is enabled by means of Bluetooth connection. In this chapter we describe the architecture of the external patch at component-level, together with its performance.

5.1 Patch Design

Wearable and flexible devices for biomedical measurements have already been presented in the literature. A survey on wearable sensor-based systems for medical aims has been proposed by [40]. Flexible systems to be worn around the wrist have been reported by [41] and [42] for monitoring and evaluation of vital signs. Wearable devices for pulse oximetry have been presented by [43] and [44]. The electronic patch described in [44] is a single unit without wires and does not limit the movements. A flexible and stretchable ECG patch to monitor the heart activity has been proposed by [45]. Fabricated on a polyamide substrate, that patch can fit any body curve. Finally, flexible electronics have been used to fabricate clothes and textiles with built-in sensors. A system based on a textile wearable interface is presented by [46]. The system can acquire different biomedical signals simultaneously. The state of the art of flexible, wearable devices is represented by the “epidermal electronics” [126]. These classes of electronic systems achieve the mechanical characteristic of the epidermis in terms of thickness, elastic modulus, bending stiffness, and density. Several devices, such as body sensors, can be embedded in those systems and placed in every part of the body.

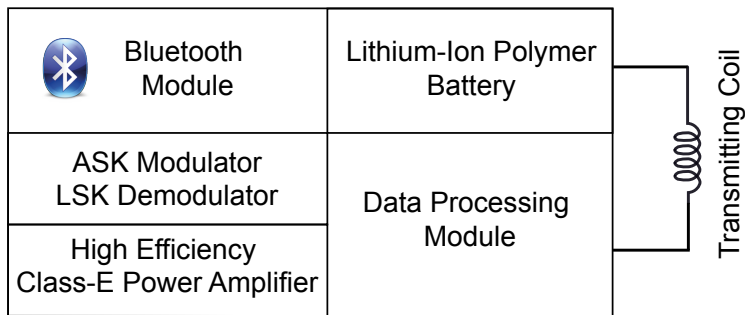


Figure 5.1: Functionalities of the IronIC patch.

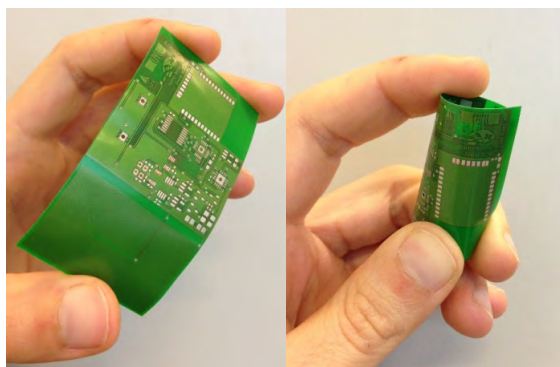


Figure 5.2: The patch is realized on a flexible FR4 substrate, having a thickness of 0.1 mm.

Different from all these devices, the IronIC patch reported in this chapter is not directly involved in the sensing process, but it is designed to provide power and connectivity to implanted systems. Thanks to a high efficiency class-E power amplifier, the patch can transfer power wirelessly through the body tissues by using an inductive link. Bidirectional data communication is enabled by using an ASK modulator (downlink) and an LSK demodulator (uplink). The patch can be remotely controlled by means of an Android application. In this section, the patch is described in detail at component-level. An overview of its functionalities is depicted in Fig. 5.1.

5.1.1 Substrate Description

The patch is fabricated as a double-layer PCB on flexible substrate (Fig. 5.2). The substrate is an FR4 board having a thickness of 0.1 mm. FR4 is a composite material composed of woven fiberglass cloth with an epoxy resin binder. The mechanical parameters of this substrate are reported in Table 5.1. Solder mask is applied on top and bottom layers. Metallic vias are used to connect the two layers. The bendability of the patch enables the user to place it directly over the implantation zone, in convex or concave parts of the body (Fig. 5.3). This reduces the possibility of misalignment between the transmitting and the receiving coils.

Table 5.1: Physical properties of the FR4 patch substrate.

Substrate Thickness	0.1 mm
Copper Initial Thickness	18 μm
Peel Strength (minimum)	0.9 N/mm
Moisture Absorption (maximum)	0.11%
Flexural Strength (minimum)	Length dir. 580 N/mm ² Cross dir. 410 N/mm ²
Density	1.91 g/cm ³

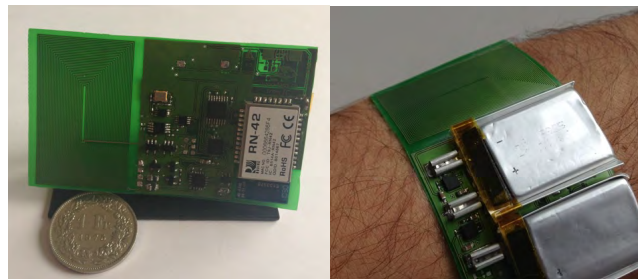


Figure 5.3: The patch can be placed over the implantation zones, in concave or convex parts of the body, to power the implanted sensor and communicate with it.

5.1.2 Class-E Power Amplifier

Amplifiers in class-E, such as that depicted in Fig. 5.4, are commonly used to drive inductive links, due to the high efficiency, theoretically equal to 100% [94, 95, 127]. The MOSFET M_2 , driven by a square waveform, acts as a switch. Capacitors C_3 and C_4 must be tuned to have the current and the voltage across M_2 never different from zero at the same time. Therefore, theoretically the switch does not dissipate power. In Fig. 5.5 is shown the behavior of voltage and current across the switch while the amplifier is well-tuned. Choke inductor L_1 is used to decouple AC signals of the amplifier from DC supply. Inductor L_2 is the transmitting coil. Different sets of equations have been proposed to tune the electrical parameters of a class-E power amplifier [95, 127].

In this design, the amplifier is driven by a 5 MHz square waveform having 50% duty cycle. The circuit to generate that waveform, based on a Pierce oscillator, is also shown in Fig. 5.4. The user can enable the amplifier by means of the Bluetooth module. The ISM radio band provides standard frequencies for this type of applications. The most commonly used are 6.78 MHz and 13.56 MHz. In this work we did not limit our investigation to these two frequencies and we did not pose constraints on the working frequency of the inductive link.

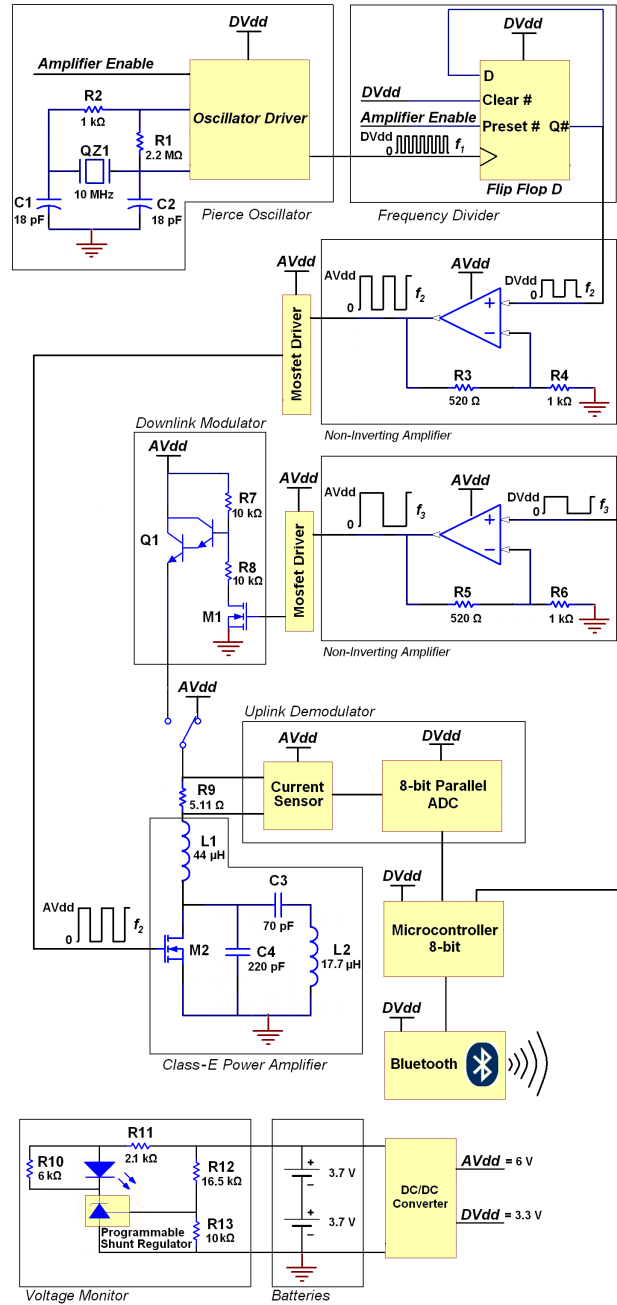


Figure 5.4: Schematic of the IronIC patch at component-level. Reprinted from [36].

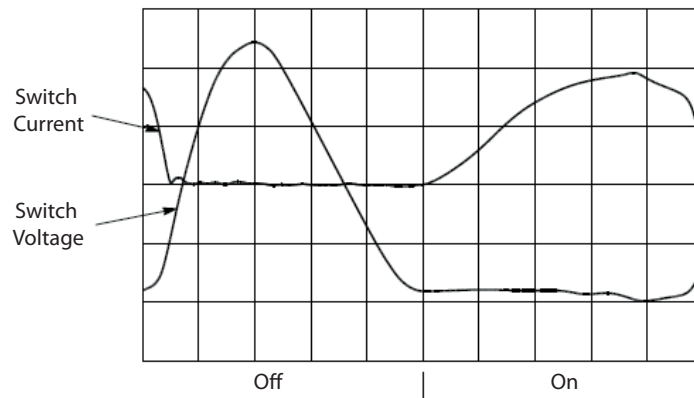


Figure 5.5: Behavior of voltage and current across the switch of a well-tuned class-E amplifier. Reprinted from [95].

5.1.3 Downlink Modulator

Downlink communication is achieved by modulating the amplitude of the current flowing on the transmitting inductor L_2 . To that aim, the supply of the amplifier is switched to the downlink modulator (Fig. 5.4). This block, based on a Darlington pair, is inspired to that presented by [128]. The circuit modulates the supply of the amplifier, thus modulating the current on the transmitting inductor. This modulation is detected by the amplitude demodulator embedded into the implanted sensor. The modulating bitstream is generated by the application running on the remote device and it is transmitted to the patch by means of the Bluetooth module. The bit-rate is set to 100 kbps. The modulation depth is determined by the ratio between resistors R_7 and R_8 .

5.1.4 Uplink Demodulator

Uplink communication is achieved by modulating the load of the internal sensor seen by the transmitter. Load modulation affects not only the current flowing on the external inductor, but also the DC current drawn by the amplifier from the supply and passing through resistor R_9 (Fig. 5.4). To demodulate an uplink bitstream, the voltage drop across resistor R_9 is digitized and analyzed by the microcontroller. A high voltage drop, due to a high current, corresponds to an internal load not short-circuited (digital value 0); conversely, a low voltage drop, due to a low current, corresponds to a short-circuited internal load (digital value 1).

Since the current drawn by the amplifier depends on several factors, such as the distance between the inductors and the interleaved tissues, the threshold between high and low current is updated prior to each communication. The uplink bit-rate is set to 66.6 kbps. This bit-rate is slightly lower than the downlink bit-rate due to the computational time required to perform a real-time threshold check. Data acquired from uplink communication are transmitted via Bluetooth to the application running on the remote device.

5.1.5 Power Supply

The patch is powered by two rechargeable lithium-ion polymer batteries (LiPo). Each battery has a nominal voltage of 3.7 V and weights 3.7 g. The volume of the single battery is $30.6 \times 20.2 \times 3.6 \text{ mm}^3$. Each battery has a capacity of 120 mAh and a maximum discharging rate of 3 A. The maximum charging current is 0.6 A.

The two batteries are placed in series to obtain an overall voltage of 7.4 V (Fig. 5.4). Different supply voltages are generated on-board. The analog voltage AVdd is equal to 6 V. The digital voltage DVdd is equal to 3.3 V.

A voltage monitor is used to check the batteries and prevent over-discharge. The LED is ON when the battery voltage is higher than 6.7 V and switches off when it is lower.

5.1.6 External Inductor

The external transmitting inductor is a 30-turn, planar spiral coil with an area of $38 \times 24 \text{ mm}^2$. The copper thickness is about 40 μm , while the distance between adjacent turns is 150 μm . The width of the copper traces is 250 μm .

As reported in Chapter 4, the geometry of the external inductor strongly affects the performance of the link. By using as receiving inductor the microfabricated structure described in the previous chapter, at 5 MHz the link efficiency (ratio between the power dissipated on the load and the total dissipated power) is about 25%. The link efficiency does not include the losses due to the amplifier. In the following section, the power consumption of the amplifier is obtained and the overall link efficiency is calculated including the losses.

The working frequency is chosen within the band commonly used for remote powering through inductive link, between 1 MHz and 13.56 MHz [26, 27, 31]. In that range, the power absorbed by the tissues is minimum, thus avoiding tissue heating.

5.2 Experimental Results

In this section, the performance of the system is evaluated in terms of transferred power and battery consumption. Moreover, the system is compared to similar devices presented in the literature.

5.2.1 Performance Evaluation

The patch has been tested by using multi-layer printed coils and microfabricated inductors as receiving antennas. The performance obtained with multi-layer inductors has been shown in Section 4.1.3 of the previous chapter. By using as receiving coil the 12-layer, 21-turn, $15 \times 2 \text{ mm}^2$ inductor, the amplifier can transmit about 15 mW over a distance of 6 mm.

Table 5.2: Power consumption of the patch in different operating modes. Table from [36].

	Bluetooth Module	Voltage Monitor	Waveform Gen.	Power Amplifier	Total Power
Stand-by Mode	59.2 mW	14.8 mW	-	-	74 mW
Connection Mode	185 mW	14.8 mW	-	-	199.8 mW
Power Mode (BT Disconnected)	59.2 mW	14.8 mW	125.8 mW	340.4 mW	540.2 mW
Power Mode (BT Connected)	185 mW	14.8 mW	125.8 mW	340.4 mW	666 mW

The link efficiency, as calculated from (2.22) by using the measured values of the inductors, is about 13%. While transmitting 15 mW at 6 mm, the amplifier consumes about 340 mW. Thus, the overall efficiency of the system is about 4.4%.

The performance obtained by means of microfabricated inductors has been reported in Section 4.2.3 of the previous chapter. A maximum received power of 8.7 mW is measured within a distance of 6 mm between the inductors. Within that distance, the link exhibits an efficiency of 25%, while the overall efficiency is equal to 3.54%.

In both cases, downlink communication is successfully tested at 100 kbps by means of ASK modulation, while uplink communication is successfully tested at 66.6 kbps by means of LSK modulation.

5.2.2 Battery Consumption

The system can operate in different modes. A summary of the power drawn from the 7.4 V supply in the different operating modes is reported in Table 5.2.

In *stand-by mode*, the Bluetooth module is not connected but intermittently inquires for possible connections. The analog supply AVdd is disconnected and the amplifier is disabled. Digital circuits are disabled and the microcontroller is in low-power mode. The voltage monitor checks the batteries to prevent over-discharge. The total power consumption is about 74 mW, with an estimated battery duration of about 10 h (80% of battery discharge).

In *connection mode*, the Bluetooth module communicates with a remote device. Consequently, the power consumption increases. This additional power is the only difference as compared to the stand-by mode. The total power consumption in connection mode is about 200 mW, with an estimated battery duration of about 3.5 h.

In *power mode*, analog and digital circuits are enabled and the amplifier is operative. The system transmits power or communicates with the implanted device. It is possible to further split up this operating mode in two cases, according to the Bluetooth status (connected or not). With the chosen tuning, the amplifier consumes about 340 mW. When the Bluetooth is not connected, the measured battery duration in power mode is about 1.5 h.

5.2.3 Comparison with the Literature

The system designed is compared with similar designs reported in literature [26, 27, 31, 34]. In order to compare inductive links dedicated to the remote powering of implantable biosensors, a figure of merit (FOM) is proposed in [29]

$$\text{FOM} = 10 \log \left[\frac{d^2}{D_1 \times D_2} \times \left(\frac{\text{BW}}{f_{\text{carrier}}} \right) \times \eta \right], \quad (5.1)$$

where d is the distance between the inductors, D_1 and D_2 are the diameters of the external and internal inductors (supposed circular), BW is the data-transmission bandwidth, f_{carrier} is the carrier frequency, and η is the link efficiency.

The figure of merit just introduced considers many important aspects of an inductive link. However, specific limitations also exist. First of all, it cannot be applied to those designs where data communication with the implanted devices is not performed, such as in [27, 28, 34]. Moreover, by considering only the diameter of an inductor as an indicator of the size, this figure of merit does not consider the thickness of the inductors. This parameter cannot be neglected, since the volume of a wearable or implantable device affects the discomfort of the patient.

For these reasons, we introduce a new figure of merit $\text{FOM}_{3\text{D}-\eta}$ that can be applied also to those systems where data communication is not performed and includes the volume of the inductors instead of the area

$$\text{FOM}_{3\text{D}-\eta} = 10 \log \left[\frac{d^3}{V_1 + V_2} \times \eta \right], \quad (5.2)$$

where d is the distance between the inductors, V_1 and V_2 are the volumes of the external and internal inductors (any shape), and η is the link efficiency.

Unfortunately, the link efficiency η is not always clearly stated in all the publications; instead, the transmitted power is usually provided. Thus, a further figure of merit $\text{FOM}_{3\text{D}-P}$ is adopted. $\text{FOM}_{3\text{D}-P}$ considers the transmitted power P instead of the link efficiency

$$\text{FOM}_{3\text{D}-P} = 10 \log \left[\frac{d^3}{V_1 + V_2} \times P \right]. \quad (5.3)$$

This figure of merit is slightly biased if compared with the previous, since even a poor design with a low link efficiency can deliver a fair amount of power by transmitting a large quantity of

Table 5.3: Comparison among inductive powering systems for implantable devices. Table elaborated from [36].

Ref.	Coil Area	Coil Thickness	Carrier Frequency	Data Transmission	Transmitted Power	Link Efficiency	Distance	FOM _{3D-η}	FOM _{3D-P}	Transmitter Wearability
[26]	Tx: 1960 mm ² Rx: 314 mm ²	Tx: 9.5 mm Rx: 5 mm	4 MHz	Uplink	11 mW	-	28 mm	-	-19.22 dBW	-
[27]	Tx: $1.32 \cdot 10^5$ mm ² Rx: 79 mm ²	Tx: 300 mm Rx: 13 mm	1 MHz	-	150 mW	1% (min.)	205 mm	-26.62 dB	-14.86 dBW	Surrounding the body
[31]	Tx: 1963 mm ² Rx: 35 mm ²	Tx: 5 mm Rx: 1.9 mm	5 MHz	Downlink	10 mW	-	40 mm	-	-11.89 dBW	-
[34]	Tx: 400 mm ² Rx: 4 mm ²	Tx: $3.8 \cdot 10^{-2}$ mm Rx: $3.8 \cdot 10^{-2}$ mm	915 MHz	-	0.14 mW	0.06% (max.)	15 mm	-8.80 dB	-15.12 dBW	-
Multi-layer Inductor	Tx: 912 mm ² Rx: 30 mm ²	Tx: 0.136 mm Rx: 0.816 mm	5 MHz	Bidirectional	15 mW	4.4% (max)	6 mm	-11.94 dB	-16.61 dBW	Skin Patch
Microfabricated Inductor	Tx: 912 mm ² Rx: 29.76 mm ²	Tx: 0.136 mm Rx: 0.585 mm	5 MHz	Bidirectional	8.7 mW	3.54% (max)	6 mm	-12.67 dB	-18.77 dBW	Skin Patch

power through the primary coil. However, FOM_{3D-P} can be applied to a broader number of cases as compared to the $FOM_{3D-\eta}$.

These two figures of merit have been applied to several devices in literature [26, 27, 31, 34]. The results are listed in Table 5.3 and compared with the performance of the system described in this work.

Even if in some cases our system shows better performance (i.e., while compared with [27] in terms of $FOM_{3D-\eta}$ or while compared with [26] in terms of FOM_{3D-P}), the results obtained with our solutions are generally comparable with those of the other systems reported in the literature. However, while the other systems are focused on the receiver, the device proposed here aims to improve the wearability of the external transmitter. Indeed, the patch is easily wearable and completely autonomous in terms of supply. Finally, it enables bidirectional data communication with implanted sensors.

5.3 Chapter Contribution and Summary

In this chapter, the power and data transmitter named IronIC patch has been described. The device has been realized on a flexible substrate and can be placed on concave or convex parts of the body, directly over the implantation zone. Short-range communication is performed by using ASK modulation (downlink) and LSK modulation (uplink).

Tested with a 12-layer, 21-turn, $15 \times 2 \text{ mm}^2$ receiving inductor the patch can transfer up to 15 mW over 6 mm distance with an overall efficiency of 4.4%; tested with a $14.88 \times 2 \text{ mm}^2$, 6-turn, microfabricated receiving inductor, the system can transfer up to 8.7 mW over 6 mm distance with an overall efficiency of 3.54%. In both cases, downlink communication has been tested up to 100 kbps and uplink communication has been tested up to 66.6 kbps. Finally, the patch has been compared with similar devices reported in the literature in terms of $FOM_{3D-\eta}$ and FOM_{3D-P} .

The patch is connected with Android devices via Bluetooth. Thus, commands and data can be transferred bidirectionally between the user and the implantable device by using the patch as a gateway. The user interface to interact with the patch is depicted in the next chapter.

6 Android Interface

In order to enable long-range communication with the IronIC patch presented in the previous chapter, we designed an Android application running on smartphones and tablets. The application, named BlueCells, provides a user-friendly interface to set the measurement parameters and plot the data provided by the patch. Furthermore, the acquired data can be stored on external memories, such *Secure Digital* (SD) cards.

The application utilizes the patch as a gateway to communicate to the implanted sensor. Every command sent from the application is received from the patch (long-range communication) and directly transmitted by the patch to the implanted sensor (short-range communication). Similarly, every message returned by the implanted sensor is detected by the patch and re-directed to the application.

BlueCells uses the 8b/10b encoding technique to communicate with the implanted sensor through the patch. The 8b/10b provides DC-balancing and bounded disparity, avoiding long sequences of the same logic value. Indeed, short-range communication strongly affects the transmitted power and long sequences of the same logic value can sensibly decrease the power received by the sensor while communicating with the application.

In this chapter, the BlueCells interface is described in detail. Finally, in order to test the performance of the interface, the application has been used with an external sensor for glucose and lactate detection in cell culture medium.

The Android application presented in this chapter has been developed by [129] in collaboration with the author of this thesis.

6.1 Application Description

In this section is described the Android application designed to communicate with the implanted sensor through the patch. The application uses Bluetooth protocol to transmit commands and data and to receive the measured samples.

Chapter 6. Android Interface

In this scenario, the patch acts as a gateway between portable devices (smartphones or tablets) and the implanted biosensor.

The application consists of six activities. These activities enable the user to define the measurement parameters and to start and conclude a measurement session. Moreover, they provide a graphical output of the measurement results.

Welcome Activity

The “Welcome Activity” (Fig. 6.1.a) is the first activity to be run after the user has launched the application. It shows the logo and the background style. The user can pass to the next activity by touching the screen.

Setting Activity

In the “Setting Activity” (Fig. 6.1.b) the user can define the measurement settings. In the first version of the software, the only measurement allowed is the chronoamperometry. Thus, the user can set the sampling period, the sampling instants, and the working electrode to be used among the five available. Furthermore, a moving average filter can be applied to the measured output. Once the parameters are set, the user can start the measurement.

Chart Activity

The “Chart Activity” (Fig. 6.1.c) asks the user to connect the device to the patch by means of the option menu. In the background is shown the chart used by the application to plot the acquired data.

Device List Activity

In the “Device List Activity” (Fig. 6.1.d) are displayed the available Bluetooth devices. The user can select the patch by touching its name on the screen. If the patch is not paired, the user can use the function “Search for other devices”.

Final Chart Activity

In the “Final Chart Activity” (Fig. 6.1.e) every sample acquired during the measurement is plotted in real-time. The signal is conveniently downsized to fit the device screen. The user can stop the measurement at any time with a long touch of the screen. Afterwards, the user can scroll and zoom the signal for a better analysis. Moreover, he can save the signal on the SD card of the device.

End Session Activity

The “End Session Activity” (Fig. 6.1.f) concludes the measurement session. The user can now start a new measurement.

6.1.1 Communication Protocol

The instruction set of the biosensor, reported in Fig. 6.2, consists of five main commands, each having a length of two bytes. The three most significant bits of every instruction define the command type.

The instruction SETUP is used to define the measurement parameters. Two measurements can be performed by the biosensor: *chronoamperometry* (CA) and *cyclic voltammetry* (CV). SETUP[12:11] select the type of analysis. The measurement parameters are set in SETUP[10:0]. Two bits (SETUP[10:9]) define the parameter to be set, while the remaining bits (SETUP[8:0]) contain the numerical value to be assigned. When a cyclic voltammetry is selected, the following parameters can be set: scan rate, minimum voltage, and maximum voltage. When a chronoamperometry is selected, the applied potential can be set.

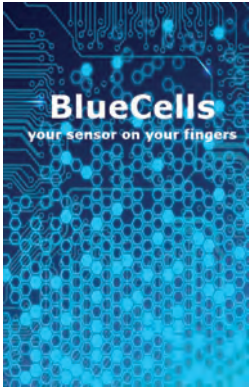
The instruction START is used to begin a measurement. START[12:11] set the measurement to perform (chronoamperometry or cyclic voltammetry) while START[10:8] define the working electrode to be used for the measurement. The remaining bits are ignored.

The instruction GET is used to require a measured sample from the biosensor. Beside the cell current, due to the running measurement, pH and temperature can be recorded by the sensor. GET[12:11] defines which measured sample should be returned. The remaining bits are ignored.

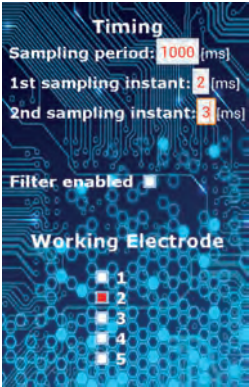
The instruction ABORT is used to stop the measurement. ABORT[10:8] define the working electrode to be stopped. The remaining bits are ignored.

Data are sent from the biosensor to the portable device using the DATA format. DATA[12:0] contain the numerical value of the sample required by the portable device. The remaining bits are ignored.

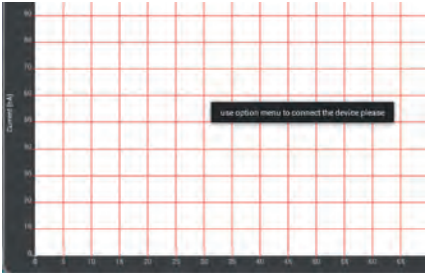
The communication protocol between the portable device and the biosensor is reported in Fig. 6.3, in the case of a cyclic voltammetry. After every command sent by the portable device, the biosensor can send OK (command correctly received), ERROR (command not correctly received) or provide the required DATA if the instruction GET is received. After every command, the portable device waits a fixed timeout. If no response is received within the timeout period, the same command is sent again. After three unsuccessful attempts, the portable device stops the communication and informs the user. If an ERROR is received, the same instruction is sent again.



(a)



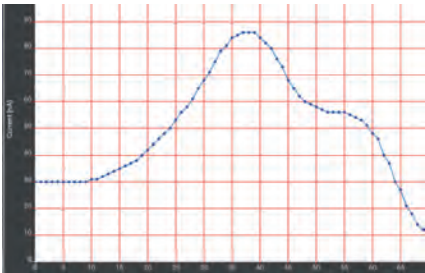
(b)



(c)



(d)



(e)



(f)

Figure 6.1: Activities of BlueCells application. (a) Welcome; (b) Setting; (c) Chart; (d) Device List; (e) Final Chart; (f) End Session. Elaborated from [129].

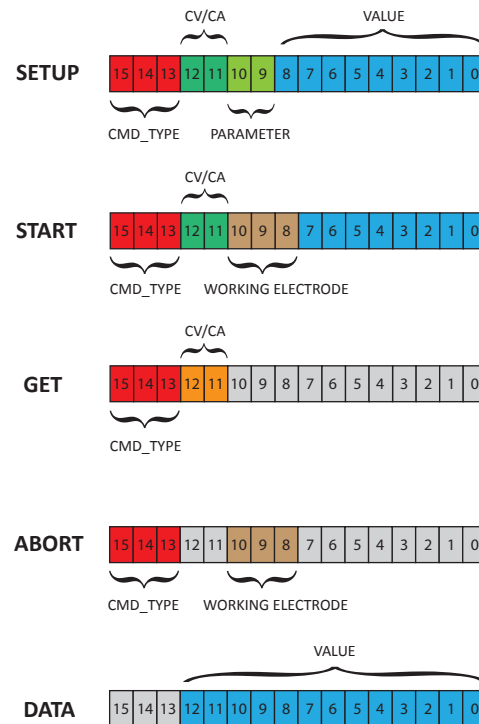


Figure 6.2: Biosensor instruction set. Elaborated from [129].

6.1.2 8b/10b Encoding

The 8b/10b is an encoding technique that maps 8-bit symbols to 10-bit symbols, in order to achieve DC-balancing and bounded disparity [130]. The output stream has a balanced number of zeros and ones and does not contain long sequences of the same logic value. These requirements are important for the application described in this thesis. During downlink communication, the power transmitted by the patch strongly decreases while a logic zero is sent. During uplink communication, the receiving inductor is short-circuited when a logic one is sent; thus, the implanted device does not receive power. For these reasons, a 8b/10b encoding is used to convert both the downlink and uplink bitstreams in order to achieve DC-balancing and avoid long sequences of the same logic value. The downlink bitstream is encoded by the portable device before the transmission and decoded by the implantable sensor; the uplink bitstream is encoded by the implantable sensor and decoded by the portable device. The patch acts as a simple gateway between the portable device and the implantable sensor.

The encoding diagram is shown in Fig. 6.4. As reported in the previous paragraph, every instruction is a 2-byte word. The final output is a 20-bit word that is used for the transmission. During the encoding, every byte is split in two blocks. The 3 most significant bits are encoded using a 3b/4b look-up table, while the 5 least significant bits are encoded using a 5b/6b look-up table. The disparity of the 10-bit word is the sum of the disparity of the 4-bit and 6-bit

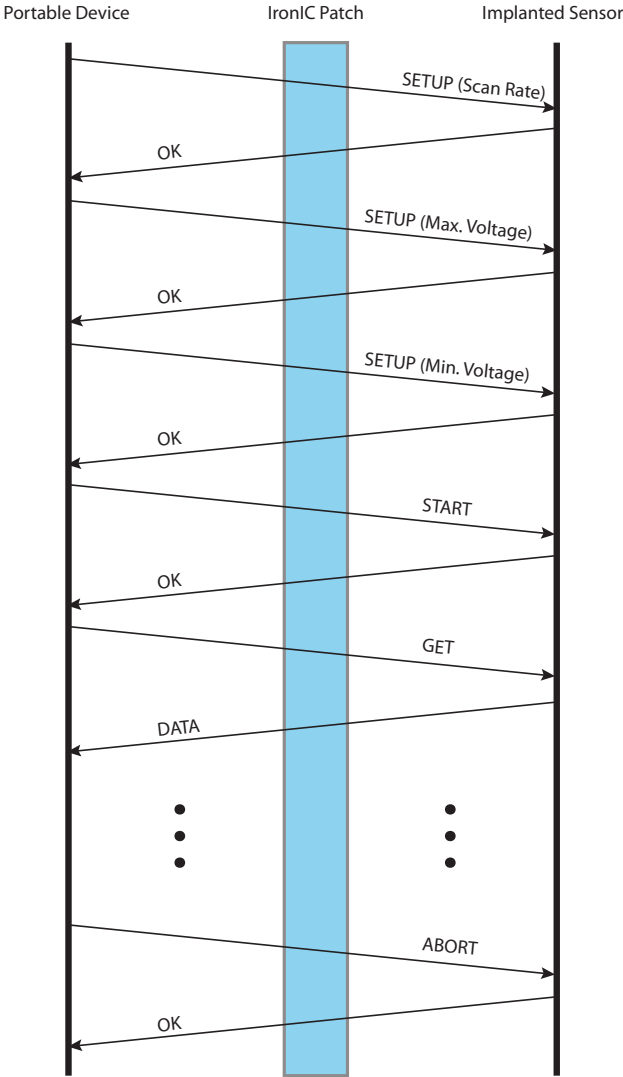


Figure 6.3: Communication protocol for a cyclic voltammetry. Elaborated from [129].

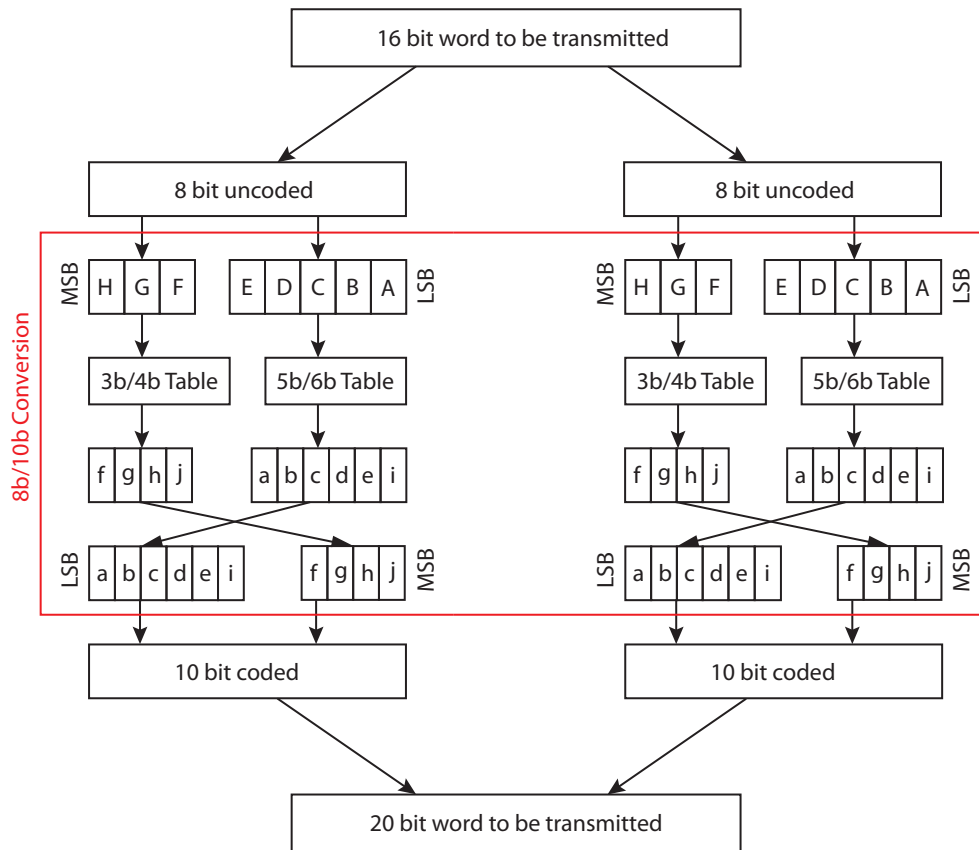


Figure 6.4: Description of the 8b/10b encoding. Elaborated from [129].

blocks. Thus, if the outputs of those table are disparity neutral, the final 10-bit word is perfectly balanced. However, only 6 out of 16 possible combinations of 4 bits and only 20 out of 64 combinations of 6 bits are disparity neutral. The other combinations can have disparity ± 2 .

To avoid combinations of blocks having the same disparity, a variable named *Running Disparity* (RD) is introduced. The variable is used to select the outputs of the 3b/4b and 5b/6b look-up tables. The variable can assume two values, +1 and -1. When RD is equal to +1, the outputs of the tables having disparity -2 are preferred; viceversa, when RD is equal to -1, the outputs having disparity +2 are preferred. When an output with disparity equal to -2 is chosen from one of the two tables, the value of RD is changed to -1. When an output with disparity equal to +2 is chosen from one of the two tables, the value of RD is changed to +1. This behavior is displayed in Fig. 6.5. This method assures that for every 20-bit word the difference between the number of ones and zeros is lower than 2 and there are no more than 5 consecutive ones or zeros.

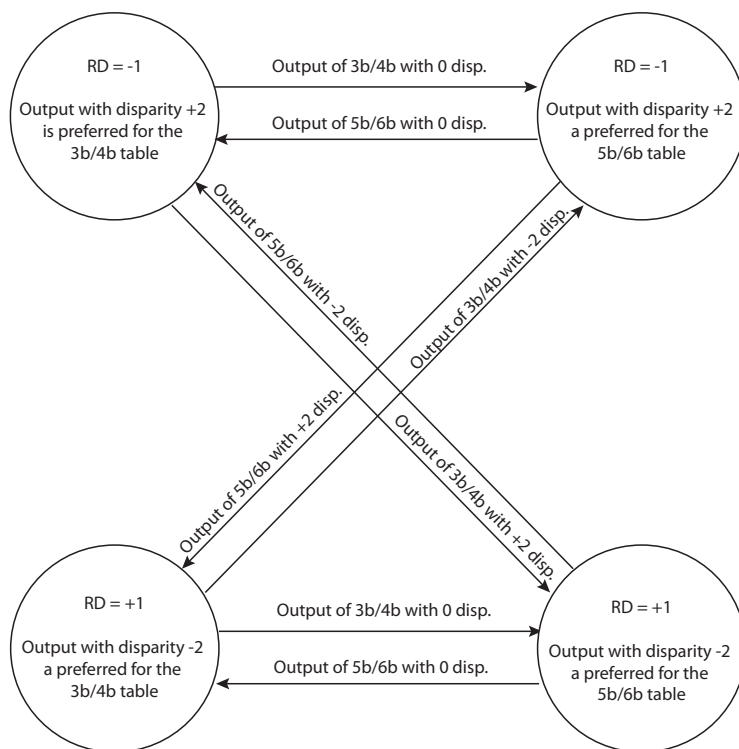


Figure 6.5: Running disparity state diagram. Elaborated from [129].

6.2 Experimental Results

The BlueCells application has been tested with an external sensor in order to evaluate the interface performance. The sensor used for these measurements has been designed to detect glucose and lactate in cell culture medium by means of chronoamperometry [131]. The medium is constantly in contact with a three-electrode cell by using a peristaltic pump. Once the measurement is run, the medium enriched with glucose and lactate is changed at the inlet of the fluidic system every 5 min. Concentration ranges of glucose and lactate are between 5 mM and 25 mM. The change of concentration results in a current variation on the active working electrode.

The results acquired with the interface are reported in Fig. 6.6. The sensitivity for glucose is $(4.67 \pm 1.26) \text{ nA}/(\text{mM} \cdot \text{mm}^2)$ with a detection limit of $(1.41 \pm 0.90) \text{ mM}$, while for lactate is $(12.16 \pm 3.8) \text{ nA}/(\text{mM} \cdot \text{mm}^2)$ with a detection limit of $(0.28 \pm 0.17) \text{ mM}$. These results show that the developed application is suitable for real-time and online monitoring.

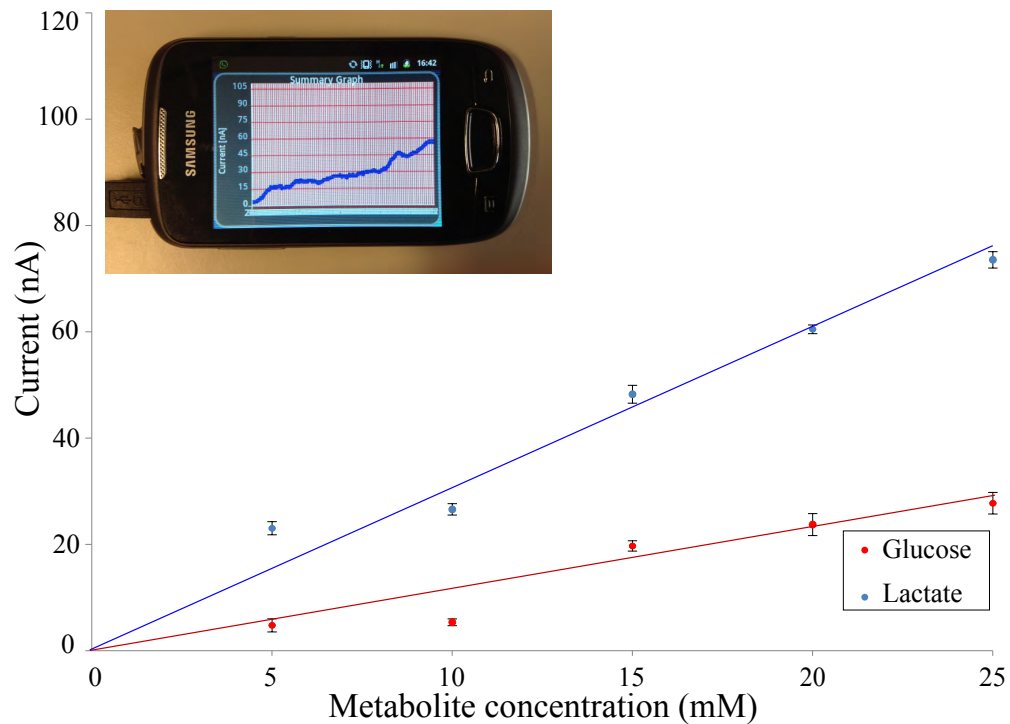


Figure 6.6: Calibration lines of lactate and glucose, obtained by means of the Android application and an external sensor. Offsets have been subtracted from the two lines.

6.3 Chapter Contribution and Summary

In this chapter we have introduced the Android interface, named BlueCells, to interact with the implanted biosensor. The interface, running on smartphones or tablets, exploits the IronIC patch as a gateway to transmit commands to the implanted device. In the same way, the application receives the samples acquired by the implanted device and plot them on the screen of portable devices. Then, the acquired data can be saved on external memories, such as SD cards.

The communication protocol implemented by the application is based on an 8b/10b encoding, to achieve DC-balancing and bounded disparity. Indeed, long sequences of the same logic value can affect the power received by the implanted sensor and compromise its functionality. The 8b/10b encoding assures a difference between ones and zeros lower than 2 for every 20-bit word and the absence of more than 5 consecutive ones or zeros.

Finally, the interface has been tested with an experimental setup to detect glucose and lactate in cell culture medium by means of chronoamperometry. The test proved the capability of our interface to perform real-time, online monitoring of clinically relevant species.

7 Integrated Power Module

In this chapter it is reported the design of the power module embedded in the implantable sensor. The module is needed to collect and store the power provided by the inductive link, while enabling bidirectional data communication. It consists of a voltage rectifier and a low-dropout regulator (designed by [39]) to store and manage the received power, an ASK demodulator to perform short-range downlink communication with the external patch, and an LSK modulator to perform short-range uplink communication.

The whole circuit has been designed in 0.18 μm CMOS technology to be combined with the integrated sensor. In this chapter we report the design, simulation, and test of the module. The functionalities are reported together with the design constraints. Finally, measurements are performed to check the performance of the system while operating within a real setup.

7.1 Design

In order to use the power delivered by the receiving inductor, the implantable sensor must be equipped with a voltage rectifier and a low-dropout regulator. The former converts the AC voltage at the edges of the receiving inductor to a DC voltage between 2.1 V and 3 V. The latter converts that DC voltage to a stable 1.8 V. Finally, an amplitude demodulator and a load modulator are needed to enable downlink and uplink communication, respectively. These circuits (rectifier, regulator, amplitude demodulator, and load modulator) should be integrated within the sensor to provide a stable supply voltage and perform bidirectional, short-range communication.

In this section we describe the design of a power management module including voltage rectifier, ASK demodulator and LSK modulator. The regulator used in the system has been designed by [39] and kindly provided to the author of this thesis. The module is designed in 0.18 μm CMOS technology. A schematic view is shown in Fig. 7.1.

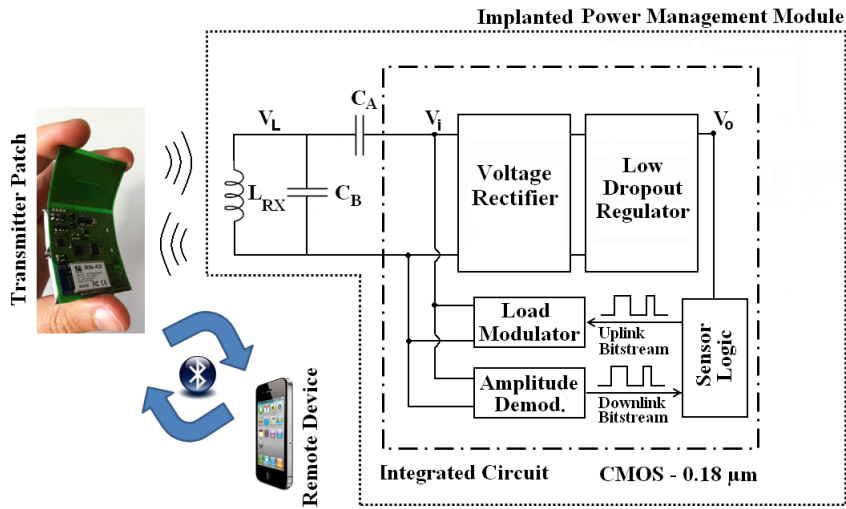


Figure 7.1: The implanted sensor receives power and data from the IronIC patch. The transmitter performs long-range communication with remote devices by means of Bluetooth. The low-dropout regulator has been designed by [39]. Elaborated from [132].

7.1.1 Voltage Rectifier and Load Modulator

The schematic of the voltage rectifier is reported in Fig. 7.2, together with the load modulation unit. At the beginning of the operations, when no power is transmitted and the output capacitor C_o is discharged, switch M_1 is open and switch M_2 is closed. Thus, the equivalent circuit is an half-wave rectifier with four clamping diodes to prevent overvoltage of the output ($V_o \leq 3\text{ V}$). The half-wave configuration has been chosen to have a low threshold rectifier. Furthermore, active rectifiers were not allowed since the only supply source depends on the output of the rectifier itself. Diode D_1 is not integrated within the circuit but is an external component. Thus, a low threshold Schottky diode can be used to increase the efficiency of the rectifier due to the reduced threshold.

Load modulation is performed by switching the transistor M_1 at the input of the rectifier according to the uplink bitstream V_{up} . When a high logic value is transmitted, switch M_1 is closed and short-circuits the input of the rectifier. This is detected by the external patch as a different current flowing on the transmitting inductor. When the receiving inductor is short-circuited, no power is delivered to the load. To avoid the discharge of C_o due to the leakage current of the clamping diodes, switch M_2 is kept open when a high logic value is transmitted.

To prevent the latch-up of transistor M_1 when the input voltage V_i has negative values, its bulk is not connected to ground. Transistors M_a and M_b are used to bias the bulk of M_1 to the lowest between drain and source voltages. To realize that circuit, the bulks of M_1 , M_a , and M_b are fabricated within a separate p-well (triple well, in Fig. 7.3).

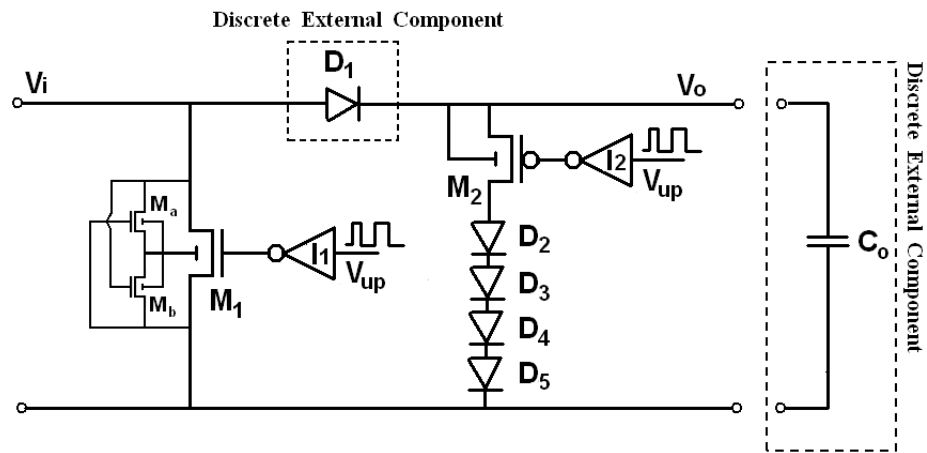


Figure 7.2: Schematic of the voltage rectifier and the load modulation unit. Elaborated from [132].

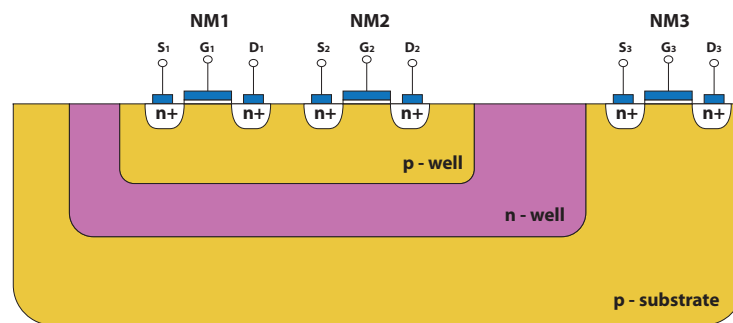


Figure 7.3: In order to have NMOS transistors with bulk potential different from the substrate potential, a triple well has been used. In this example, transistors NM_1 and NM_2 can have bulk potential different from NM_3 .

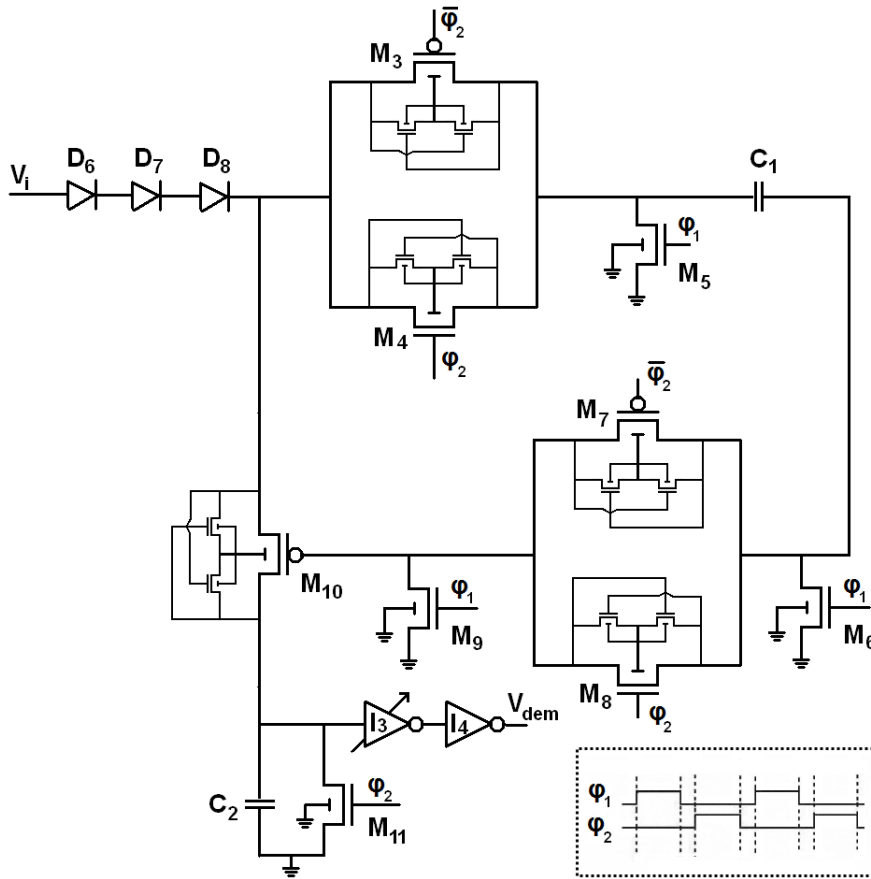


Figure 7.4: Schematic of the amplitude demodulator. The circuit is driven by a two-phase, non-overlapping clock signal (φ_1 and φ_2). Elaborated from [132].

7.1.2 Amplitude Demodulator

The power management module is equipped with an embedded ASK demodulator to read downlink bitstreams transmitted by the external patch. The schematic of the demodulator is reported in Fig. 7.4.

The circuit is driven by a two-phase non-overlapping clock signal (φ_1 and φ_2 , in Fig. 7.4). While signal φ_1 is high, the equivalent circuit is reported in Fig. 7.5a. Capacitor C_2 is charged to the amplitude of the sinusoidal signal V_i through the switch M_{10} . Diodes D_6 , D_7 and D_8 prevent the discharge. The voltage across C_2 is read as a logic value by inverters I_3 and I_4 . During this phase, capacitor C_1 is discharged.

The threshold between high logic values and low logic values at the edges of C_2 depends on several factors, such as modulation depth, distance between the inductors, and power consumption of the implanted sensor. For this reason, the threshold of inverter I_3 can be changed at run-time. The schematic of I_3 is reported in Fig. 7.6. In order to increase the threshold range, a pseudo-logic is used. Block A is used if a threshold lower than classic

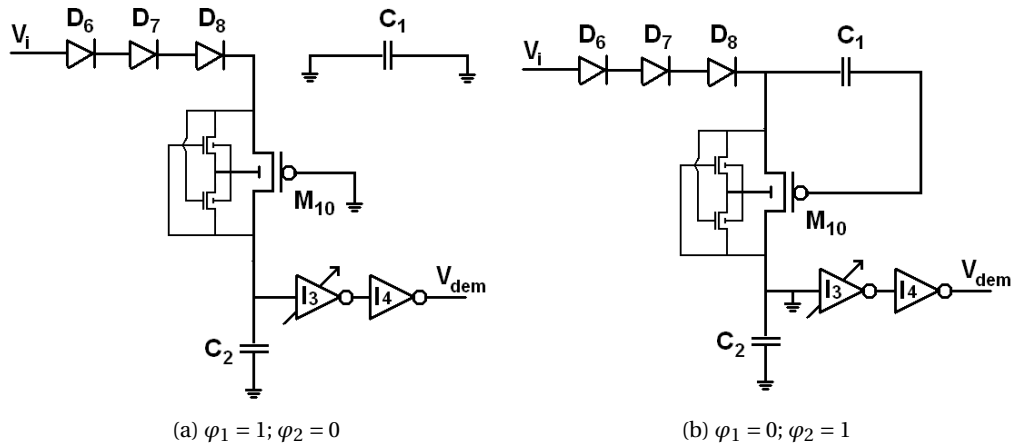


Figure 7.5: Equivalent circuit of the demodulator in Fig. 7.4 while $\varphi_1 = 1$ (a) and $\varphi_2 = 1$ (b). Elaborated from [132].

CMOS inverters is needed. Indeed, in block A the pull-up network is a bench of PMOS, each having a different on-resistance. The appropriate pull-up PMOS among the 32 available can be selected at run-time by driving low the related signal A[0:31]. A higher pull-up resistance involves a lower threshold voltage. Block B can be used instead of block A if a threshold voltage higher than classic CMOS inverters is needed. In block B, the pull-down network is a bench of NMOS, each having a different on-resistance. The appropriate pull-down NMOS among the 32 available can be selected at run-time by driving high the related signal B[0:31]. A higher pull-down resistance involves a higher threshold voltage. The characteristic of inverter I₃ is reported in Fig. 7.7. The group of waveforms on the left (low threshold) is obtained with block A, while the group of waveforms on the right (high threshold) is obtained with block B.

When signal φ_2 is high, the equivalent circuit is reported in Fig. 7.5b. Capacitor C₁, previously discharged, forces a zero voltage between gate and source of M₁₀. Thus, switch M₁₀ is open disregarding the value of V_i. During this phase, capacitor C₂ is discharged for the next reading and the output of inverters I₃ and I₄ is neglected. Similar to what happens with transistor M₁ of the rectifier (Fig. 7.2), a sub-circuit is included to bias the bulk of transistors M₃₋₄, M₇₋₈, and M₁₀ and prevent latch-up.

7.2 Simulations

The power management module is simulated to check its performance. While receiving or transmitting a bitstream, the sensor is assumed in low power mode, with a maximum current consumption of 350 μ A; while performing a measurement, the sensor is assumed in high power mode, with a maximum current consumption of about 1.3 mA. These power consumptions are much higher than those required by the implanted sensor. However, a worst case scenario is assumed to check the capability of the power module to operate with more power-demanding sensors.

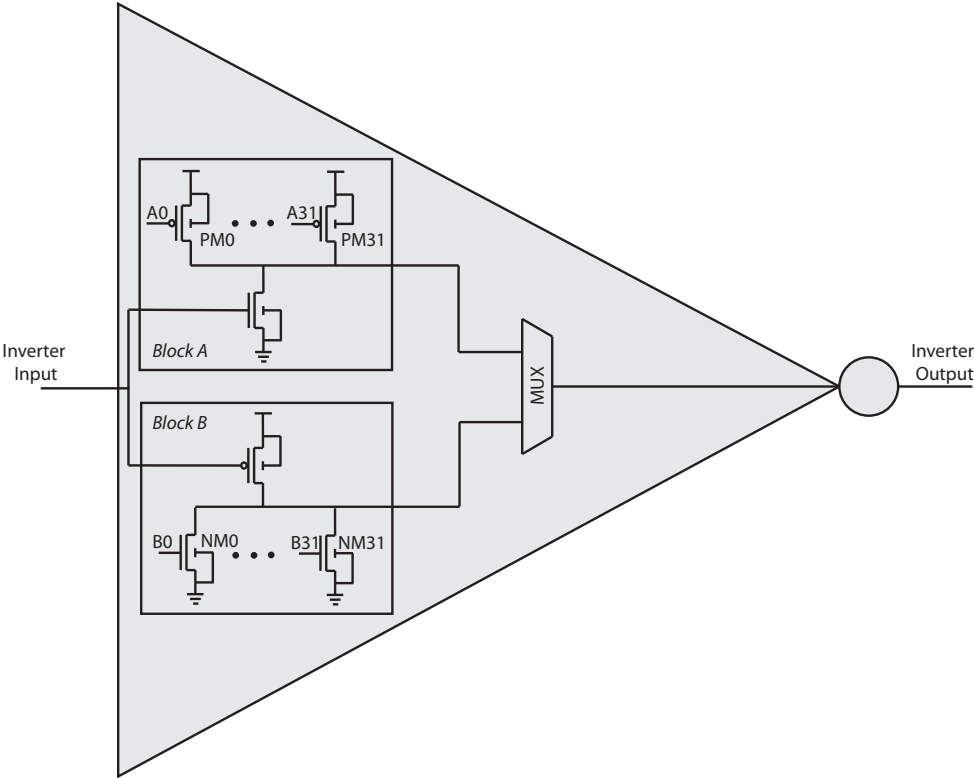


Figure 7.6: Pseudo-logic is used to achieve threshold voltages sensibly higher or lower than those obtained with standard CMOS inverters.

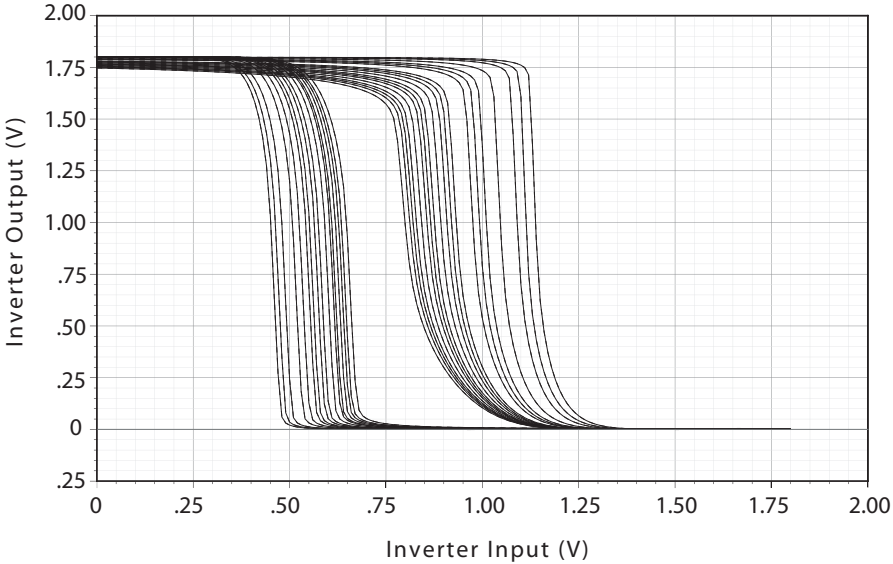


Figure 7.7: Characteristic of inverter I_3 . The different waveforms have been obtained by changing the pull-up transistor of block A (waveforms on the left) or the pull-down transistor of block B (waveforms on the right).

In this set of simulations the power delivered from the receiving inductor to a matched load is equal to 5 mW. This value decreases while downlink communication is performed. While transmitting a high logic value the transferred power is about 3 mW; while transmitting a low logic value the transferred power is about 1 mW. These values have been measured with the IronIC patch described in Chapter 5, within a distance of 10 mm between the inductors.

A purely capacitive matching network (C_A and C_B , in Fig. 7.1) is used between the receiving inductor and the input of the rectifier to achieve impedance matching. Due to the non-linearity of the rectifier, it is not possible to define a linear input impedance for that block. Thus, simulations have been performed to determine an average value of input impedance. With the data just introduced, the transmitted power is maximum when the receiving inductor is matched with a 150Ω load. This value is used to select capacitors C_A and C_B of the matching network.

The regulator designed by [39] has a dropout voltage of 300 mV. Thus, the output voltage V_o of the rectifier should always be higher than 2.1 V to assure the correct functioning of the sensor at 1.8 V.

A simulation is performed to check the behavior of the rectifier, the amplitude demodulator, and the load modulator (Fig. 7.8). Capacitor C_o is charged until it reaches a voltage of 2.75 V at time 270 μ s. Eighteen bits, with a bit-rate of 100 kbps, are sent to the sensor by modulating V_i at time 300 μ s. Those bits are correctly detected at the output V_{dem} of the demodulator at every rising edge of the clock signal φ_1 . During the communication, the output voltage V_o of the rectifier never drops below 2.1 V. This assures the correct functioning of the sensor.

An uplink communication is simulated at time 520 μ s. Several bits are sent with a bit-rate of 100 kbps from the sensor to the IronIC patch by short-circuiting the input of the rectifier according to signal V_{up} of Fig. 7.2. The effect of this modulation on the input voltage V_i is reported in Fig. 7.8. Similar to what happens during downlink communication, the output voltage V_o of the rectifier never drops below 2.1 V during the transmission, thus assuring the correct functioning of the sensor.

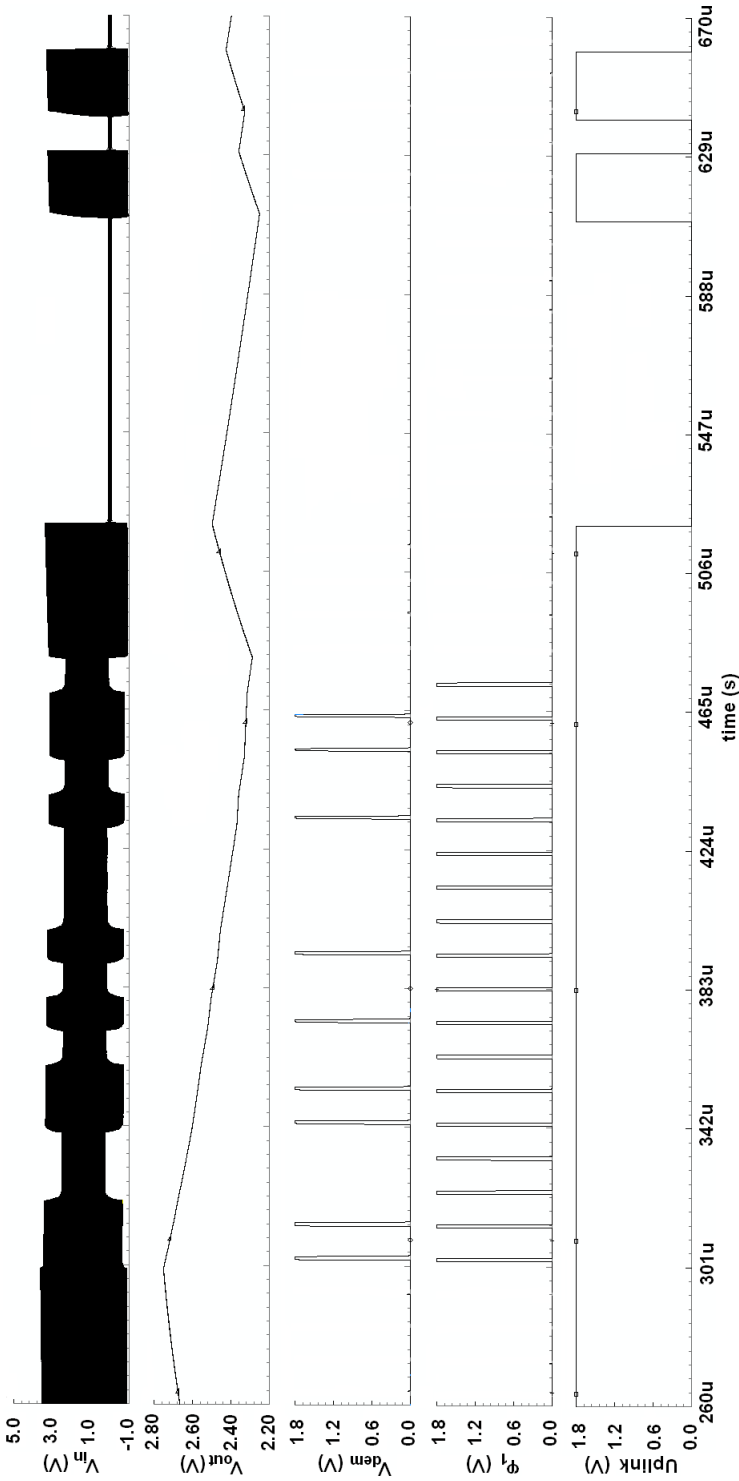


Figure 7.8: The power module is simulated to check its performance. Downlink and uplink communications are correctly performed at 100 kbps. The output of the rectifier is always higher than 2.1 V; thus, the regulator can provide a stable supply voltage of 1.8 V to the sensor. Reprinted from [132].

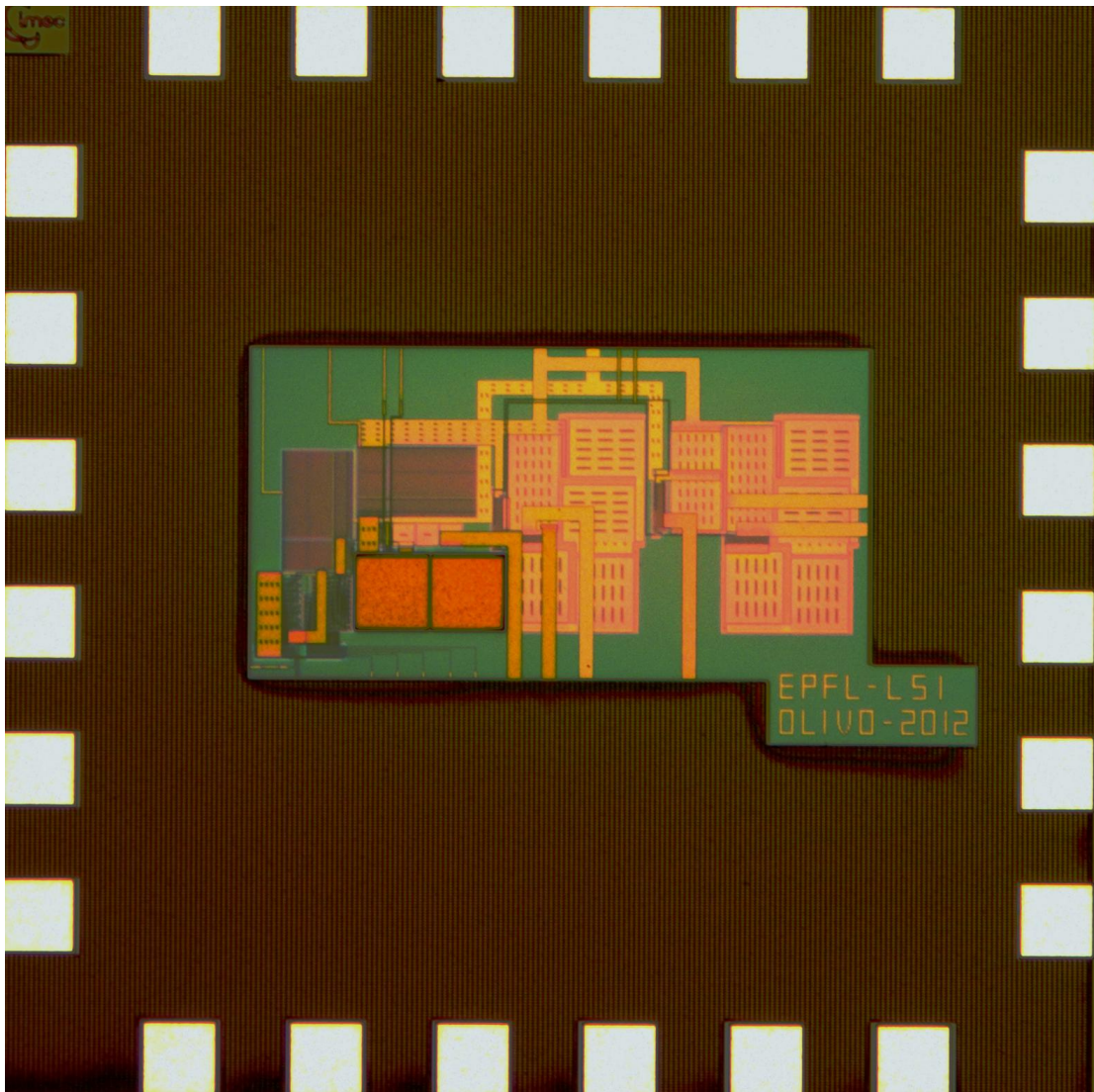


Figure 7.9: Layout of the power module fabricated in $0.18\ \mu\text{m}$ CMOS technology.

7.3 Measurements

The circuit has been manufactured in $0.18\ \mu\text{m}$ CMOS technology. In Fig. 7.9 is reported a picture of the fabricated chip. A measurement setup has been prepared to check the functionalities of the power module while driven by the IronIC patch (Fig. 7.10).

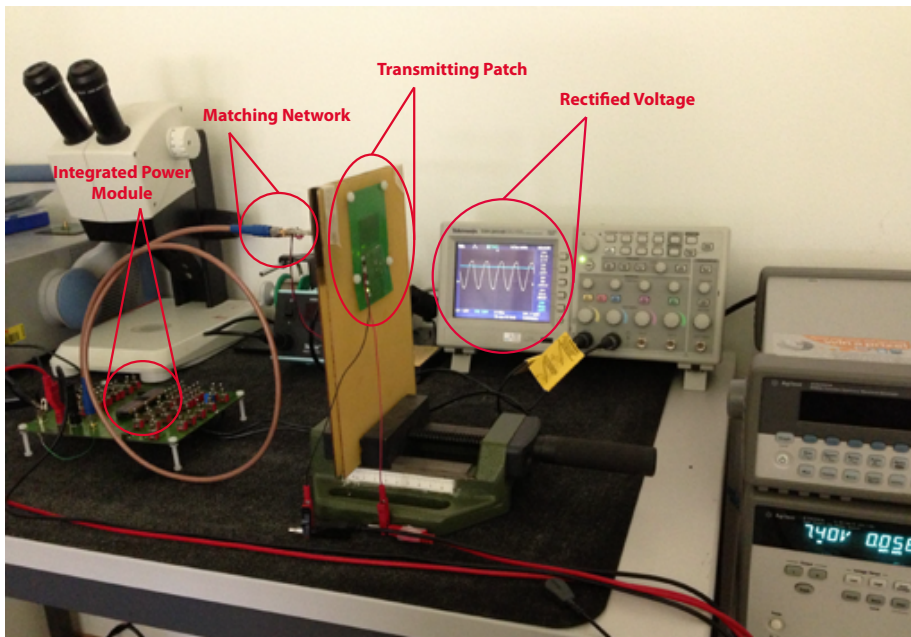


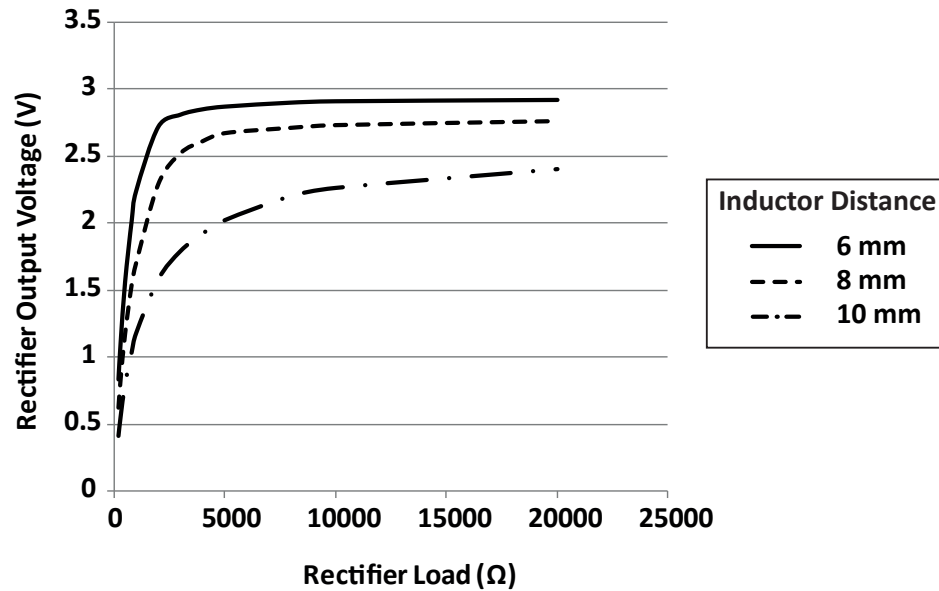
Figure 7.10: The measurement setup used to test the performance of the power module.

7.3.1 Rectifier and Load Modulator

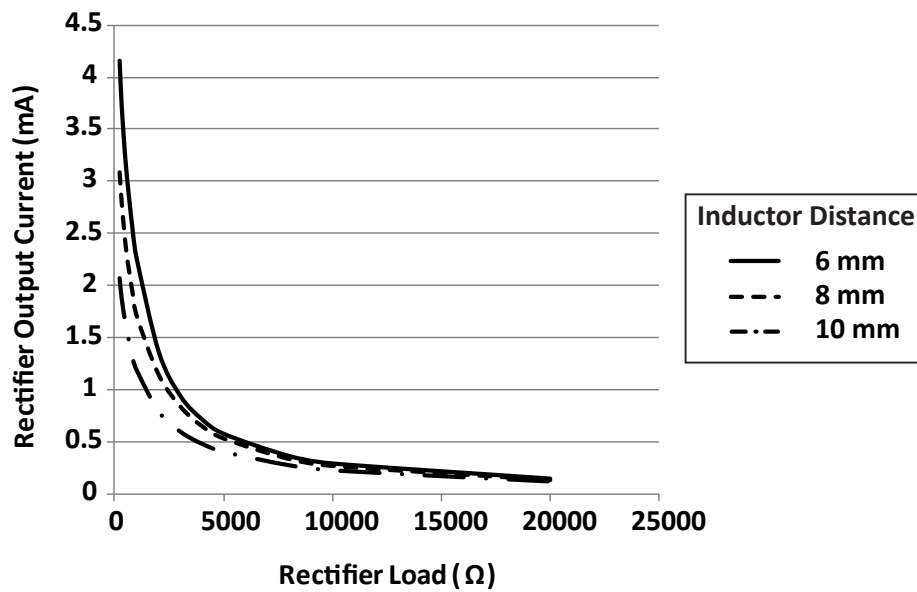
The rectifier reported in Fig. 7.2 has been tested with a variable load at the output. The output voltage and the output current have been plotted against the output load for several distances between the coils. These plots are reported in Fig. 7.11. While the distance between the inductors is 6 mm, the rectifier is able to deliver a maximum current of 2.24 mA with a voltage of 2.2 V. This corresponds to a delivered power of 5 mW.

Higher current consumptions are not allowed to avoid an output voltage lower than 2.1 V. Indeed, 2.1 V is the minimum voltage required by the regulator to assure a stable voltage of 1.8 V to the sensor. Output voltages higher than 3 V are prevented by the clamping diodes D_{2-5} (Fig. 7.2). In Fig. 7.12 is reported a screenshot of the input (CH1) and output (CH2) voltages of the rectifier during the functioning.

The test of the load modulator is reported in Fig. 7.13. The receiving coil is short-circuited according to the uplink bitstream V_{up} (CH3). The uplink bitrate is set to 66.6 kbps. This modulation is detected by the IronIC patch as a variation of the supply current of the transmitting power amplifier. This current variation is converted into a voltage (CH4) and digitized from the patch. Load modulation strongly affects the power carrier at the input of the voltage rectifier (CH1) and the rectified voltage (CH2).



(a)



(b)

Figure 7.11: Output voltage (a) and output current (b) of the rectifier against the output load for several distances between the inductors. Voltages higher than 3 V are prevented by the clamping diodes.

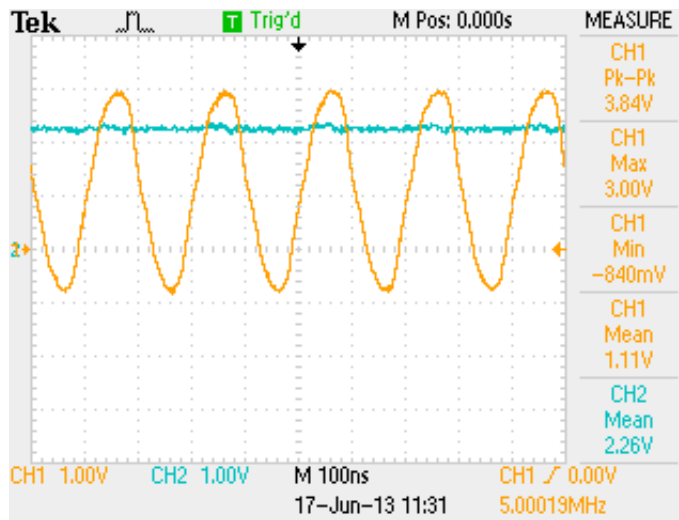


Figure 7.12: Input (CH1) and output (CH2) voltages of the rectifier during the functioning.

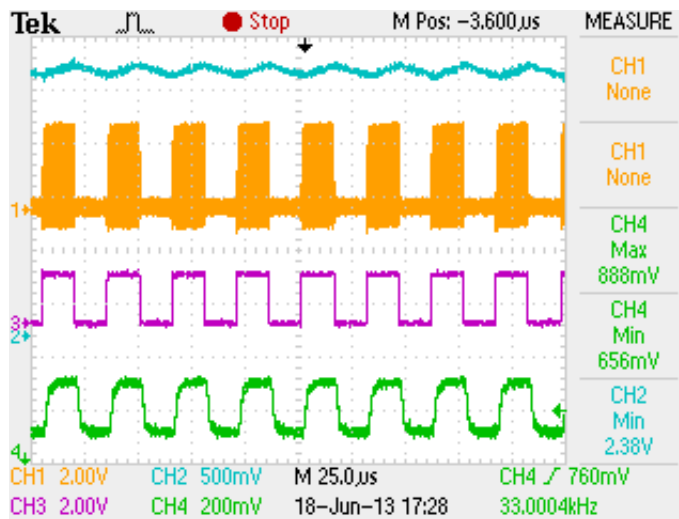


Figure 7.13: Test of the uplink communication through load modulation. The receiving inductor is short-circuited according to the uplink bitstream (CH3). Load modulation is detected as a variation of the supply current of the external class-E power amplifier (CH4). Load modulation affects the power carrier at the input of the rectifier (CH1) and the output voltage of the rectifier (CH2). The downlink bitstream has a bit-rate of 66.6 kbps.

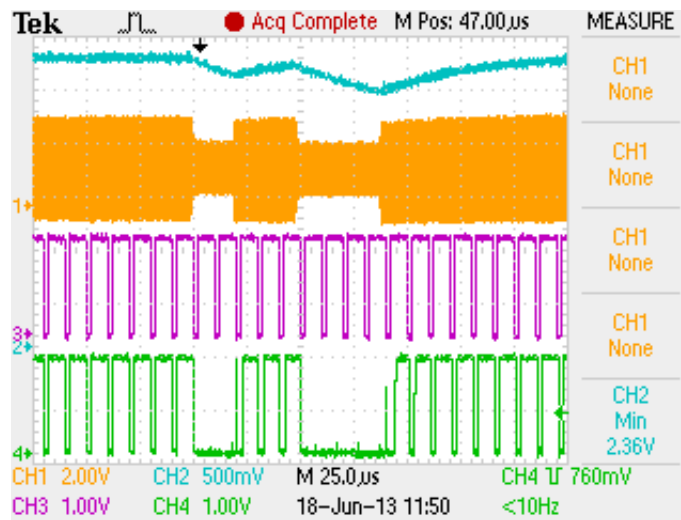


Figure 7.14: Test of downlink communication through ASK modulation. The downlink bitstream is modulated on the power carrier (CH1) at the input of the rectifier. The output of the demodulator (CH4) is valid at the rising edge of the clock signal φ_1 (CH3). Load modulation affects the rectified voltage (CH2). The downlink bitstream has a bit-rate of 100 kbps.

7.3.2 Amplitude Demodulator

Downlink communication is performed by modulating the amplitude of the power carrier. That modulation is detected by the amplitude demodulator and the modulating signal is provided to the sensor as a digital bitstream.

In Fig. 7.14 is reported an example of downlink communication at 100 kbps. The power carrier at the input of the rectifier (CH1) is modulated by the patch. The modulation affects the received power. This is visible on the rectified voltage at output of the rectifier (CH2). However, as long as the rectified voltage does not fall below 2.1 V, the correct functioning of the sensor is assured. Clock signals φ_1 and φ_2 should be provided to the demodulator in order to read the demodulated bitstream. The output V_{dem} of the demodulator (CH4) is valid at the rising edge of clock signal φ_1 (CH3).

7.4 Chapter Contribution and Summary

The integrated module for the management of the received power and bidirectional data communication has been presented in this chapter. The module consists of a voltage rectifier, a low-dropout regulator (designed by [39]), an ASK demodulator for downlink communication, and an LSK modulator for uplink communication.

The module has been designed in 0.18 μm CMOS technology and tested with the IronIC patch to check its performance. While the distance between the inductors is set to 6 mm, the rectifier is able to deliver up to 5 mW to the load, with a voltage higher than 2.1 V. This last requirement

Chapter 7. Integrated Power Module

is imposed by the regulator, that requires a minimum input voltage of 2.1 V to provide a stable output voltage of 1.8 V.

The load modulator has been tested with uplink bitstreams having bit-rate 66.6kbps. The bitstreams are correctly detected by the IronIC patch, while the output voltage of the rectifier never drops below 2.1 V. The amplitude demodulator has been tested with downlink bitstreams having bit-rate 100kbps. The amplitude demodulator properly detects the incoming bitstreams. According to the transmission parameters (such as the distance between the inductors, the power consumed by the sensor, and the modulation depth), the threshold of the demodulator can be adjusted at run-time.

These measurements confirm the functionalities of the power module, that can be used to power the implanted sensor while providing bidirectional data communication. The module can be integrated with the sensing circuit and embedded in the implantable unit.

8 Conclusions and Future Work

In this thesis we have described the research developed within the i-IronIC project. The project aims to design an implantable platform for metabolite monitoring in the human body. The implanted sensor, capable to detect up to five different metabolites, is powered by an external transmitter (IronIC patch) through inductive link. The absence of implanted batteries decreases the discomfort of the patient and avoids periodic battery replacements. Inductive link is used not only for wireless power transfer, but also for bidirectional data communication with the sensor (short-range communication). The use of the same inductive link for powering and communication decreases the power consumption of the sensor, as compared to the case where an implanted RF transmitter is used.

An important part of this work involved the design of an inductive link operating in the megahertz range while a mm-sized receiving inductor is used. Simulations and measurements led to two different solutions for the receiving inductor. Multi-layer printed inductors and microfabricated inductors have been tested in order to reduce the size of the implanted device and ease the implantation process.

The external patch can be controlled by using portable devices, such as smartphones or tablets. An Android application, named BlueCells, has been realized to communicate with the patch (long-range communication) and transmit commands to the implanted sensor. By using the patch as a gateway, the application receives the data acquired by the sensor and plots them in real-time on the device screen. The data can be saved on external memories or analyzed directly on the device.

Finally, an integrated power module has been designed to store and manage the power transmitted by the patch. That system has been designed in 0.18 μm CMOS technology and consists of a voltage rectifier and a low-dropout regulator (designed by [39]) for power management, an ASK demodulator and an LSK modulator for short-range, bidirectional data communication. The system has been conceived to be integrated with the sensor and implanted in the subcutaneous tissues of the body.

8.1 Thesis Summary and Contributions

The contents of this thesis were organized as follows.

In **Chapter 1** we have introduced the i-IronIC project. The aim of the project is the design and realization of an implantable, low cost, health-care device for real-time monitoring of several human metabolites. The contribution of this research work to the i-IronIC project consists of the design and realization of a complete platform to provide power, data communication and remote control to the implantable sensor. High wearability of the transmitting unit, low invasivity of the implanted electronics, integration of the power management module within the sensor, and a reliable communication protocol with portable devices are the key points of this platform.

In **Chapter 2** we have presented the most common techniques for powering implantable sensors. Kinetic, thermoelectric, fuel-cell based, infrared, and low frequency magnetic harvesters have been studied. For each technique, the main key points and drawbacks have been reported together with a description of the state of the art. Finally, special attention has been dedicated to the remote powering through inductive link. This technique enables wireless power transfer and bidirectional data communication by using the magnetic coupling between an external inductor and an implanted coil. The amount of delivered power, together with the possibility to communicate with the sensor without implanted RF transmitters, make the solution particularly suitable for the i-IronIC platform.

In **Chapter 3** we have presented the research dedicated to the design and optimization of an inductive link working with mm-sized receiving inductors. The effects of several factors (such as coil geometry, implantation depth, and misalignments) on the link efficiency have been analyzed by means of simulations. Smaller inductors involve higher optimal frequency, as well as a lower efficiency. Lateral misalignments do not affect the optimal frequency but seriously compromise the link efficiency. Finally, no changes have been noticed while simulating different implantation zones. Particular emphasis has been given to the possibility of operating in the low megahertz range, where tissue absorption is minimum, while using a multi-turn, cm-sized external inductor. Finally, a model has been presented to calculate the electrical properties of multi-turn external inductors starting from their geometry. This model has been realized to aid the designer while optimizing the link efficiency. The model is particularly suitable for dense inductors working at least one order of magnitude below the self-resonance frequency.

In **Chapter 4** we have described the design and fabrication of mm-sized receiving inductors compatible with the size of the implantable biosensor. Multi-layer, printed spiral inductors and microfabricated spiral inductors have been presented. Multi-layer, printed spiral inductors with rectangular shape have been studied and measured. The rectangular shape is chosen to ease the implantation process and reduce the discomfort of the patient. Moreover, the same performance, in terms of link efficiency and voltage gain, is obtained with a decrease in area of 60% by increasing the number of layers. A microfabrication process is also proposed to further

decrease the implantation size. The performance of microfabricated inductors is comparable to that obtained when multi-layer spiral inductors were used.

In **Chapter 5** the power and data transmitter named IronIC patch has been described. The device has been realized on a flexible substrate and can be placed on concave or convex parts of the body, directly over the implantation zone. Short-range communication is performed by using ASK modulation (downlink) and LSK modulation (uplink). The patch is connected with Android devices via Bluetooth. Thus, commands and data can be transferred bidirectionally between the user and the implantable device by using the patch as a gateway.

In **Chapter 6** we have introduced the Android application, named BlueCells, designed to interact with the implanted biosensor. The interface, running on smartphones or tablets, exploits the IronIC patch as a gateway to transmit commands to the implanted device. In the same way, the application receives the samples acquired by the implanted sensor and plots them on the screen of portable devices. The communication protocol implemented by the application is based on an 8b/10b encoding, to achieve DC-balancing and bounded disparity. Finally, the interface has been tested with an experimental setup to detect glucose and lactate in cell culture medium by means of chronoamperometry. The test proved the capability of our interface to perform real-time, online monitoring of clinically relevant species.

In **Chapter 7** we have presented the integrated module for the management of the received power and the bidirectional data communication. The module consists of a voltage rectifier, a low-dropout regulator (designed by [39]), an ASK demodulator for downlink communication, and an LSK modulator for uplink communication. The module has been designed in 0.18 μm CMOS technology and tested with the IronIC patch to check its performance. These measurements confirm the functionality of the module, that can be used to power the implanted sensor while providing bidirectional data communication. The block can finally be integrated with the sensing circuit and embedded in the implantable unit.

8.2 Future Work

In this thesis we laid the foundations for a battery-less, implantable platform dedicated to metabolite detection in the human body. The platform is composed of several blocks: the Android user interface, the IronIC patch, the receiving inductor, and the integrated power module. All these blocks have been deeply described and studied in the previous chapters and different solutions have been proposed to face the challenges of the project. Nevertheless, several improvements need to be done in order to obtain a completely working, standalone prototype. We report here, for every block, possible ideas and roadmaps for future developments.

The Android interface can be improved by implementing a real-time analysis of the acquired waveforms. Thus, the interface can directly communicate to the user the presence and the concentration of the compounds analyzed.

Chapter 8. Conclusions and Future Work

Indeed, at present these details must be extrapolated from the cell current plotted on the screen, making the application difficult to use for persons without biological background.

The patch could be improved in several ways. Its flexibility could be increased by re-arranging the layout of the different components to create lines of bending. Moreover, the power consumption could be reduced by using new *Bluetooth Low-Energy* (BLE) or replacing the Bluetooth protocol with ZigBee. These changes would enable a sensible reduction of the power consumption and would lead to a longer battery lifetime.

The microfabricated antenna could be manufactured directly on the bottom layer of the implantable sensor. This would require *Through Silicon Vias* (TSV) to connect the receiving inductor to the sensor located on the top layer of the platform. The presence of TSV would lead to important changes in the fabrication process flow. However, the additional workload would be compensated by the dramatic size reduction of the implantable device, as compared to the case where multi-layer printed spiral inductors are used.

The integrated power module should be integrated with the sensor, in order to further reduce the size of the implantable device. The use of an internal diode would also contribute to reduce the size. Furthermore, the power consumption of the different blocks of the power module could be optimized. More in particular, ASK demodulator could be improved by reducing the power consumption of the threshold adjustment circuit and by including synchronization with the modulated bitstream. This last change would sensibly improve the downlink communication, by enabling more complex communication patterns.

Besides these improvements, that could sensibly enhance the system described, this thesis has proved the feasibility of a battery-less, remotely controlled approach for implantable systems dedicated to real-time, continuous monitoring of human metabolism. The use of this platform could definitely change the modern medicine by enabling personalized and point-of-care therapies tuned on the response of the patient.

A Appendix

We append here a brief introduction to the theory of scattering parameters. As stated in Chapter 2, at high frequencies, such as in the microwave range, it can be difficult or even impossible to describe a circuit by using voltages and currents. Moreover, the measurement of impedances and admittances may require the use of short-circuits or open-circuits that are not always easy to realize at high frequency. Consequently, in the microwave and optical range a description of the networks by means of scattering parameters is usually preferred [99].

Referring to Fig. A.1, each voltage and current of a two-port network can be divided into two components, one incident and the other reflected

$$\begin{cases} V_n = V_n^+ + V_n^- , \\ I_n = \frac{1}{Z_{0n}}(V_n^+ - V_n^-) , \end{cases} \quad (\text{A.1})$$

where V_n^+ and V_n^- are the incident and the reflected components, respectively, and Z_{0n} is the characteristic impedance of port n . Both voltages and currents are represented as complex vectors.

When the ports of a network have different characteristic impedances, it has sense to normalize the components just introduced:

$$\begin{cases} a_n = \frac{1}{\sqrt{Z_{0n}}} V_n^+ , \\ b_n = \frac{1}{\sqrt{Z_{0n}}} V_n^- . \end{cases} \quad (\text{A.2})$$

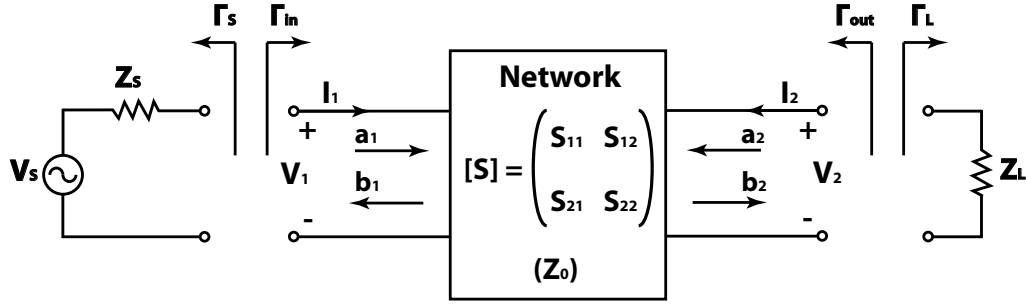


Figure A.1: Schematic description of a two-port network by means of the scattering parameters. Reprinted from [24].

Thus, it is possible to rewrite the voltages and the currents of the network as

$$\begin{cases} V_n = \sqrt{Z_{0n}}(a_n + b_n) , \\ I_n = \frac{1}{\sqrt{Z_{0n}}}(a_n - b_n) , \end{cases} \quad (\text{A.3})$$

where n is still referred to the port. It is now possible to introduce the generalized scattering matrix S

$$\begin{cases} b_1 = S_{11}a_1 + S_{12}a_2 , \\ b_2 = S_{21}a_1 + S_{22}a_2 , \end{cases} \quad (\text{A.4})$$

where the generic element S_{ij} can be written as

$$S_{ij} = \left. \frac{b_i}{a_j} \right|_{a_k=0 \text{ for } k \neq j} . \quad (\text{A.5})$$

In most practical situations, the characteristic impedance is the same for all the ports of a network. In that case, its value is indicated as Z_0 and it is called characteristic impedance of the network. Consequently, the normalization factor will be the same for all the ports and equal to $\sqrt{Z_0}$.

The use of a normalization factor involves some advantages. First, differently from V_n and I_n , the normalized factors a_n and b_n are directly related to the power flow, being $|a_n|^2$ and $|b_n|^2$ the incident power and the reflected power at port n .

The coefficients indicated with the greek letter Γ in Fig. A.1 are called reflection coefficients and describe the ratio of the amplitude of the reflected wave to the amplitude of the incident wave. With relation to Fig. A.1, these coefficients can be written as

$$\begin{cases} \Gamma_S = \frac{Z_S - Z_0}{Z_S + Z_0}, \\ \Gamma_L = \frac{Z_L - Z_0}{Z_L + Z_0}, \end{cases} \quad (\text{A.6})$$

where Z_S and Z_L are the source and load impedances, respectively.

The signals involved in the two-port network reported in Fig. A.1 can be expressed by means of a signal flow graph, as the one shown in Fig. A.2. Incident wave generated by the source V_S is indicated as b_S and it can be shown that $b_S = V_S \frac{\sqrt{Z_0}}{Z_S + Z_0}$.

Referring to Fig. A.2, it is now possible to introduce the definitions of power gain:

$$\begin{cases} G_T \doteq \frac{P_d}{P_{avs}}, & \text{Transducer Power Gain} \\ G \doteq \frac{P_d}{P_i}, & \text{Power Gain} \\ G_A \doteq \frac{P_{avo}}{P_{avs}}, & \text{Available Gain} \end{cases} \quad (\text{A.7})$$

where P_{avs} is the power available from the source, P_i is the power at the input port of the network, P_{avo} is the power available at the output port of the network, and P_d is power delivered to the load. The different power gains can be rewritten as

$$\begin{cases} G_T = \frac{1 - |\Gamma_S|^2}{|1 - \Gamma_{in}\Gamma_S|^2} \cdot |S_{21}|^2 \cdot \frac{1 - |\Gamma_L|^2}{|1 - S_{22}\Gamma_L|^2}, \\ G = \frac{1}{1 - |\Gamma_{in}|^2} \cdot |S_{21}|^2 \cdot \frac{1 - |\Gamma_L|^2}{|1 - S_{22}\Gamma_L|^2}, \\ G_A = \frac{1 - |\Gamma_S|^2}{|1 - S_{11}\Gamma_S|^2} \cdot |S_{21}|^2 \cdot \frac{1}{1 - |\Gamma_{out}|^2}, \end{cases} \quad (\text{A.8})$$

where $\Gamma_{in} = S_{11} + \frac{S_{12}S_{21}\Gamma_L}{1 - S_{22}\Gamma_L}$ and $\Gamma_{out} = S_{22} + \frac{S_{12}S_{21}\Gamma_S}{1 - S_{11}\Gamma_S}$.

An important situation is when the input impedance and the output impedance of the network are conjugately matched to the source impedance and to the load impedance, respectively.

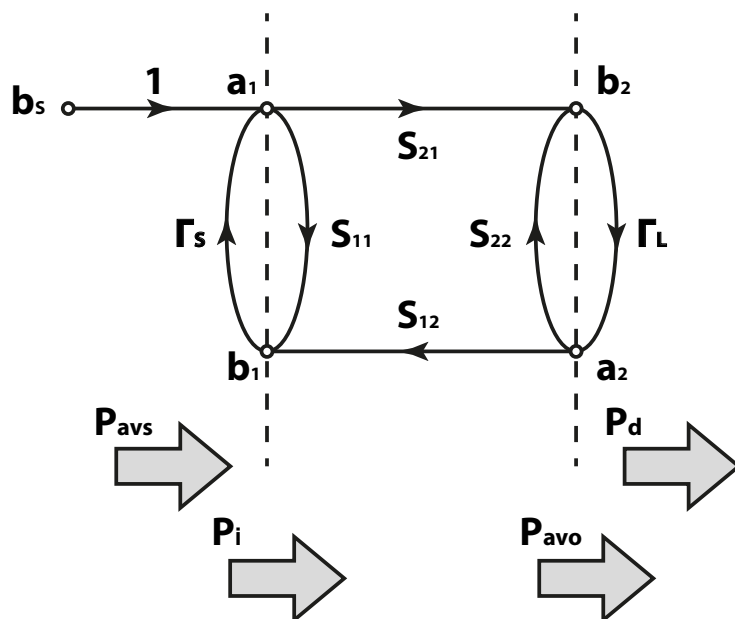


Figure A.2: Signal flow chart of a two-port network. Reprinted from [24].

In this case, named *simultaneous conjugate match*, the three definitions of power gain that we have reported assume the same maximum value.

Finally, it is useful to introduce the voltage gain at the ports of the network. By defining

$$\begin{cases} A_{11} \doteq \Gamma_S S_{11} - 1, \\ A_{12} \doteq \Gamma_S S_{12}, \\ A_{21} \doteq \Gamma_L S_{21}, \\ A_{22} \doteq \Gamma_L S_{22} - 1, \end{cases} \quad (\text{A.9})$$

the voltage gain is equal to

$$A_v = \frac{a_2 + b_2}{a_1 + b_1} = \frac{-A_{21} + (A_{22}S_{21} - S_{22}A_{21})}{A_{22} + (A_{22}S_{11} - S_{12}A_{21})}. \quad (\text{A.10})$$

With these theoretical elements a two-port network, such as an inductive link for remote powering, can be analyzed by means of the scattering parameters. As previously mentioned, the description of a network by means of the scattering parameters is always possible, while it is not always possible or convenient to use an approach based on lumped elements.

Bibliography

- [1] G. Buzsáki, "Large-scale Recording of Neuronal Ensembles," *Nat. Neurosci.*, vol. 7, no. 5, pp. 446–451, May 2004.
- [2] M. Nicolelis, D. Dimitrov, J. Carmena, R. Crist, G. Lehew, J. Kralik, and S. Wise, "Chronic, Multisite, Multielectrode Recordings in Macaque Monkeys," *Proc Natl Acad Sci U S A*, vol. 100, no. 19, pp. 11 041–11 046, Sept. 2003.
- [3] Z. Zumsteg, C. Kemere, S. O'Driscoll, G. Santhanam, R. Ahmed, K. Shenoy, and T. Meng, "Power Feasibility of Implantable Digital Spike Sorting Circuits for Neural Prosthetic Systems," *IEEE T. Neur. Sys. Reh.*, vol. 13, no. 3, pp. 272–279, Sept. 2005.
- [4] K. Wise, D. Anderson, J. Hetke, D. Kipke, and K. Najafi, "Wireless Implantable Microsystems: High-density Electronic Interfaces to the Nervous System," *Proc. IEEE*, vol. 92, no. 1, pp. 76–97, Jan. 2004.
- [5] M. Carrozza, G. Cappiello, S. Micera, B. Edin, L. Beccai, and C. Cipriani, "Design of a Cybernetic Hand for Perception and Action," *Biol Cybern*, vol. 95, pp. 629–644, 2006.
- [6] M. Frost and M. Meyerhoff, "Implantable Chemical Sensors for Real-time Clinical Monitoring: Progress and Challenges," *Curr. Opin. Chem. Biol.*, vol. 6, no. 5, pp. 633 – 641, Oct. 2002.
- [7] A. Poscia, D. Messeri, D. Moscone, F. Ricci, and F. Valgimigli, "A Novel Continuous Subcutaneous Lactate Monitoring System," *Biosens Bioelectron*, vol. 20, pp. 2244 – 2250, 2005.
- [8] M. Romero, F. Garay, and A. Baruzzi, "Design and Optimization of a Lactate Amperometric Biosensor Based on Lactate Oxidase Cross-linked with Polymeric Matrixes," *Sensor Actuat B-Chem*, vol. 131, pp. 590 – 595, 2008.
- [9] A. Guiseppi-Elie, S. Brahim, G. Slaughter, and K. Ward, "Design of a Subcutaneous Implantable Biochip for Monitoring of Glucose and Lactate," *IEEE Sens. J.*, vol. 5, no. 3, pp. 345–355, 2005.
- [10] J. Huang, Z. Song, J. Li, Y. Yang, H. Shi, B. Wu, J. Anzai, T. Osa, and Q. Chen, "A Highly-sensitive L-lactate Biosensor Based on Sol-gel Film Combined with Multi-walled Carbon Nanotubes (MWCNTs) Modified Electrode," *Mater Sci Eng C*, vol. 27, pp. 29 – 34, 2007.

Bibliography

- [11] X. Cui, C. Li, J. Zang, and S. Yu, "Highly Sensitive Lactate Biosensor by Engineering Chitosan/pvi-os/cnt/Iod Network Nanocomposite," *Biosens Bioelectron*, vol. 22, pp. 3288 – 3292, 2007.
- [12] C. Lam, J. James, R. McCluskey, and R. Hunter, "Pulmonary Toxicity of Single-wall Carbon Nanotubes in Mice 7 and 90 Days After Intratracheal Instillation," *Toxicol Sci*, vol. 77, pp. 126–134, 2004.
- [13] D. Warheit, B. R. Laurence, K. Reed, D. Roach, G. Reynolds, and T. Webb, "Comparative Pulmonary Toxicity Assessment of Single-wall Carbon Nanotubes in Rats," *Toxicol Sci*, vol. 77, pp. 117–125, 2004.
- [14] F. Valgimigli, F. Lucarelli, C. Scuffi, S. Morandi, and I. Sposato, "Evaluating the Clinical Accuracy of GlucoMen Day: A Novel Microdialysis-based Continuous Glucose Monitor," *J Diabetes Sci Technol.*, vol. 4, pp. 1182 – 1192, 2010.
- [15] S. Carrara, L. Bolomey, C. Boero, A. Cavallini, E. Meurville, G. De Micheli, F. Grassi, and T. Rezzonico, "Single-metabolite Bio-nano-sensors and System for Remote Monitoring in Animal Models," in *Proceedings of IEEE Sensors Conference*, 2011, pp. 716 – 719.
- [16] A. Cavallini, G. De Micheli, and S. Carrara, "Comparison of Three Methods of Biocompatible Multi-walled Carbon Nanotubes Confinement for the Development of Implantable Amperometric Adenosine-5'-Triphosphate Biosensors," *Sens Lett*, vol. 9, pp. 1838 – 1844, 2011.
- [17] S. Carrara, A. Cavallini, V. Erokhin, and G. De Micheli, "Multi-panel Drugs Detection in Human Serum for Personalized Therapy," *Biosens Bioelectron*, vol. 26, pp. 3914–3919, 2011.
- [18] G. De Micheli, S. Ghoreishizadeh, C. Boero, F. Valgimigli, and S. Carrara, "An Integrated Platform for Advanced Diagnostics," in *IEEE DATE Conf.*, 2011, pp. 1–6.
- [19] S. Ghoreishizadeh, S. Carrara, and G. De Micheli, "Circuit Design for Human Metabolites Biochip," in *IEEE BioCAS Conf.*, 2011, pp. 460 – 463.
- [20] S. Carrara, S. Ghoreishizadeh, J. Olivo, I. Taurino, C. Baj-Rossi, A. Cavallini, M. Op de Beeck, C. Dehollain, W. Burseson, F. Moussy, A. Guiseppi-Elie, and G. De Micheli, "Fully Integrated Biochip Platforms for Advanced Healthcare," *Sensors*, vol. 12, pp. 11 013–11 060, 2012.
- [21] S. Carrara, M. Torre, A. Cavallini, D. De Venuto, and G. De Micheli, "Multiplexing pH and Temperature in a Molecular Biosensor," in *IEEE BioCAS Conf.*, 2010, pp. 146–149.
- [22] C. Boero, "Electrochemical Biosensors for On-line Monitoring of Cell Culture Metabolism," Ph.D. dissertation, EPFL - École Polytechnique Fédérale de Lausanne, 2012.

- [23] A. Du Pasquier, I. Plitz, S. Menocal, and G. Amatucci, "A Comparative Study of Li-ion Battery, Supercapacitor and Nonaqueous Asymmetric Hybrid Devices for Automotive Applications," *J. Power Sources*, vol. 115, no. 1, pp. 171–178, Mar. 2003.
- [24] J. Olivo, S. Carrara, and G. De Micheli, "Energy Harvesting and Remote Powering for Implantable Biosensors," *IEEE Sens. J.*, vol. 11, no. 7, pp. 1573–1586, 2010.
- [25] T. Akin, K. Najafi, and R. Bradley, "A Wireless Implantable Multichannel Digital Neural Recording System for a Micromachined Sieve Electrode," *IEEE J. Solid-St. Circ.*, vol. 33, pp. 109–118, 1998.
- [26] C. Sauer, M. Stanačević, G. Cauwenberghs, and N. Thakor, "Power Harvesting and Telemetry in CMOS for Implanted Devices," *IEEE Trans. Circuits Syst. I, Reg. Papers*, vol. 52, pp. 2605–2613, 2005.
- [27] B. Lenaerts and R. Puers, "An Inductive Power Link for a Wireless Endoscope," *Biosens Bioelectron*, vol. 22, pp. 1390–1395, 2007.
- [28] K. Silay, D. Dondi, L. Larcher, M. Declercq, L. Benini, Y. Leblebici, and C. Dehollain, "Load Optimization of an Inductive Power Link for Remote Powering of Biomedical Implants," in *IEEE ISCAS Conf.*, 2009, pp. 533–536.
- [29] M. Catrysse, B. Hermans, and R. Puers, "An Inductive Power System with Integrated Bi-directional Data-transmission," *Sensor Actuat A-Phys*, vol. 115, pp. 221–229, 2004.
- [30] J. Parramon, P. Doguet, D. Marin, M. Verleyssen, R. Muñoz, L. Leija, and E. Valderrama, "ASIC-Based Batteryless Implantable Telemetry Microsystem for Recording Purposes," *IEEE EMBC*, vol. 5, pp. 2225–2228, 1997.
- [31] G. Gudnason, E. Bruun, and M. Haugland, "A Chip for an Implantable Neural Stimulator," *Analog Integr. Circuits Signal Process.*, vol. 22, pp. 81–89, 2000.
- [32] B. Smith, Z. Tang, M. Johnson, S. Pourmehdi, M. Gazdik, J. Buckett, and P. Peckham, "An Externally Powered, Multichannel, Implantable Stimulator-telemeter for Control of Paralyzed Muscle," *IEEE Trans Biomed Eng.*, vol. 45, pp. 463–475, 1998.
- [33] M. Ahmadi and G. Jullien, "A Wireless-implantable Microsystem for Continuous Blood Glucose Monitoring," *IEEE Trans. Biomed. Circuits Syst.*, vol. 3, pp. 169–180, 2009.
- [34] S. O'Driscoll, A. Poon, and T. Meng, "A mm-sized Implantable Power Receiver with Adaptive Link Compensation," in *ISSCC - Digest of Technical Papers*, 2009, pp. 294–295, 295a.
- [35] Activa RC Recharging System 37751. Medtronic.
- [36] J. Olivo, S. Carrara, and G. De Micheli, "IronIC Patch: A Wearable Device for the Remote Powering and Connectivity of Implantable Systems," in *IEEE I2MTC Conf.*, 2012, pp. 286–289.

Bibliography

- [37] J. Olivo, S. Carrara, and G. De Micheli, "Optimal Frequencies for Inductive Powering of Fully Implantable Biosensors for Chronic and Elderly Patients," in *IEEE Sensors Conf.*, 2010, pp. 99–103.
- [38] J. Olivo, S. Carrara, and G. De Micheli, "Modeling of Printed Spiral Inductors for Remote Powering of Implantable Biosensors," in *5th International Symposium on Medical Information and Communication Technology (ISMICT)*, 2011, pp. 29–32.
- [39] E. Kilinc, F. Maloberti, and C. Dehollain, "Remotely Powered Telemetry System with Dynamic Power-adaptation for Freely Moving Animals," in *IEEE BioCAS Conf.*, 2012.
- [40] A. Pantelopoulos and N. Bourbakis, "A Survey on Wearable Sensor-Based Systems for Health Monitoring and Prognosis," *IEEE Trans. Syst. Man Cybern. Part C Appl. Rev.*, vol. 40, pp. 1–12, 2010.
- [41] J. Kang, T. Yoo, and H. Kim, "A Wrist-Worn Integrated Health Monitoring Instrument with a Tele-Reporting Device for Telemedicine and Telecare," *IEEE Trans. Instrum. Meas.*, vol. 55, pp. 1655–1661, 2006.
- [42] U. Anliker, J. Ward, P. Lukowicz, G. Tröster, F. Dolveck, M. Baer, F. Keita, E. Schenker, F. Catarsi, L. Coluccini, A. Belardinelli, D. Shklarski, M. Alon, E. Hirt, R. Schmid, and M. Vuskovic, "AMON: A Wearable Multiparameter Medical Monitoring and Alert System." *IEEE Trans. Inf. Technol. Biomed.*, vol. 8, pp. 415–427, 2004.
- [43] Y. Mendelson, R. Duckworth, and G. Comtois, "A Wearable Reflectance Pulse Oximeter for Remote Physiological Monitoring," in *Proceedings of the 28th IEEE EMBS Annual International Conference*, 2006.
- [44] R. Haahr, S. Duun, M. Toft, B. Belhage, J. Larsen, K. Birkelund, and E. Thomsen, "An Electronic Patch for Wearable Health Monitoring by Reflectance Pulse Oximetry," *IEEE Trans. Biomed. Circuits Syst.*, vol. 6, pp. 45–53, 2012.
- [45] J. Penders, B. Gyselinckx, R. Vullers, M. De Nil, V. Nimmala, J. van de Molengraft, F. Yazicioglu, T. Torfs, V. Leonov, P. Merken, and C. Van Hoof, "Human++: From Technology to Emerging Health Monitoring Concepts," in *Proceedings of the 5th International Workshop on Wearable and Implantable Body Sensor Networks*, 2008.
- [46] R. Paradiso, G. Loriga, and N. Taccini, "Wearable Health Care System Based on Knitted Integrated Sensors," *IEEE Trans. Inf. Technol. Biomed.*, vol. 9, pp. 337–344, 2005.
- [47] A. Laskovski, M. Yuce, and T. Dissanayake, "Stacked Spiral for Biosensor Telemetry," *IEEE Sens. J.*, vol. 11, pp. 1484–1490, 2011.
- [48] A. Islam and S. Islam, "Design of Multi-Spiral Solenoidal Inductor for Inductive Power Transfer in Biomedical Applications," in *ACES Conf.*, 2011, pp. 369–374.
- [49] J. Zhao, "A New Calculation for Designing Multilayer Planar Spiral Inductors," *Electronics Design, Strategy, News*, vol. 3, pp. 37–40, 2010.

- [50] P. Basset, A. Kaiser, D. Collard, and L. Buchailot, "Process and Realization of a Three-Dimensional Gold Electroplated Antenna on a Flexible Epoxy Film for Wireless Micro-motion System," *J. Vac. Sci. Technol. B*, vol. 20, pp. 1465–1470, 2002.
- [51] Y. Choi and J. Yoon, "Experimental Analysis of the Effect of Metal Thickness on the Quality Factor in Integrated Spiral Inductors for RF ICs," *IEEE Electr. Device. L.*, vol. 25, pp. 76–79, 2004.
- [52] R. Puers, G. Vandevorode, and D. De Bruyker, "Electrodeposited Copper Inductors for Intraocular Pressure Telemetry," *J. Micromech. Microeng.*, vol. 10, pp. 124–129, 2000.
- [53] J. Wu, V. Quinn, and G. Bernstein, "Powering Efficiency of Inductive Links with Inlaid Electroplated Microcoils," *J. Micromech. Microeng.*, vol. 14, pp. 576–586, 2004.
- [54] P. Mitcheson, E. Yeatman, G. Rao, A. Holmes, and T. Green, "Energy Harvesting from Human and Machine Motion for Wireless Electronic Devices," *Proc. IEEE*, vol. 96, no. 9, pp. 1457–1486, Sept. 2008.
- [55] United States Patents Office Patent 5 001 685, 1991.
- [56] M. Hayakawa, "A Study of the New Energy System for Quartz Watches (ii) - The Effective Circuit for the System," in *Congrès Européen de Chronométrie*, 1988, pp. 81–85.
- [57] H. Goto, T. Sugiura, Y. Harada, and T. Kazui, "Feasibility of Using the Automatic Generating System for Quartz Watches as a Leadless Pacemaker Power Source," *Med Biol Eng Comput*, vol. 37, no. 3, pp. 377–380, May 1999.
- [58] R. Tashiro, N. Kabei, K. Katayama, Y. Ishizuka, E. Tsuboi, and K. Tsuchiya, "Development of an Electrostatic Generator that Harnesses the Motion of a Living Body (Use of a Resonant Phenomenon)," *International Journal of the Japan Society of Mechanical Engineers*, vol. 43, no. 4, pp. 916–922, 2000.
- [59] P. Miao, P. Mitcheson, A. Holmes, E. Yeatman, T. Green, and B. Stark, "MEMS Inertial Power Generators for Biomedical Applications," *Microsystem Technologies*, vol. 12, no. 10-11, pp. 1079–1083, Sept. 2006.
- [60] R. Elfrink, T. M. Kamel, M. Goedbloed, S. Matova, D. Hohlfeld, Y. van Andel, and R. van Schaijk, "Vibration Energy Harvesting with Aluminum Nitride-based Piezoelectric Devices," *Journal of Micromechanics and Microengineering*, vol. 19, no. 9, p. 094005, Sept. 2009.
- [61] M. Renaud, K. Karakaya, T. Sterken, P. Fiorini, C. Van Hoof, and R. Puers, "Fabrication, Modelling and Characterization of MEMS Piezoelectric Vibration Harvesters," *Sensor Actuat A-Phys*, vol. 145-146, pp. 380 – 386, 2008.
- [62] [Online]. Available: <http://www.perpetuum.com/>
- [63] [Online]. Available: <http://www.enocean.com/>

Bibliography

- [64] V. Leonov, T. Torfs, P. Fiorini, and C. van Hoof, "Thermoelectric Converters of Human Warmth for Self-powered Wireless Sensor Nodes," *IEEE Sens. J.*, vol. 7, no. 5, pp. 650–657, May 2007.
- [65] R. Vullers, R. van Schaijk, I. Doms, C. van Hoof, and R. Mertens, "Micropower Energy Harvesting," *Solid-State Electron.*, vol. 53, no. 7, pp. 684 – 693, Jul. 2009.
- [66] P. Wright. Energy Harvesting in the Human Body (Implantable Self-powered Sensors). Presentation, BWRC Summer 2008 Retreat.
- [67] P. Favrat, P. Deval, and M. Declercq, "A High-efficiency CMOS Voltage Doubler," *IEEE J. Solid-St. Circ.*, vol. 33, no. 3, pp. 410–416, Mar. 1998.
- [68] J. Dickson, "On-chip High-voltage Generation in MNOS Integrated Circuits Using an Improved Voltage Multiplier Technique," *IEEE J. Solid-St. Circ.*, vol. SC-11, no. 3, pp. 374–378, Jun. 1976.
- [69] J. Silva-Martinez, "A Switched Capacitor Double Voltage Generator," *Proceedings of the 37th Midwest Symposium on Circuits and Systems*, vol. 1, pp. 177–180, 1994.
- [70] J. Wu and K. Chang, "MOS Charge Pumps for Low-voltage Operation," *IEEE J. Solid-St. Circ.*, vol. 33, no. 4, pp. 592–597, Apr. 1998.
- [71] M. Kishi, H. Nemoto, T. Hamao, M. Yamamoto, S. Sudou, M. Mandai, and S. Yamamoto, "Micro Thermoelectric Modules and their Application to Wristwatches as an Energy Source," in *18th International Conference on Thermoelectric*, 1999, pp. 301–307.
- [72] I. Stark and M. Stordeur, "New Micro Thermoelectric Devices Based on Bismuth Telluride-type Thin Solid Films," in *18th International Conference on Thermoelectric*, 1999, pp. 465–472.
- [73] M. Strasser, R. Aigner, C. Lauterbach, T. Sturm, M. Franosch, and G. Wachutka, "Micro-machined CMOS Thermoelectric Generators as On-chip Power Supply," *Sensor Actuat A-Phys*, vol. 114, no. 2-3, pp. 362 – 370, Sept. 2004.
- [74] [Online]. Available: <http://www.poweredbythermolife.com>
- [75] R. Ferrigno, A. Stroock, T. Clark, M. Mayer, and G. Whitesides, "Membraneless Vanadium Redox Fuel Cell Using Laminar Flow," *J. Am. Chem. Soc.*, vol. 124, no. 44, pp. 12 930–12 931, Nov. 2002.
- [76] E. Choban, L. Markoski, A. Wieckowski, and P. Kenis, "Microfluidic Fuel Cell Based on Laminar Flow," *J. Power Sources*, vol. 128, no. 1, pp. 54–60, Mar. 2004.
- [77] S. Wolfson Jr, S. Gofberg, P. Prusiner, and L. Nanis, "The Bioautofuel Cell: a Device for Pacemaker Power from Direct Energy Conversion Consuming Autogenous Fuel," *Transactions - American Society for Artificial Internal Organs*, vol. 14, pp. 198–203, 1968.

- [78] S. Kerzenmacher, J. Ducreé, R. Zengerle, and F. von Stetten, "Energy Harvesting by Implantable Abiotically Catalyzed Glucose Fuel Cells," *J. Power Sources*, vol. 182, no. 1, pp. 1–17, Jul. 2008.
- [79] P. Malachuk, G. Holleck, F. McGovern, and R. Devarakonda, "Parametric Studies of the Implantable Fuel Cell," in *Proceedings of the 7th Intersociety Energy Conversion Engineering Conference*, 1972, pp. 727–732.
- [80] R. Drake, B. Kusserow, S. Messinger, and S. Matsuda, "A Tissue Implantable Fuel Cell Power Supply," *Transactions - American Society for Artificial Internal Organs*, vol. 16, no. 1, pp. 199–205, Apr. 1970.
- [81] N. Mano, F. Mao, and A. Heller, "Characteristics of a Miniature Compartment-less Glucose-O₂ Biofuel Cell and its Operation in a Living Plant," *J. Am. Chem. Soc.*, vol. 125, no. 21, pp. 6588–6594, May 2003.
- [82] R. Bullen, T. Arnot, J. Lakeman, and F. Walsh, "Biofuel Cells and their Development," *Biosens Bioelectron*, vol. 21, no. 11, pp. 2015 – 2045, May 2006.
- [83] J. Phirani and S. Basu, "Analyses of Fuel Utilization in Microfluidic Fuel Cell," *J. Power Sources*, vol. 175, no. 1, pp. 261–265, Jan. 2008.
- [84] K. Murakawa, M. Kobayashi, O. Nakamura, and S. Kawata, "A Wireless Near-infrared Energy System for Medical Implants," *IEEE Eng Med Biol Mag*, vol. 18, no. 6, pp. 70 –72, Nov./Dec. 1999.
- [85] K. Goto, T. Nakagawa, O. Nakamura, and S. Kawata, "An Implantable Power Supply with an Optically Rechargeable Lithium Battery," *IEEE Trans Biomed Eng*, vol. 48, no. 7, pp. 830–833, Jul. 2001.
- [86] T. Ohshiro, R. Calderhead, and J. Walker, *Low Level Laser Therapy: A Practical Introduction*. John Wiley & Sons, 1988.
- [87] S. Suzuki, T. Katane, H. Saotome, and O. Saito, "A Proposal of Electric Power Generating System for Implanted Medical Devices," *IEEE T. Magn.*, vol. 35, no. 5, pp. 3586 –3588, Sept. 1999.
- [88] S. Suzuki, T. Katane, H. Saotome, and O. Saito, "Electric Power-generating System Using Magnetic Coupling for Deeply Implanted Medical Electronic Devices," *IEEE T. Magn.*, vol. 38, no. 5, pp. 3006–3008, Sept. 2002.
- [89] R. Sarpeshkar, *Ultra Low Power Bioelectronics: Fundamentals, Biomedical Applications, and Bio-inspired Systems*. Cambridge University Press, 2010.
- [90] K. Kalyanasundaram and M. Grätzel, "Artificial Photosynthesis: Biomimetic Approaches to Solar Energy Conversion and Storage," *Curr Opin Biotechnol*, vol. 21, no. 3, pp. 298 – 310, Jun. 2010.

Bibliography

- [91] I. McConnell, G. Li, and G. Brudvig, "Energy Conversion in Natural and Artificial Photosynthesis," *Chemistry & Biology*, vol. 17, no. 5, pp. 434 – 447, May 2010.
- [92] M. Katterle, V. Prokhorenko, A. Holzwarth, and A. Jesorka, "An Artificial Supramolecular Photosynthetic Unit," *Chem. Phys. Lett.*, vol. 447, no. 4-6, pp. 284 – 288, Oct. 2007.
- [93] M. Grätzel, "Photoelectrochemical Cells," *Nature*, vol. 414, no. 6861, pp. 338–344, Nov. 2001.
- [94] B. Lenaerts and R. Puers, *Omnidirectional Inductive Powering for Biomedical Implants*. Springer, 2009.
- [95] N. Sokal, "Class-E RF Power Amplifiers," *QEX*, pp. 9–20, Jan./Feb. 2001.
- [96] M. Ghovanloo and K. Najafi, "A High Data Transfer Rate Frequency Shift Keying Demodulator Chip for the Wireless Biomedical Implants," in *45th Midwest Symposium on Circuits and Systems (MWSCAS'02)*, vol. 3, 2002, pp. 433–436.
- [97] E. Ngai, K. Moon, F. Riggins, and C. Yi, "RFID Research: An Academic Literature Review (1995-2005) and Future Research Directions," *International Journal of Production Economics*, vol. 112, no. 2, pp. 510 – 520, Apr. 2008.
- [98] A. Poon, S. O'Driscoll, and T. Meng, "Optimal Operating Frequency in Wireless Power Transmission for Implantable Devices," in *29th Annual International Conference of the IEEE Engineering in Medicine and Biology Society*, 2007, pp. 5673–5678.
- [99] D. Pozar, *Microwave Engineering - Third Edition*. John Wiley & Sons, 2005.
- [100] A. Poon, S. O'Driscoll, and T. Meng, "Optimal Frequency for Wireless Power Transmission into Dispersive Tissue," *IEEE T. Antenn. Propag.*, vol. 58, pp. 1739–1750, 2010.
- [101] *IEEE Standard for Safety Levels with Respect to Human Exposure to Radio Frequency Electromagnetic Fields, 3 kHz to 3 GHz*, IEEE Std. Std. C95-1, 1999.
- [102] ICNIRP. Guidelines for Limiting Exposure to Time-Varying Electric, Magnetic and Electromagnetic Fields (Up to 300 GHz). [Online]. Available: www.icnirp.de
- [103] S. Michaelson, "Health Implications of Exposure to Radiofrequency/Microwave Energies," *Brit J Ind Med*, vol. 39, pp. 105–119, 1982.
- [104] P. Bernardi, M. Cavagnaro, S. Pisa, and E. Piuze, "Specific Absorption Rate and Temperature Increases in the Head of a Cellular-phone User," *IEEE T. Microw. Theory.*, vol. 48, no. 7, pp. 1118 –1126, Jul. 2000.
- [105] D. Hermann and K. Hossmann, "Neurological Effects of Microwave Exposure Related to Mobile Communication," *J Neurol Sci*, vol. 152, no. 1, pp. 1 – 14, Nov. 1997.
- [106] [Online]. Available: <http://visiblehuman.epfl.ch/>

- [107] S. Gabriel, R. Lau, and C. Gabriel, "The Dielectric Properties of Biological Tissues: III. Parametric Models for the Dielectric Spectrum of Tissues," *Phys Med Biol*, vol. 41, pp. 2271–2293, 1996.
- [108] H. Wheeler, "Formulas for the Skin Effect," *Proceedings of the IRE*, vol. 30, no. 9, pp. 412–424, Sept. 1942.
- [109] C. Zierhofer and E. Hochmair, "Geometric Approach for Coupling Enhancement of Magnetically Coupled Coils," *IEEE Trans Biomed Eng*, vol. 43, no. 7, pp. 708–714, Jul. 1996.
- [110] B. Kuhn and N. Ibrahim, "Analysis of Current Crowding Effects in Multiturn Spiral Inductors," *IEEE T. Microw. Theory.*, vol. 49, no. 1, pp. 31–38, Jan. 2001.
- [111] S. Gevorgian, H. Berg, H. Jacobsson, and T. Lewin, "Basic Parameters of Coplanar-Strip Waveguides on Multilayer Dielectric/Semiconductor Substrates, Part 1: High Permittivity Superstrates," *IEEE Microw. Mag.*, vol. 4, no. 2, pp. 60–70, Jun. 2003.
- [112] P. Pieters, K. Vaesen, S. Brebels, S. Mahmoud, W. De Raedt, E. Beyne, and R. Mertens, "Accurate Modeling of High-Q Spiral Inductors in Thin-film Multilayer Technology for Wireless Telecommunication Applications," *IEEE T. Microw. Theory.*, vol. 49, no. 4, pp. 589–599, Apr. 2001.
- [113] U. Jow and M. Ghovanloo, "Modeling and Optimization of Printed Spiral Coils in Air, Saline, and Muscle Tissue Environments," *IEEE Trans. Biomed. Circuits Syst.*, vol. 3, no. 5, pp. 339–347, Oct. 2009.
- [114] S. Mohan, M. del Mar Hershenson, S. Boyd, and T. Lee, "Simple Accurate Expressions for Planar Spiral Inductances," *IEEE J. Solid-St. Circ.*, vol. 34, no. 10, pp. 1419–1424, Oct. 1999.
- [115] C. Neagu, H. Jansen, A. Smith, J. Gardeniers, and M. Elwenspoek, "Characterization of a Planar Microcoil for Implantable Microsystems," *Sensor Actuat A-Phys*, vol. 62, no. 1-3, pp. 599 – 611, Jul. 1997.
- [116] G. Kendir, W. Liu, G. Wang, M. Sivaprakasam, R. Bashirullah, M. Humayun, and J. Weiland, "An Optimal Design Methodology for Inductive Power Link with Class-E Amplifier," *IEEE Trans. Circuits Syst. I, Reg. Papers*, vol. 52, pp. 857–866, 2005.
- [117] C. Sullivan, "Optimal Choice for Number of Strands in a Litz-Wire Transformer Winding," *IEEE T. Power. Electr.*, vol. 14, pp. 283–291, 1999.
- [118] A. Lotfi and F. Lee, "A High Frequency Model for Litz Wire for Switch-Mode Magnetics," in *Conf. Rec. IEEE IAS*, 1993.
- [119] A. Makharia and G. Rincón-Mora, "Integrating Power Inductors onto the IC-SOC Implementation of Inductor Multipliers for DC-DC Converters," in *Conf. Rec. IEEE-IECON*, vol. 1, 2003, pp. 556–561.

Bibliography

- [120] R. Merrill, T. Lee, H. You, R. Rasmussen, and L. Moberly, "Optimization of High Q Integrated Inductors for Multi-Level Metal CMOS," in *IEEE IEDM Conf.*, 1995, pp. 983–986.
- [121] C. Tang, C. Wu, and S. Liu, "Miniature 3-D Inductors in Standard CMOS Process," *IEEE J. Solid-St. Circ.*, vol. 37, pp. 471–480, 2002.
- [122] P. Basset, A. Kaiser, B. Legrand, D. Collard, and L. Buchaillot, "Complete System for Wireless Powering and Remote Control of Electrostatic Actuators by Inductive Coupling," *IEEE/ASME Trans. Mechatronics*, vol. 12, pp. 23–31, 2007.
- [123] J. Olivo, S. Carrara, and G. De Micheli, "A Study of Multi-Layer Spiral Inductors for Remote Powering of Implantable Sensors," *IEEE Trans. Biomed. Circuits Syst.*, vol. 7, pp. 536–547, 2013.
- [124] W. Ko, S. Liang, and C. Fung, "Design of radio-frequency powered coils for implant instruments," *Med Biol Eng Comput*, vol. 15, pp. 634–640, 1977.
- [125] J. Olivo, S. Carrara, and G. De Micheli, "Micro-fabrication of High-thickness Spiral Inductors for the Remote Powering of Implantable Biosensors," *Microelectron. Eng.*, vol. 113, pp. 130–135, 2014.
- [126] D. Kim, N. Lu, R. Ma, Y. Kim, R. Kim, S. Wang, J. Wu, S. Won, H. Tao, A. Islam, K. Yu, T. Kim, R. Chowdhury, M. Ying, L. Xu, M. Li, H. Chung, H. Keum, M. McCormick, P. Liu, Y. Zhang, F. Omenetto, Y. Huang, T. Coleman, and J. Rogers, "Epidermal Electronics," *Science*, vol. 333, pp. 838–843, 2011.
- [127] F. Raab, "Idealized Operation of the Class-E Tuned Power Amplifier," *IEEE T. Circuits. Syst.*, vol. CAS-24, pp. 725–735, 1977.
- [128] B. Ziaie, S. Rose, M. Nardin, and K. Najafi, "A Self-oscillating Detuning-insensitive Class-E Transmitter for Implantable Microsystems," *IEEE Trans. Biomed. Eng.*, vol. 48, pp. 397–400, 2001.
- [129] L. Foglia, "Design and Development of Android-based Communication Platform for Implantable Metabolite Sensors," Master's thesis, EPFL - University of Genova, 2013.
- [130] A. Widmer and P. Franaszek, "A DC-Balanced, Partitioned-Block, 8b/10b Transmission Code," *IBM J Res Dev*, vol. 27, pp. 440–451, 1983.
- [131] C. Boero, J. Olivo, S. Carrara, and G. De Micheli, "A Self-contained System with CNTs-based Biosensors for Cell Culture Monitoring," *IEEE J. Emerg. Sel. Topic Circuits Syst.*, vol. 2, pp. 658 – 671, 2012.
- [132] J. Olivo, S. Ghoreishizadeh, S. Carrara, and G. De Micheli, "Electronic Implants: Power Delivery and Management," in *IEEE DATE*, 2013, pp. 1540–1545.

JACOPO OLIVO

Electronic Engineer

📍 Chemin des Côtes 4
1020 - Renens
Switzerland

☎ +41 (0)78 76 23 752

✉ jacopo.olivo@yahoo.it



Design and realization of wearable platforms for **RF power transmission** based on **RFID technology**
Sizing and simulation of antennas for RFID and NFC applications
Design and layout of **analog integrated circuits** for implantable healthcare devices



09. 2009 **EPFL - École Polytechnique Fédérale de Lausanne** Lausanne, Switzerland
11. 2013 **Research Engineer and Doctoral Candidate**

- Design and realization of a novel platform for wireless power transfer based on RFID technology. Project cited on several international media (BBC, Daily Mail, The Wall Street Journal)
- Sizing and simulation of printed and microfabricated antennas, having a size compatible with the implantation in the human body
- Design and development of wearable electronics connected to Android devices via Bluetooth
- Responsible for the development of electronics within the IronIC project, funded with 5.500.000 CHF by the Swiss Confederation and private enterprises, both Swiss (Nestlé) and international (Menarini, Italy)
- Responsible for the costing and purchase of measuring equipment, with a personal budget of 50.000 CHF and direct communication with the suppliers
- Responsible for the selection and management of collaborators for short-term projects (6 months)

01. 2009 **University of Bologna** Bologna, Italy
08. 2009 **Research Engineer**

- Design and development of a kinetic energy harvester based on the wristwatch Seiko Kinetic in collaboration with Telecom Italia
- Realization of a system based on electromagnetic transduction for the fast startup of wearable sensors



09. 2009 **EPFL - École Polytechnique Fédérale de Lausanne** Lausanne, Switzerland
11. 2013 Degree: PhD in Electronic Engineering

01. 2006 **University of Bologna** Bologna, Italy
12. 2008 Degree: Master in Electronic Engineering
Grade: 110/110 Summa Cum Laude

09. 2002 **University of Bologna** Bologna, Italy
01. 2006 Degree: Bachelor in Electronic Engineering
Grade: 110/110 Summa Cum Laude



Technical

- Sizing and simulation of antennas for RFID and NFC applications
- Design and fabrication of printed circuit boards (PCB) and embedded systems. Expertise on soldering techniques
- Microcontroller programming and development of microcontroller-based circuits (ATMEL AVR, 8-bit and 16-bit)
- Design and test of analog integrated circuits (IC) in 0.18µm CMOS technology. Knowledge of tape-out procedures and collaboration with Europractice IC Service for IC manufacturing
- Confident with the most important electrical and electronic measurement instruments: oscilloscope, function generator, waveform generator, spectrum analyzer, vector network analyzer (VNA)
- Expertise on the basic microfabrication techniques in clean-room: metal evaporation, dry film lamination, photoresist development, electroplating, chemical-mechanical polishing (CMP), plasma cleaning, wet etching, scanning electron microscope (SEM)

Relational

- Adaptation to multicultural environments, acquired during the doctorate working closely with colleagues from all around the world
- Capability to recognize the key points of a problem and propose practical solutions, developed during the doctorate
- Team management skills, learnt by coordinating several master projects and by means of "human resources management" courses within the EPFL program "Management, Technology and Entrepreneurship"
- Organization skills and competence to work under tight time constraints, developed during the doctorate by scheduling the work load according to the different deadlines, for example publication and tape-out deadlines

Computer

• *Operating Systems*

Windows (XP, Vista, 7) – Mac OS X (Mountain Lion)

• *Programming and Hardware Description Languages*

C/C++ – Labview – Assembler – VHDL

• *Tools*

Cadence (integrated circuit design) – Altium (PCB design) Orcad (PCB design) – Matlab (numerical environment) Sonnet (EM analysis) – AVR Studio (microcontroller) EDK (development on FPGA)

• *Graphic Tools*

Sketch Up – Adobe Illustrator

Languages

• **Italian**

Mother Tongue

• **English**

Understanding: Advanced (B2)

Speaking: Advanced (B2)

Writing: Advanced (B2)

• **French**

Understanding: Advanced (B2)

Speaking: Intermediate (B1)

Writing: Intermediate (B1)



Personal Data

Year of birth: 1983

Nationality: Italian

Residence Permit: B

Interests

Sailing on the lake and on the sea. Member of the EPFL Sailing Club and the Folle Brise Sailing Club. Participation to boat-races on the Lemman lake

Mountain activities: ski, alpine-ski, and hiking. Member of the EPFL Mountain Club

Track motorcycling. Motorbike tuning for track use

Licenses

A (motorcycles) and B (cars)

Swiss Sail Permit (D Type – sailing boats on inland waters)

International Sailing License (sailing and motor boats)



Journal

Energy Harvesting and Remote Powering for Implantable Biosensors,

J. Olivo, S. Carrara, and G. De Micheli, *IEEE Sensors Journal*, Vol. 11, No. 7, pp. 1573-1586, 2011

Biofuel Cells and Inductive Powering as Energy Harvesting Techniques for Implantable Sensors,

J. Olivo, S. Carrara, and G. De Micheli, *Science of Advanced Materials*, Vol. 3, No. 3, pp. 420-425, 2011

A Study of Multi-layer Spiral Inductors for Remote Powering of Implantable Sensors,

J. Olivo, S. Carrara, and G. De Micheli, *IEEE Trans. on Biomedical Circuits and Systems*, Vol. 7, No. 4, pp. 536-547, 2013

Micro-fabrication of High-thickness Spiral Inductors for the Remote Powering of Implantable Biosensors,

J. Olivo, S. Carrara, and G. De Micheli, *Microelectronic Engineering Journal*, Vol. 113, pp. 130-135, 2014

New Approaches for Carbon Nanotubes-based Biosensors and their Application to Cell Culture Monitoring,

C. Boero, J. Olivo, G. De Micheli and S. Carrara, *IEEE Trans. on Biomedical Circuits and Systems*, Vol. 6, No. 5, pp. 479-485, 2012

A Self Contained System with CNTs-based Biosensors for Cell-culture Monitoring,

C. Boero, J. Olivo, S. Carrara and G. De Micheli, *IEEE Journal on Emerging and Selected Topics in Circuits and Systems*, Vol. 2, No. 4, pp. 658-671, 2012

Fully Integrated Biochip Platforms for Advanced Healthcare

S. Carrara, S. Ghoreishizadeh, J. Olivo, I. Taurino, C. Baj-Rossi, A. Cavallini, M. Op de Beeck, C. Dehollain, W. Burseson, F.G. Moussy, A. Guiseppi-Elie, and G. De Micheli, *Sensors*, Vol. 12, No.8, pp. 11013-11060, 2012

Conference

Optimal Frequencies for Inductive Powering of Fully Implantable Biosensors for Chronic and Elderly Patients,

J. Olivo, S. Carrara, and G. De Micheli, *IEEE Sensors Conference*, pp.99-103, 2010

Modeling of Printed Spiral Inductors for Remote Powering of Implantable Biosensors,

J. Olivo, S. Carrara, and G. De Micheli, *5th International Symposium on Medical Information and Communication Technology (ISMICT)*, pp. 29-32, 2011

IronIC Patch: A Wearable Device for the Remote Powering and Connectivity of Implantable Systems,

J. Olivo, S. Carrara, G. De Micheli, *IEEE Instrumentation and Measurement Technology Conference (I2MTC)*, pp. 286-289, 2012

Electronic Implants: Power Delivery and Management,

J. Olivo, S. Ghoreishizadeh, S. Carrara, G. De Micheli, *Conference on Design, Automation and Test in Europe (DATE)*, pp.1540-1545, 2013

Developing Highly-integrated Subcutaneous Biochips for Remote Monitoring of Human Metabolism,

S. Carrara, A. Cavallini, S. Ghoreishizadeh, J. Olivo, G. De Micheli, *IEEE Sensors Conference*, pp. 1-4, 2012

Not Related to the Thesis Work

A Kinetic Energy Harvester with Fast Start-up for Wearable Body-monitoring Sensors,

J. Olivo, D. Brunelli, L. Benini, *4th International Conference on Pervasive Computing Technologies for Healthcare* pp. 1-7, 2010

Circuits Design and Nano-Structured Electrodes for Drugs Monitoring in Personalized Therapy,

S. Carrara, A. Cavallini, G. De Micheli, J. Olivo, L. Benini, V.V. Shumyantseva, A.I. Arhakov, *IEEE Biomedical Circuits and Systems Conference (BIOCAS)*, pp.325-328, 2008